AFOSR - TR - 76 - 0146

AD A023175

SYSTEMS, SCIENCE AND SOFTWARE

SSS-R-76-2792

APPLICATION OF ADVANCED METHODS FOR IDENTIFICATION AND DETECTION OF NUCLEAR EXPLOSIONS FROM THE ASIAN CONTINENT

J. M. Savino
T. C. Bache
J. T. Cherry
K. G. Hamilton
D. G. Lambert
J. F. Masso

Semi-Annual Technical Report

DDC
RECEIVED
APR 20 1976
A

Sponsored by:

Advanced Research Projects Agency
ARPA Order No. 1827
Program Code 4F10

Contract No. F44620-74-C-0063
Effective Date of Contract: 4/1/74
Contract Expiration Date: 3/31/76
Amount of Contract: $567,312

S^3 Project 261

AIR FORCE OFFICE OF SCIENTIFIC RESEARCH (AFSC)
... reviewed and is
... AFR 190-12 (7b).
... is unlimited.
A. D. ...
Technical Information Officer

December 1975

P.O. BOX 1620, LA JOLLA, CALIFORNIA 92038, TELEPHONE (714) 453-0060

UNCLASSIFIED

SECURITY CLASSIFICATION OF THIS PAGE (When Data Entered)

REPORT DOCUMENTATION PAGE	READ INSTRUCTIONS BEFORE COMPLETING FORM
1. REPORT NUMBER: AFOSR TR-76-0146	2. GOVT ACCESSION NO. / 3. RECIPIENT'S CATALOG NUMBER
4. TITLE (and Subtitle): APPLICATION OF ADVANCED METHODS FOR IDENTIFICATION AND DETECTION OF NUCLEAR EXPLOSIONS FROM THE ASIAN CONTINENT.	5. TYPE OF REPORT & PERIOD COVERED: Semi-Annual Technical rept. 2
	6. PERFORMING ORG. REPORT NUMBER: SSS-R-76-2792
7. AUTHOR(s): J. M. Savino, T. C. Bache, J. T. Cherry, K. G. Hamilton, D. G. Lambert and J. F. Masso	8. CONTRACT OR GRANT NUMBER(s): F44620-74-C-0063, ARPA Order-1827
9. PERFORMING ORGANIZATION NAME AND ADDRESS: Systems, Science and Software, P. O. Box 1620, La Jolla, California 92038 (16) S3-261	10. PROGRAM ELEMENT, PROJECT, TASK AREA & WORK UNIT NUMBERS: 62701E, AO 1827-17
11. CONTROLLING OFFICE NAME AND ADDRESS: Advanced Research Projects Agency/NMR, 1400 Wilson Boulevard, Arlington, Virginia 22209	12. REPORT DATE: December 1975
	13. NUMBER OF PAGES: 159
14. MONITORING AGENCY NAME & ADDRESS (if different from Controlling Office): Air Force Office of Scientific Research, 1400 Wilson Boulevard, Arlington, Virginia 22209 (12) 162p.	15. SECURITY CLASS. (of this report)
	15a. DECLASSIFICATION/DOWNGRADING SCHEDULE

16. DISTRIBUTION STATEMENT (of this Report)

Approved for public release; distribution unlimited.

17. DISTRIBUTION STATEMENT (of the abstract entered in Block 20, if different from Report)

(10) John M. /Savino, Thomas C. /Bache, J. Theodore /Cherry, Kenneth G. /Hamilton, David G. /Lambert

18. SUPPLEMENTARY

19. KEY WORDS (Continue on reverse side if necessary and identify by block number)

Seismology
Nuclear Explosions
Teleseismic Ground Motion
Seismic Discrimination
Time Series Analysis
Earthquake Source Modeling

20. ABSTRACT (Continue on reverse side if necessary and identify by block number)

The objective of this research program is to develop an optimum multi-discriminant/detection procedure for earthquake and underground explosions with emphasis on events occurring within the Asian continent. The approach to the seismic discrimination problem incorporates a number of diverse topics including: explosion and earthquake source modeling; stress wave propagation through realistic earth structures and prediction of teleseismically recorded ground motion; the development of signal

Next page

DD FORM 1 JAN 73 1473 EDITION OF 1 NOV 65 IS OBSOLETE

UNCLASSIFIED

SECURITY CLASSIFICATION OF THIS PAGE (When Data Entered)

388 507

20.

detection, enhancement and identification techniques; multi-discriminant testing of a large population of worldwide events.

One of the most significant achievements described in this report is the development of a three-dimensional finite difference stick-slip earthquake model and the characterization of the far-field (that which propagates to teleseismic distances) radiation of stress waves generated by this source.

A theoretical analysis of the influence of tectonic release on the teleseismic short-period P-wave signature from underground nuclear explosions was also conducted. The principal result of this study is that in the case of most, if not all, explosions, tectonic release does not measurably affect the short-period P-wave signature.

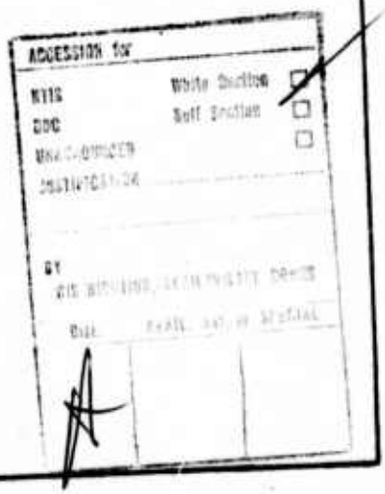

FOREWORD

This semi-annual technical report entitled, "Application of Advanced Methods for Identification and Detection of Nuclear Explosions from the Asian Continent," is submitted by Systems, Science and Software (S^3) to the Advanced Research Projects Agency and to the Air Force Office of Scientific Research (AFOSR). This report presents the results of a continuing effort to obtain an optimum multi-discriminant/detection procedure for earthquakes and explosions occurring within the Asian Continent. The work is being performed under Contract Number F44620-74-C-0063. Mr. William J. Best is the AFOSR technical contracting officer.

Dr. J. Theodore Cherry is the S^3 project manager. Drs. Thomas C. Bache and Joseph F. Masso are responsible for the development and application of the seismic ground motion prediction work. Dr. John M. Savino and Messrs. Kenneth G. Hamilton and David G. Lambert are responsible for the analysis of the seismic data against which all theoretical developments must eventually be tested. Acting as consultants on the project are Professors Charles B. Archambeau of the University of Colorado, David G. Harkrider of the California Institute of Technology and Donald V. Helmberger of the California Institute of Technology.

The authors wish to extend their sincere appreciation to Ms. Bernadine Ludwig and Ms. Darlene Roddy for the many hours spent on the preparation of this report.

TABLE OF CONTENTS

		Page
I.	INTRODUCTION	5
II.	THE MULTIPLE ARRIVAL RECOGNITION SYSTEM . . .	8
	2.1 INTRODUCTION	8
	2.2 NARROW-BAND FILTERING (NBF)	8
	2.3 INSTRUMENTAL CORRECTION	10
	2.4 ENVELOPE CONSTRUCTION BY HILBERT TRANSFORMS	12
	2.5 DETECTION OF ARRIVALS IN THE $t_g - f_c$ PLANE	15
	2.6 VARIABLE FREQUENCY MAGNITUDE DETERMINATION	15
	2.7 NOISE CORRECTION	18
	2.8 DEMONSTRATION OF NARROW-BAND FILTERING FOR SEISMIC EVENTS	18
	2.9 POLARIZATION FILTERING	27
	2.10 CONSTRUCTION OF POLARIZATION-FILTERED WAVES	31
	2.11 DEMONSTRATION OF POLARIZATION FILTERING FOR ARTIFICIAL SIGNALS	31
	2.12 POLARIZATION ANALYSIS OF SEVERAL OBSERVATIONAL EVENTS	40
III.	VARIABLE FREQUENCY MAGNITUDE DISCRIMINANT . .	54
	3.1 INTRODUCTION	54
	3.2 NORTH AMERICAN EVENTS RECORDED IN CANADA	54
	3.3 RESULTS OF THE VFM DISCRIMINATION TEST .	58
	3.4 SUMMARY	61

TABLE OF CONTENTS (Continued)

		Page
IV.	THE EFFECT OF TECTONIC RELEASE ON THE TELESEISMIC SHORT PERIOD SEISMOGRAM	62
	4.1 INTRODUCTION	62
	4.2 ARCHAMBEAU'S TECTONIC RELEASE MODEL . .	64
	4.3 EXPLOSION MODELING	66
	4.4 THE EQUIVALENT ELASTIC SOURCE	70
	4.5 COMPUTATION OF THEORETICAL SEISMOGRAMS	78
	4.6 TECTONIC RELEASE FROM AN OPTIMALLY ORIENTED PRESTRESS FIELD	82
	4.7 SUMMARY AND CONCLUSIONS	91
V.	A THREE-DIMENSIONAL FINITE DIFFERENCE SIMULATION OF STICK-SLIP EARTHQUAKE FAULTING — THE EQUIVALENT ELASTIC SOURCE	95
	5.1 INTRODUCTION	95
	5.2 FAULT CONFIGURATION FOR THE THREE-DIMENSIONAL CALCULATION	96
	5.3 EQUIVALENT ELASTIC SOURCE REPRESENTATION	100
	5.4 THE EQUIVALENT ELASTIC SOURCE FOR THE BILATERAL RUPTURE	103
	5.5 FAR-FIELD DISPLACEMENT SPECTRA	107
VI.	REFERENCES	116
APPENDIX A —	SYMMETRY PROPERTIES OF THE STICK-SLIP RUPTURE SOURCE MODEL	120
APPENDIX B —	THE NONZERO MULTIPOLE COEFFICIENTS FOR THE BILATERAL RUPTURE	134

TABLE OF CONTENTS (Continued)

Page

APPENDIX C — ASYMPTOTIC BEHAVIOR OF THE EQUIVALENT ELASTIC SOURCE 145

APPENDIX D — HIGH-FREQUENCY APPROXIMATIONS DUE TO THE DISCRETE GRID IN THE THREE-DIMENSIONAL FINITE DIFFERENCE CALCULATION. . . 153

I. INTRODUCTION

The conduct of the research under this contract is aimed at the development of an optimum multi-discriminant/detection procedure for earthquakes and underground explosions with emphasis on events occurring within the Asian continent. In order to realize this objective our research program has involved a combined theoretical/empirical approach. That is, deterministic predictions of teleseismic ground motion generated by underground explosion and earthquake sources are ultimately compared to actual observations. In this way we are provided with a confirmed theoretical framework for testing existing discriminants, as well as designing new discriminants.

Our approach is quite comprehensive and, in outline form, involves the following:

1. Explosion and earthquake source modeling.
2. Stress wave propagation through complicated realistic earth structure.
3. Development of state of the art signal enhancement and identification techniques.
4. Multi-discriminant design and evaluation.

Section II of this report is devoted to a detailed description of an extremely versatile computer code, MARS (Multiple Arrival Recognition System), that incorporates several different data processing techniques for signal detection, enhancement and identification. The MARS code now accepts from one up to three components of seismic data and applies a series of narrow band filters to determine spectral amplitudes. Corrections for instrument response may be made and true dispersion data computed. Polarization and dispersion filters may then be applied to separate

the various modes of wave propagation present in the record. Then, for example, the code can filter the record to select only those P-waves arriving along selected ray paths (azimuth and emergence angle). Matched filtering and cross-correlation are among the other data processing capabilities available as options in the code.

The variable frequency magnitude (VFM) technique, embodied in the MARS code, has been tested on a wide range of seismic event data to determine its effectiveness as a discriminant between earthquakes and underground explosions. In Section III we discuss the results of an application of the VFM technique to a large population of North American earthquakes and explosions at the Nevada Test Site (NTS) recorded at the 19-element short-period Yellowknife array in Canada. These results are compared to previous results obtained for Eurasian events recorded at LASA.

In Section IV is a theoretical analysis which addresses the question: under what circumstances can tectonic release have an important effect on the teleseismic short period P-wave signature of underground nuclear explosions? The analysis has validity whether one assumes that the primary mechanism for the release of tectonic stress is the creation of a spherical shatter zone by the explosion or movement along a pre-existing fault plane. In either case, it is only under optimal conditions that the tectonic release contribution to the seismogram becomes important. It is concluded that in the case of most, if not all, events it is safe to ignore tectonic release as a contributor to the short period P-wave recording.

A three-dimensional finite difference simulation of an earthquake is discussed in Section V. The calculation includes a realistic nonlinear model of spontaneous stick-slip earthquake faulting for the case of a bilateral rupture on a fault surface that is 1 km long and 0.6 km wide. An

equivalent elastic point source representation of the earthquake is obtained. Using this unique and exact representation, the far-field (that which propagates to teleseismic distances) radiation of stress waves by the earthquake source is studied.

Appendices A - D pertain to key elements of the 3-D finite difference earthquake calculation described in Section V. Sections II and III should be read in sequence. Sections IV and V are self-contained and may be read independently.

II. THE MULTIPLE ARRIVAL RECOGNITION SYSTEM

2.1 INTRODUCTION

Significant progress has been made on the Multiple Arrival Recognition System (MARS) since the last semi-annual report (Bache, et al. [1975a]), where it was briefly outlined in an appendix. As will be shown in this section, the MARS code has developed into an extremely powerful and efficient tool for signal (body and surface waves) detection and enhancement, and for discrimination between earthquakes and underground explosions.

Improvements made to the MARS code during the last six months include provisions to correct envelopes for frequency-dependent noise, to remove signal distortion due to instrumental factors, and to perform polarization filtering on multicomponent data. Improvements have also been implemented for display of the computed results.

2.2 NARROW-BAND FILTERING (NBF)

Data are input to MARS in the form of a time series, generally of about 500-2000 points in length. The data are then optionally demeaned, detrended, and tapered at the tail end by a cosine bell. MARS then selects the smallest power of two which is greater than the number of points input, and performs a discrete Fourier transform using the algorithm of Cooley and Tukey [1965]. Both the time series and the spectrum are plotted for examination.

The signal is filtered in the frequency domain by multiplication with a cusp-type filter of the form:

$$F(f) = \begin{cases} 1 - \cos \frac{\pi}{3}\left[\frac{f - \left(f_c - \frac{3}{2}\Delta f\right)}{\Delta f}\right], & f_c - \frac{3}{2}\Delta f \leq f \leq f_c \\ 1 - \cos \frac{\pi}{3}\left[\frac{\left(f_c + \frac{3}{2}\Delta f\right) - f}{\Delta f}\right], & f_c \leq f \leq f_c + \frac{3}{2}\Delta f \\ 0 \text{ , otherwise} \end{cases}$$

This filter is drawn in Fig. 2.1. It was discussed in the previous report (Bache, et al. [1975a]), compared against several other filter shapes, and found to be the best in terms of time-domain ripple suppression. The width at one-half maximum amplitude is designated Δf.

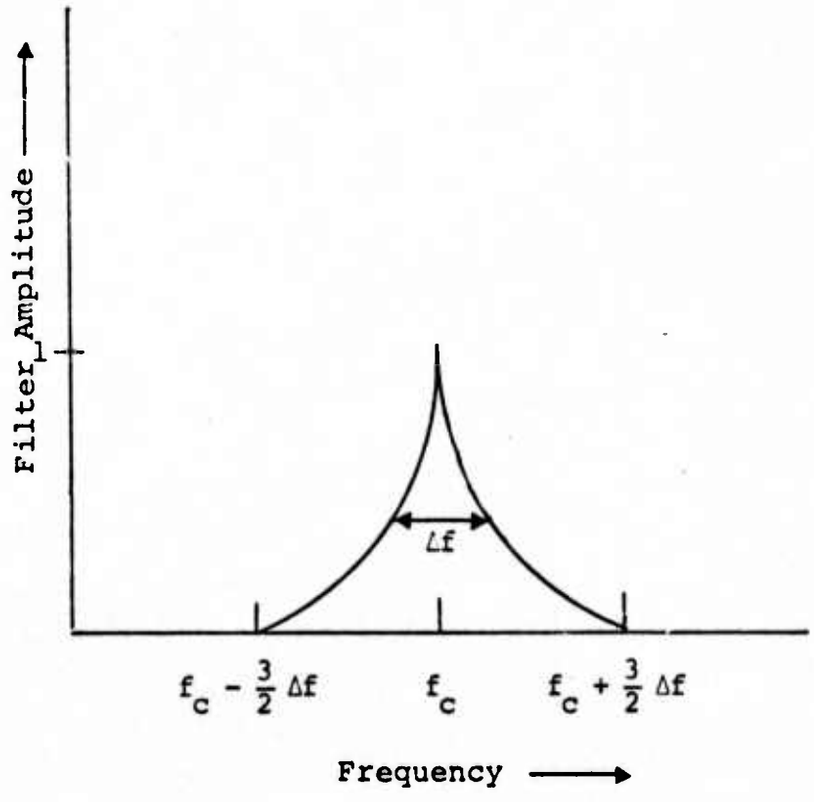

Figure 2.1. Filter shape used in MARS.

2.3 INSTRUMENTAL CORRECTION

Once a signal has been narrow-band filtered, MARS corrects it for instrument response. When a seismogram is originally taken, it is measured through a system whose transfer function is strongly frequency-dependent; this distortion affects both the amplitude and the phase of the signal. If we are to make accurate measurements of magnitude and arrival time, the signal must be corrected for the appropriate instrument response.

A typical seismic system consists of: (a) a transducer, which converts ground motion into electrical signals; (b) a galvanometer, driving a mirror to provide optical amplification; (c) a system of photocells to provide conversion back to an analog electrical signal; (d) an electrical filter to further shape the pass-band, and finally, (e) a digitizer and recorder where the data are stored.

The transducer and galvanometer considered separately, both obey second-order ordinary differential equations. When they are coupled together, the resulting system obeys the equation (c.f., for example, Kisslinger [1971])

$$\theta^{(iv)} + A\dddot{\theta} + B\ddot{\theta} + C\dot{\theta} + D\tau = -E\dddot{X}$$

for the galvanometer deflection angle (θ) due to a ground motion (X), where

$$A = 2h_T\omega_T + 2h_G\omega_G$$

$$B = \omega_T^2 + 4h_Th_G\omega_T\omega_G + \omega_G^2 - 4h_Th_G\omega_T\omega_G\sigma^2$$

$$C = 2h_T\omega_T\omega_G^2 + 2h_G\omega_G\omega_T^2$$

$$D = \omega_T^2\omega_G^2$$

$$E = \frac{2h_G\omega_G\sigma}{\ell}$$

ω_T = transducer resonant frequency

ω_G = galvanometer resonant frequency

h_T = transducer damping fraction

h_G = galvanometer damping fraction

σ = a constant which measures coupling between transducer and galvanometer

ℓ = a measure of the mass, restoring spring, and level arm of the transducer

Fourier transformation of this yields the transfer function

$$\chi(\omega) = \frac{i\omega^3/\chi_0}{(\omega^4 - B\omega^2 + D) + i(-A\omega^3 + C\omega)} ,$$

with χ_0 being chosen as a real number which causes $|\chi| = 1$ at a frequency of $\omega/2\pi = f = 1$ Hz. An approximation to a short-period LRSM instrument is given by using the values

$$\omega_T = 2\pi/1.02$$

$$\omega_G = 2\pi/0.2$$

$$h_T = 0.98$$

$$h_G = 0.9$$

$$\sigma^2 = 0.01 .$$

The MARS program divides the signal transform by this transfer function, after the former has been narrow-band filtered.

The electrical filter used on the seismic data is typically a Geotech model 6824-1, or one of a similar family. These filters can be described reasonably well by the transfer function

$$\bar{\chi}(\omega) = \frac{i\omega R^2/\bar{\chi}_0}{(a + i\omega)[R^2 - \omega^2 + i2SR\omega]} \quad .$$

The first term of the denominator provides a very sharp low-frequency cut-off; a is generally taken to be $\pi/50$. The second part of the denominator is clearly a harmonic oscillator response; for this we have taken $R = 40\pi/7$ and $S = \sqrt{1/2}$. Like the instrument response, this transfer function is normalized to be 1 at 1 Hz by a judicious choice of $\bar{\chi}_0$. The narrow-band filtered signal transform is also divided by this factor, to bring the signal much closer to a filtered true ground motion.

The resulting complex spectrum is then inverse Fourier transformed into the time domain, to produce what will hereinafter be called the filtered signal.

2.4 ENVELOPE CONSTRUCTION BY HILBERT TRANSFORMS (Bracewell, [1965])

The filtered signal produced by MARS has the form

$$X(t) = A(t) \cos(\omega_c t + \phi) \ , \ \omega_c > 0 \ ,$$

which clearly represents a modulated carrier wave. Its Fourier transform is

$$\hat{X}(\omega) = \int_{-\infty}^{+\infty} X(t)\, e^{-i\omega t}\, dt \quad .$$

This can be integrated to produce

$$\hat{X}(\omega) = \frac{1}{2} \left[e^{i\phi} \hat{A}(\omega - \omega_c) + e^{-i\phi} \hat{A}(\omega + \omega_c) \right] ,$$

where $\hat{A}(\omega)$ is the Fourier transform of $A(t)$.

If we consider the same signal, but with a 90° phase shift,

$$Y(t) = A(t) \sin(\omega_c t + \phi) ,$$

then its transform is

$$\hat{Y}(\omega) = \frac{1}{2} \left[-ie^{i\phi} \hat{A}(\omega - \omega_c) + ie^{-i\phi} \hat{A}(\omega + \omega_c) \right] .$$

These two functions of frequency can be easily related by the Hilbert transform condition,

$$\hat{Y}(\omega) = -i \, \mathrm{sgn}(\omega) \, \hat{X}(\omega) ,$$

provided that $\hat{A}(\omega)$ has significant amplitude only near $\omega = 0$, and drops essentially to zero for $|\omega| \geq \omega_c$. This condition is equivalent to having a narrow-band signal; since our filtered signal obeys this condition, we can generate a signal which has the same envelope function, $A(t)$, as the filtered signal, but which is 90° out of phase. This secondary signal is ordinarily referred to as the quadrature, while the corresponding analytic signal is defined by

$$Z(t) = X(t) + i\,Y(t) = A(t)\, e^{i(\omega_c t + \phi)} .$$

It is of interest to note that the analytic signal contains only positive frequency components. The envelope is extracted from it quite easily as

$$A(t) = |Z(t)| = \sqrt{X^2(t) + Y^2(t)} ,$$

while the instantaneous phase and frequency are given as

$$\Phi(t) = \omega_c t + \phi = \text{Arctan}[Y(t)/X(t)] \quad ,$$

and

$$\omega(t) = \frac{d\Phi}{dt} = \omega_c + \frac{d\phi}{dt} \quad .$$

This method is followed in MARS: The transform of the filtered signal is multiplied by $-i\ \text{sgn}(\omega)$, and then brought to the time domain by an inverse transformation. The envelope and instantaneous frequency are produced; the envelope has applications in terms of variable-frequency magnitude (VFM) measurements, while the instantaneous frequency is utilized mostly for polarization filtering. Both of these subjects will be discussed later and at greater length.

An envelope, constructed by narrow-band filtering in this manner, will be a very smooth function of time. The time required for the envelope to change its height appreciably must be proportional to the inverse filter width $1/\Delta f = Q/f_c$; this statement is essentially just the well-known uncertainty principle. Stated in terms of information theory, a signal of a particular bandwidth is limited in the amount of information which it can carry, so that the highest rate of information flow is the same as the frequency width of the channel.

It is true that a signal of a pure frequency has no time dependence. However, it is possible, using only those frequency components which fall within a limited bandpass, to make up a wave-packet group which is fairly localized in time. Taken in this light, the time variation of an envelope can be interpreted as being the arrival (or non-arrival) of wave groups of the filter frequency; the variation will describe the appearance of energy of that frequency.

2.5 DETECTION OF ARRIVALS IN THE t_g - f_c PLANE

Given a particular seismic signal, the procedure of envelope construction can be performed for a number of filter center frequencies, f_c. For each of these envelopes, a group arrival time (t_g) can be computed and plotted as a function of f_c. If the original signal consists of only one undispersed arrival, then the arrival time diagram will look like Fig. 2.2a.

If a single arrival is present, but it has been dispersed such that low frequencies travel fastest (e.g., normally dispersed Rayleigh waves) then the arrival time diagram looks like Fig. 2.2b. Figure 2.2c exhibits the opposite effect, with high frequencies traveling faster than lows, as in the case of inversely dispersed surface waves. Under certain circumstances, a dispersion curve can bend down and have a flat portion, or a minimum. This type of dispersion gives rise to an Airy phase (Båth [1968]) and is demonstrated in Fig. 2.2d.

2.6 VARIABLE FREQUENCY MAGNITUDE DETERMINATION

For each filter frequency and for each significant signal arrival, in terms of signal-to-ncise ratio, it is possible to compute a seismic magnitude. The procedure followed in MARS is to define body wave magnitudes as

$$m_b = \log_{10}(S_{max}/f_c) + B(\Delta) + 0.05$$

and surface wave magnitudes as

$$M_s = \log_{10}(S_{max}/f_c) + 1.656 \log_{10}(\Delta) + 1.6 ,$$

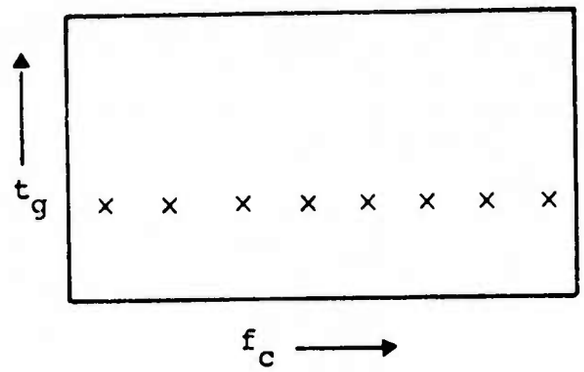

Figure 2.2a. Arrival time diagram for an undispersed pulse.

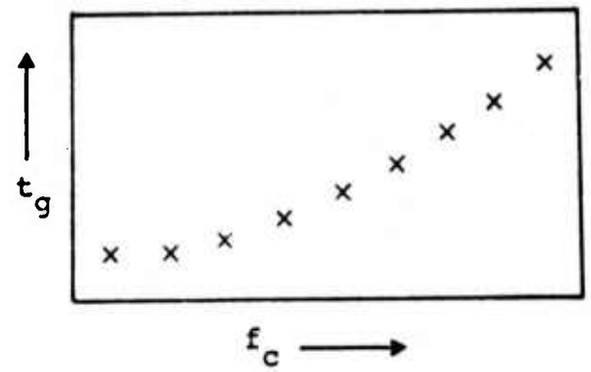

Figure 2.2b. Arrival time diagram for a pulse which has been dispersed by propagation through a medium in which low frequencies travel faster than high.

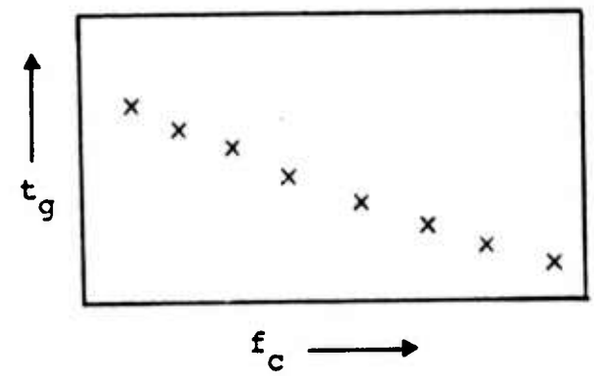

Figure 2.2c. Dispersion causes high frequencies to travel fastest.

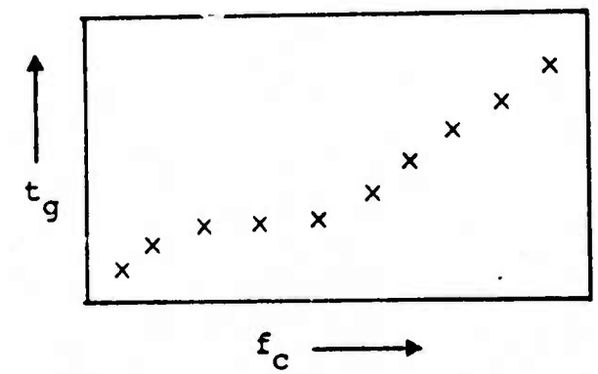

Figure 2.2d. Airy phase dispersion.

where

S_{max} = envelope peak value

f_c = filter center frequency

Δ = distance between event and detector in degrees.

The function $B(\Delta)$ represents modified Gutenberg-Richter distance correction factors, derived from LRSM data. The exact values used are shown in Table 2.1.

TABLE 2.1. MODIFIED GUTENBERG-RICHTER B-FACTORS

DELTA	B	DELTA	B	DELTA	B	DELTA	B	DELTA	B
1.	1.0	22.	3.2	43.	3.5	64.	4.0	85.	4.0
2.	2.2	23.	3.3	44.	3.5	65.	4.0	86.	3.9
3.	2.7	24.	3.3	45.	3.7	66.	4.0	87.	4.0
4.	3.1	25.	3.5	46.	3.8	67.	4.0	88.	4.1
5.	3.4	26.	3.4	47.	3.9	68.	4.0	89.	4.0
6.	3.6	27.	3.5	48.	3.9	69.	4.0	90.	4.0
7.	3.8	28.	3.6	49.	3.8	70.	3.9	91.	4.1
8.	4.0	29.	3.6	50.	3.7	71.	3.9	92.	4.1
9.	4.2	30.	3.6	51.	3.7	72.	3.9	93.	4.2
10.	4.3	31.	3.7	52.	3.7	73.	3.9	94.	4.1
11.	4.2	32.	3.7	53.	3.7	74.	3.8	95.	4.2
12.	4.1	33.	3.7	54.	3.8	75.	3.8	96.	4.3
13.	4.0	34.	3.7	55.	3.8	76.	3.9	97.	4.4
14.	3.6	35.	3.7	56.	3.8	77.	3.9	98.	4.5
15.	3.3	36.	3.6	57.	3.8	78.	3.9	99.	4.5
16.	2.9	37.	3.5	58.	3.8	79.	3.8	100.	4.4
17.	2.9	38.	3.5	59.	3.8	80.	3.7	101.	4.3
18.	2.9	39.	3.4	60.	3.8	81.	3.8	102.	4.4
19.	3.0	40.	3.4	61.	3.9	82.	3.9	103.	4.5
20.	3.0	41.	3.5	62.	4.0	83.	4.0	104.	4.6
21.	3.1	42.	3.5	63.	3.9	84.	4.0	105.	4.7

2.7 NOISE CORRECTION

When an event is processed which contains a significant amount of noise, a noise correction can be made to the spectral amplitudes. This is done by taking a section of the seismogram before the arrival of the actual event, and processing the noise alone as though it were a signal. The noise envelope is formed for each of several filter frequencies, and in each case the maximum value is taken as an amplitude correction factor.

Subsequently, when the signal window is processed and the signal envelopes constructed, the maximum noise amplitude at that frequency is subtracted as a constant. This will cause the less significant signal envelope peaks to be submerged, and they can be disregarded as far as arrival identification is concerned.

2.8 DEMONSTRATION OF NARROW-BAND FILTERING FOR SEISMIC EVENTS

In this subsection of the report the narrow-band filtering technique described above will be applied to actual seismic signals recorded at the LASA and NORSAR short-period vertical-component arrays located in Montana and Norway, respectively. The seismograms are best beam recordings based on phasing of the full arrays.

Figure 2.3a shows a LASA best beam recording of a P-wave train from a presumed explosion that occurred in eastern Kazakhstan: hereafter referred to as LASA Event 1522. The amplitude scale given along the ordinate in this figure is in millimicrons of ground motion at 1 Hz. Figure 2.3b is the amplitude spectrum of this event, showing that the signal energy is principally in the region of 1 Hz, as one would expect for body waves detected at teleseismic distances by short-period instruments of the LASA type.

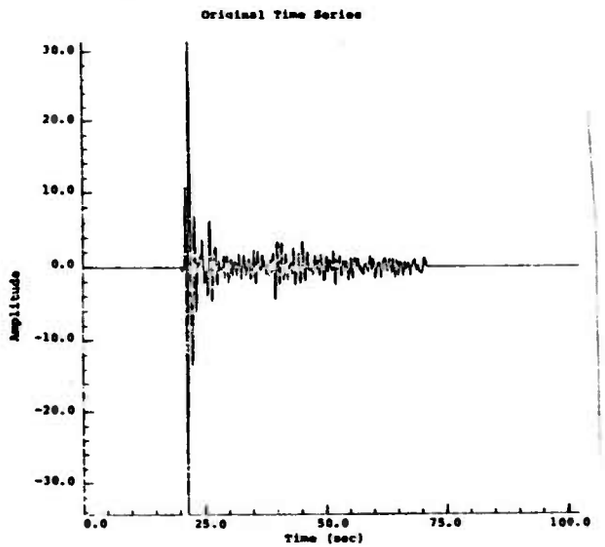

Figure 2.3a. LASA Event 1522: Vertical component.

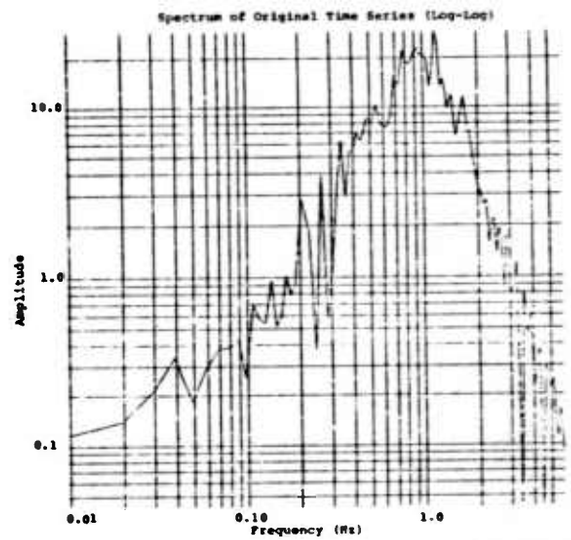

Figure 2.3b. Spectrum of LASA Event 1522 vertical motion.

The time series in Fig. 2.3a was processed through ten narrow-band filters, with center frequencies f_c = 0.4, 0.6, 0.8, 1.0, 1.2, 1.4, 1.5, 1.6, 1.8 and 2.0 Hz, all with quality factors of Q = 10. The single arrival nature of these data is reflected in Fig. 2.3c, which shows the sum of the envelopes for the ten filters as a function of time.

Figure 2.3d is an arrival time diagram, on which time runs horizontally and filter center frequency vertically. For each frequency, the envelope is plotted as a function of time; each of these curves has been normalized so as to have the same height. The undispersed nature of these data are quite evident.

A LASA recording of a P-wave train from a Japanese earthquake is shown in Fig. 2.4a; this is referred to as LASA Event 2030. In it, a direct P-wave is demonstrated (arriving at approximately t = 20 seconds) followed by a surface reflection (pP at ≈ t = 31 seconds). This event was processed through the same filters as for the previous event (LASA 1522), and the sum of the envelopes is shown in Fig. 2.4b. The separation between the envelope peaks is 11.0 seconds, compared with the separation of approximately 12.0 seconds in the unfiltered signal. This event was reported in the Preliminary Determination of Epicenters (PDE) to be at a depth of 40 km and a distance of 63.5° from LASA, for which a pP-P time delay of 11.4 seconds is considered normal (Herrin, et al. [1968]).

For Event 2030, the envelopes for different frequencies are shown in Fig. 2.4c. This figure demonstrates an interesting phenomenon: at low frequencies, an envelope maximum appears in the neighborhood of t = 32-33 seconds, but vanishing when f_c > 1 Hz. At the same time, the envelope peak near t = 22-23 seconds grows in significance with increasing frequency. The message conveyed by this is clear — the pP signal does not contain as much high frequency energy as the

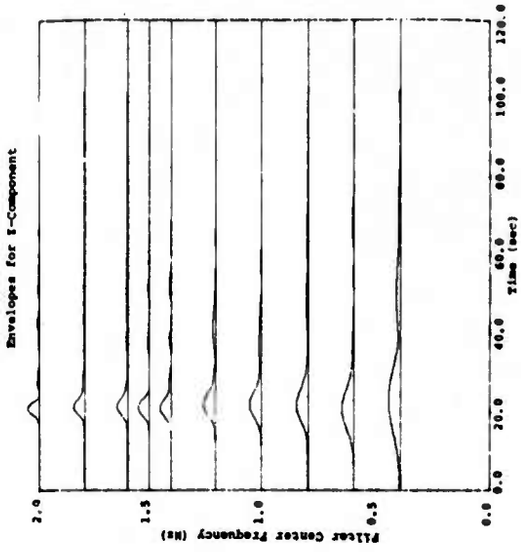

Figure 2.3d. Envelopes for various filters applied to LASA Event 1522.

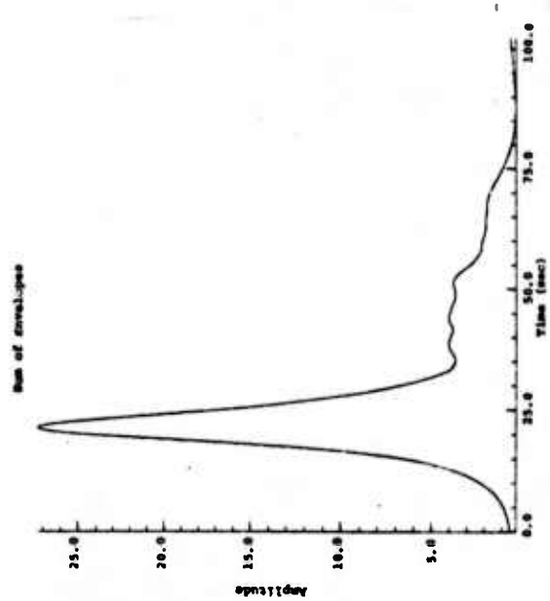

Figure 2.3c. LASA Event 1522: Sum of envelopes.

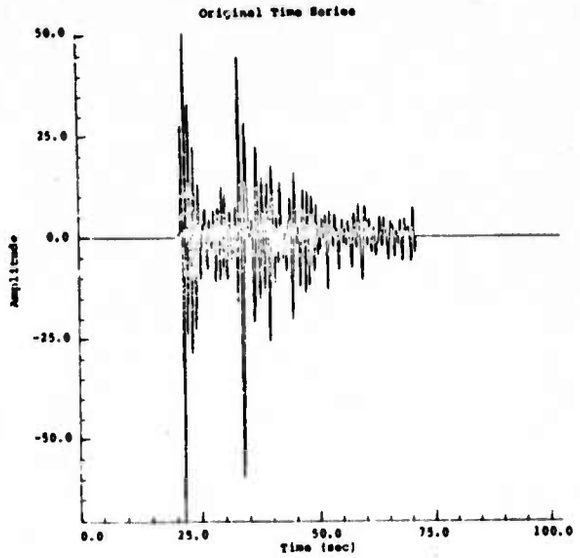

Figure 2.4a. LASA Event 2030: Vertical component.

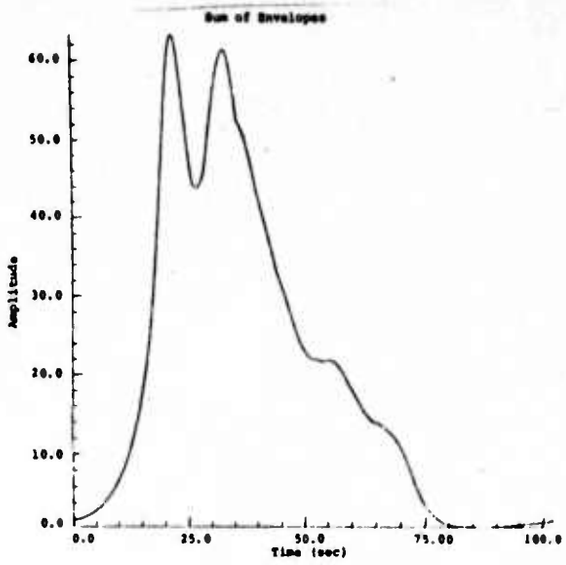

Figure 2.4b. LASA Event 2030: Sum of ten envelopes.

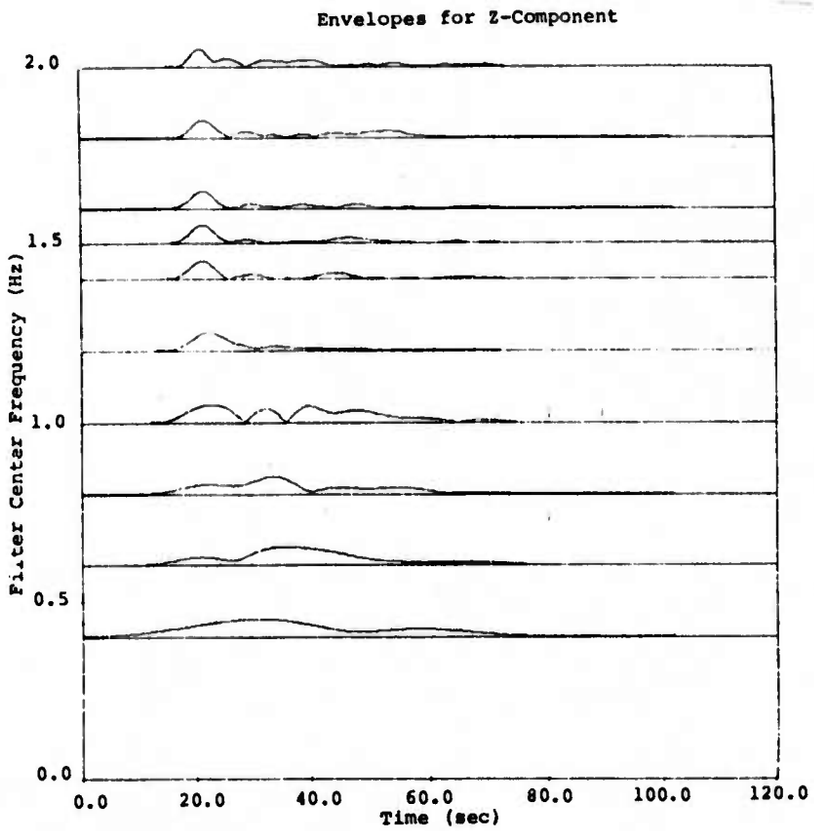

Figure 2.4c. Envelopes for LASA 2030 vertical motion.

P signal. This can possibly be interpreted as the effect of absorption of the high frequency components of the free surface reflection, pP, by relatively low Q, high attenuation, surface layers in the source region.

LASA Event 2011, a Rumanian earthquake, is shown in Fig. 2.5a. This signal was filtered at the same frequencies as the previous two events, with an arrival time diagram of the sum of the envelopes being shown in Fig. 2.5b and one for the individual filter envelopes in Fig. 2.5c. The largest peak, at t = 23.0 seconds, is due to direct P-wave; the next largest is at t = 62.0 seconds. This delay of 39.0 seconds, for a source at a distance of 76.2° and a depth of 158 km (PDE), falls in the range given for pP in the travel-time tables of Herrin, et al. [1968] whose delay times are reproduced in Table 2.2.

TABLE 2.2. pP DELAY TIMES IN SECONDS

Distance	Depth	
	150 km	200 km
75°	36.2	47.0
80°	36.6	47.6

Examination of Fig. 2.5c shows that the amplitude of the pP phase dies out with increasing filter frequency, relative to the amplitude of the direct P-wave: below 1 Hz, the pP is as strong or stronger than the P, while above that frequency, direct P is clearly dominant. This is similar to the behavior as noted for Event 2030.

The third largest peak in Fig. 2.5b lies at t = 33.0 seconds, a delay with respect to P of 10.0 seconds. This

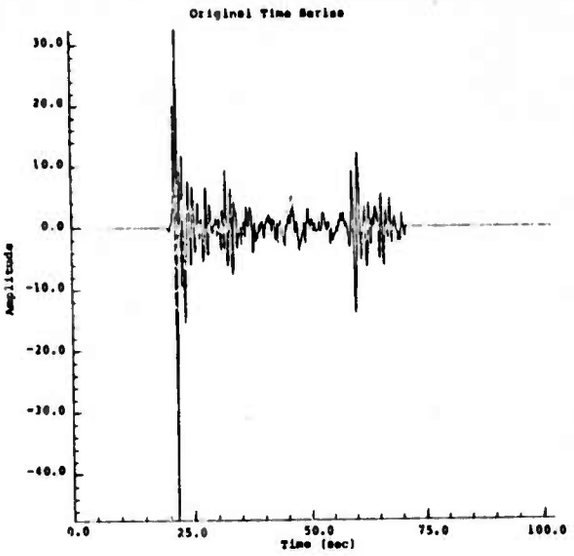

Figure 2.5a. LASA Event 2011: Vertical motion.

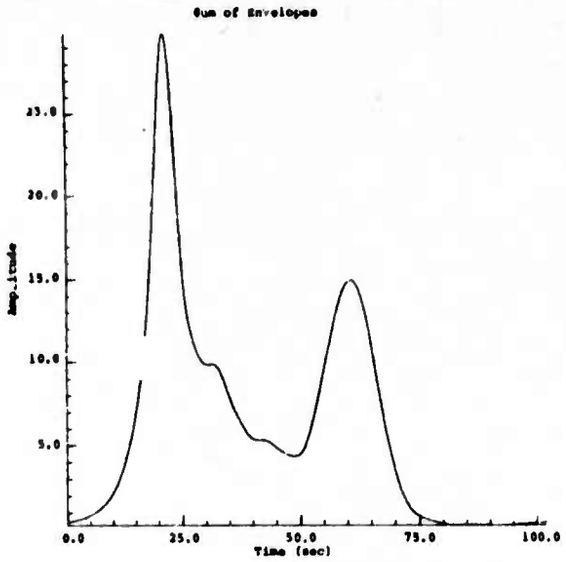

Figure 2.5b. LASA Event 2011: Sum of ten envelopes.

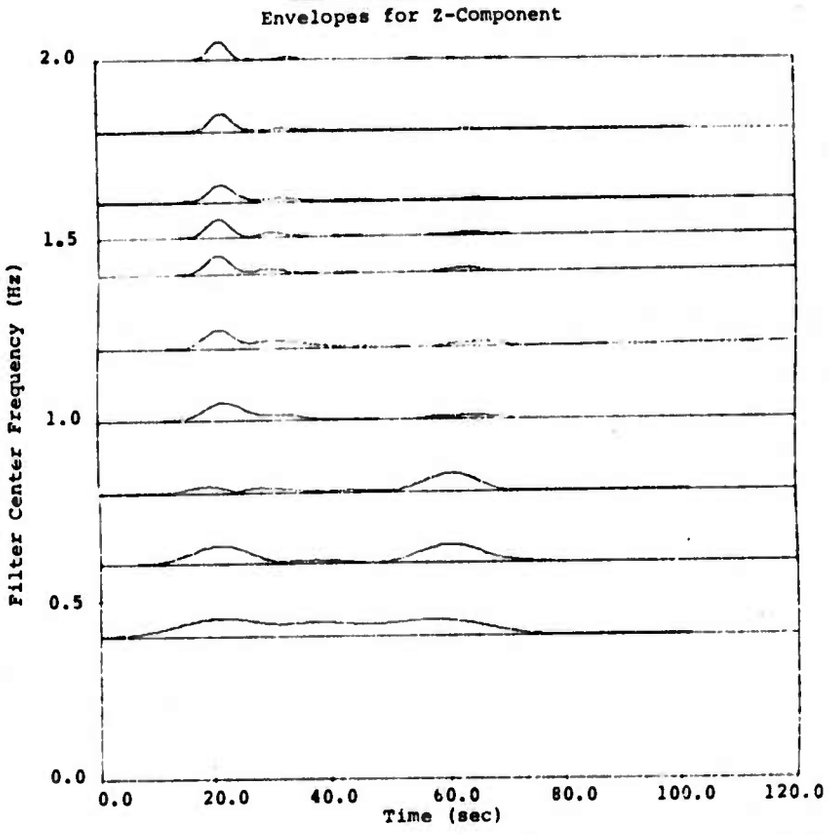

Figure 2.5c. Individual envelopes for LASA 2011.

fits in well with Herrin's values for a core reflection, PcP, and the bracketing data are depicted in Table 2.3.

TABLE 2.3. DELAY TIMES BETWEEN P AND PcP

Distance	Depth	
	150 km	200 km
75°	13.0	12.7
80°	6.9	6.7

Figure 2.5c shows, interestingly enough, that the PcP signal strength is roughly a constant fraction of the direct P amplitude. Note that as we filter at higher and higher frequencies, the PcP phase remains visible with about 20-30 percent of the maximum envelope height associated wit the P phase. This shows that PcP has not suffered the high-frequency attenuation observed for pP.

On Fig. 2.5b, a fourth peak is visible near t = 42-43 seconds. Examination of Fig. 2.5c indicates, however, that the frequency content of this particular peak is within the microseismic band.

The seismogram for a P-wavetrain from an earthquake in the Caucasus recorded at NORSAR (NORSAR Event 6277), is shown in Fig. 2.6a. It is clearly a very noisy record. This seismogram was processed by MARS, using the previously described method designed to eliminate noise.

The noise window was taken to be the section of the recording in Fig. 2.6a from t = 0 to t = 20 seconds, the spectrum of this portion is shown in Fig. 2.6b. The signal window was defined as the 51.2 second interval (1024 points at 20 points/second) following t = 20 seconds. The signal spectrum is plotted in Fig. 2.6c. Comparison of these two spectra makes clear the profound difference in frequency content between noise and signal.

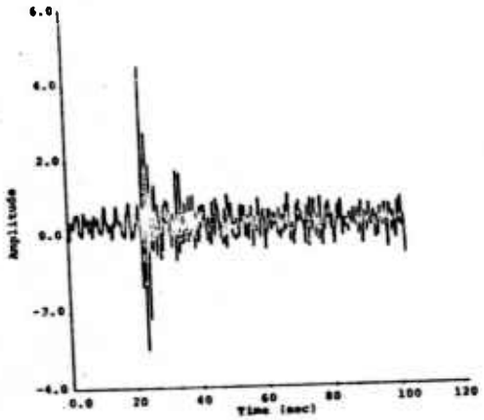

Figure 2.6a. Norsar Event 6277: Vertical displacement.

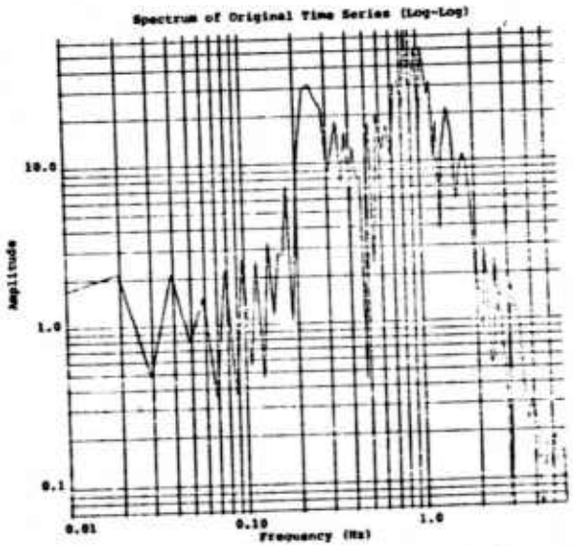

Figure 2.6c. Spectrum of signal window from Norsar 6277.

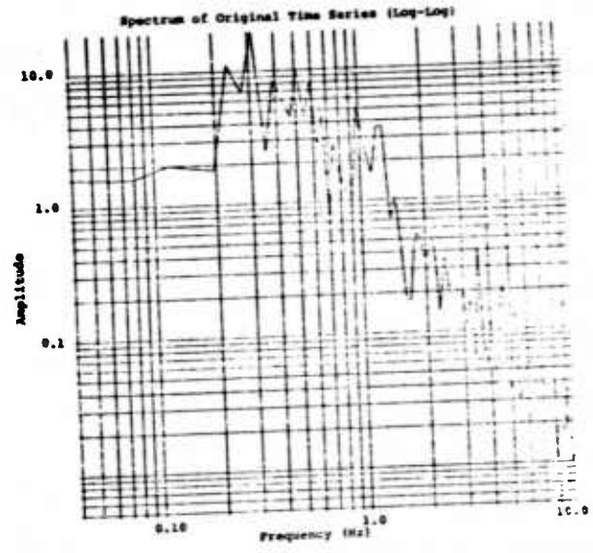

Figure 2.6b. Spectrum of noise window from Norsar 6277.

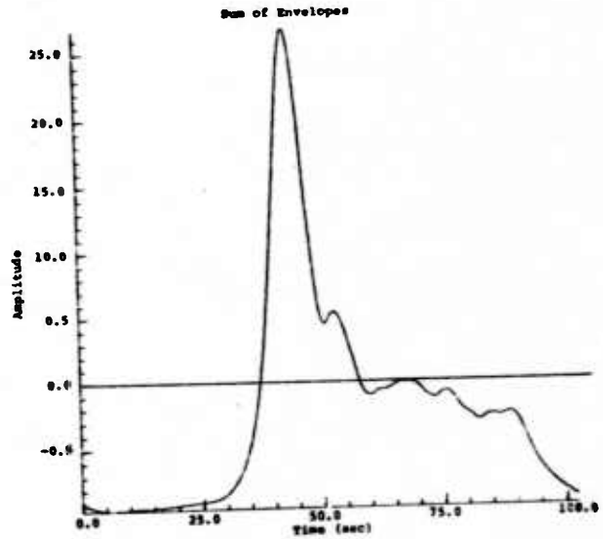

Figure 2.6d. Sum of ten envelopes, with noise level indicated, for Norsar 6277.

When the sum of envelopes is formed, with the appropriate noise correction subtracted from each individual envelope, the result is as shown in Fig. 2.6d. In this figure the straight line at zero amplitude indicates the noise level and eliminates all but two peaks. In this plot, the time scale has been shifted by an amount such that the signal window begins at t = 40 seconds. The largest peak, at t = 43 seconds, is then the direct P-wave arrival; the second peak is about 9 seconds later – a plausible delay time for pP, if the event was in the neighborhood of 35 km deep.

The individual envelopes for Event 6277 are shown in Fig. 2.6e, with the noise subtracted, an operation which causes the lowest frequency envelope (0.4 Hz) to virtually disappear due to the large amount of long-period background. In this display, the second arrival is not definitely indicated (it can best be seen in the f_c = 1.2 trace), showing that both types of display are necessary for a good signal evaluation.

2.9 POLARIZATION FILTERING

Given seismograms with more than one component of motion, it is possible to perform additional analysis based upon the phase correlation of the filtered particle motion. It is well-known, for example, that if $\hat{e}_z$ is a unit vector oriented vertically, and $\hat{e}_r$ is a unit vector pointing away from the source, the P-wave motion will tend to appear as

$$\underset{\sim}{X}(t) = f(t)\ [\hat{e}_r \cos\alpha + \hat{e}_z \sin\alpha] \quad ,$$

where α is the apparent emergence angle. SV waves will be given by

$$\underset{\sim}{X}(t) = g(t)\ [-\hat{e}_r \cos\alpha + \hat{e}_z \sin\alpha] \quad .$$

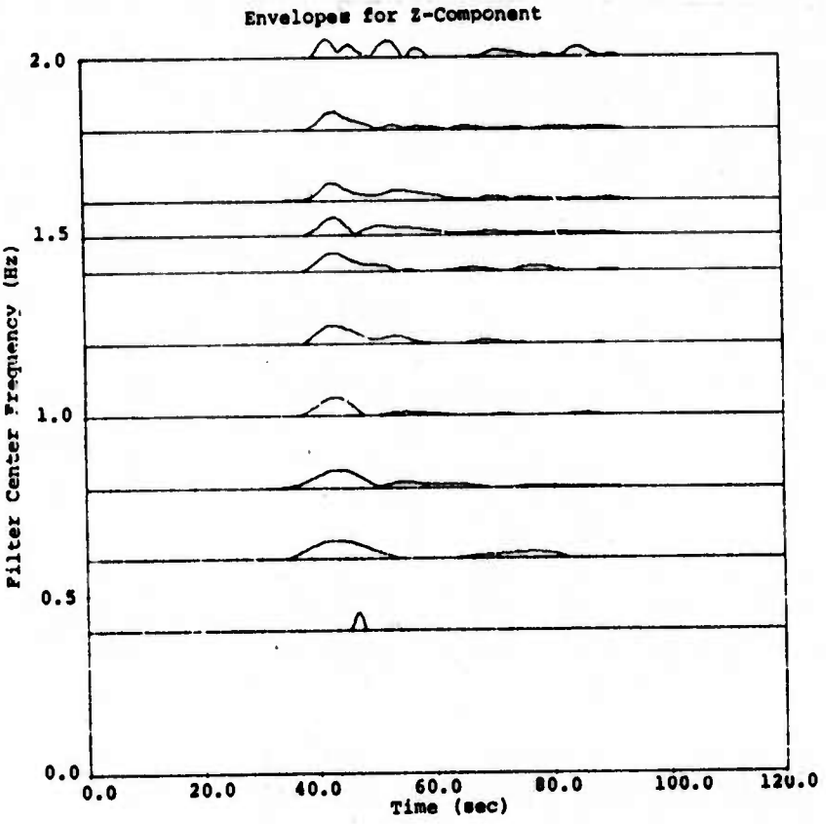

Figure 2.6e. Individual envelopes for Norsar 6277.

Both of these are linearly polarized in the z-r plane, the first being in phase, and the second, 180° out of phase.

Rayleigh waves, on the other hand, are elliptically polarized, having the form

$$\underset{\sim}{X}(t) = \hat{e}_r a \cos\phi(t) + \hat{e}_z b \sin\phi(t) \quad ,$$

so that the two components are 90° out of phase with one another. If the amplitude coefficients a and b are equal, then the polarization is circular, and Rayleigh wave motion is often close to this limit.

If both z- and r-component motion are measured simultaneously, narrow-band filtering can be performed on the two for the same filter frequencies and then, for each frequency, the linear polarization fraction can be defined using the instantaneous phases as

$$P_L(t) = \cos[\phi_z(t) - \phi_r(t)] \quad ,$$

and the circular polarization fraction as

$$P_C(t) = \sin[\phi_z(t) - \phi_r(t)] \quad .$$

Clearly,

$$P_L^2 + P_C^2 = 1 \quad ,$$

so that the two are, in a sense, mutually exclusive.

This method can be used to identify different signals as belonging to various wave types. Since frequency filtering is done before polarization filtering, the normal sort of low-frequency Rayleigh wave background noise can be excluded at an early stage, allowing the detection of higher frequency linearly-polarized information with greater sensitivity. If,

on the other hand, a P-wave and an SV-wave arrive simultaneously, then they may be indistinguishable from a higher-mode Rayleigh wave.

For z-r data, different types of waves can be identified as follows:

P-wave: $P_L > 0$ and $P_L > |P_C|$

SV-wave: $P_L < 0$ and $|P_L| > |P_C|$

Rayleigh wave: $P_C < 0$ and $|P_C| > |P_L|$

The case of $P_C > 0$ and $|P_C| > |P_L|$ can be taken to indicate either noise, or higher mode Rayleigh motion.

For waves which appear to be linearly polarized, an apparent emergence angle can be defined by

$$\alpha(t) = \text{Arctan}[S_z(t)/S_r(t)] \quad ,$$

while the ellipticity of other waves can be defined by

$$E(t) = S_z(t)/S_r(t) \quad .$$

If the data have not been rotated exactly towards the source, and if three Cartesian components are available, then the same analysis can be performed, comparing the vertical with each of the horizontal components separately. Correlation of the two analyses can then be used to indicate the apparent direction of the source; since differing frequency components will often be refracted differently, this apparent direction may be expected to vary somewhat with frequency.

Three-component data can also be used to identify Love waves. If the data have already been analytically rotated toward the source, then the transverse channel will contain mostly Love and SH waves. Should the signal not

have been rotated, then these wave types will be linearly polarized in the horizontal plane, with an angle which will indicate an apparent azimuth.

2.10 CONSTRUCTION OF POLARIZATION-FILTERED WAVES

A two-dimensional space can be constructed, the basis set of which consists of one linear and one circular component. The linear and circular polarization fractions for a given wave then indicate where the signal appears in such a space. The polarization fractions can be used to form projections into this space, where individual wave types can be easily picked out. For example, the P-wave envelope projection can be defined as

$$S_P(t) = \max(P_L(t),0) \cdot \sqrt{S_z^2(t) + S_r^2(t)} \quad ,$$

the SV-wave projection as

$$S_{SV}(t) = \max(-P_L(t),0) \cdot \sqrt{S_z^2(t) + S_r^2(t)} \quad ,$$

and the Rayleigh wave projection as

$$S_R(t) = \max(-P_C(t),0) \cdot \sqrt{S_z^2(t) + S_r^2(t)} \quad .$$

By evaluating these quantities for several frequencies, the appearance of different wave types can be observed and separated by polarization.

2.11 DEMONSTRATION OF POLARIZATION FILTERING FOR ARTIFICIAL SIGNALS

To test the polarization filtering method, an artificial two-component signal was prepared, with the intention that it look like a P-wave, followed by an SV-wave. Both

were represented by decaying sine-waves, the P-wave as

$$z(t) = r(t) = \theta(t-15)e^{-(t-15)/5} \sin(t-15)$$

and the SV as

$$z(t) = -r(t) = 0.4\ \theta(t-25)e^{-(t-25)/4} \sin\left[\frac{t-25}{0.75}\right] ,$$

where θ is the Heaviside step function. The two waves can be seen to have slightly different frequency content, as well as different decay times: The P-wave train should last a bit longer than the SV.

The z-component is shown in Fig. 2.7a, and the r in Fig. 2.7b. The SV-wave onset can be seen in the first diagram by a sharp break at t = 25; it is not visible in the second plot, and it is not obvious that this is anything but a single complicated wave. About 1 1/2 cycles separate the two waves, and so the P-wave will have to be observed during this time. In addition, detection of the SV-wave will be hampered by the coda of the first arrival, which has a larger initial amplitude and greater decay time.

This time-series (P and SV) was filtered by ten filters with center frequencies between 0.25 and 3.0. When the envelopes are summed, the result is as shown in Figs. 2.7c (for z) and 2.7d (for r). In both these cases, the SV arrival stands out clearly. The peaks for both arrivals, on both components, match the actual onset times quite accurately.

The individual envelopes are plotted in Figs. 2.7e and 2.7f. Here we see that the narrow-band filtering has done a very good job of separating the arrivals at the higher frequencies.

When the circular polarization fraction (P_C) is calculated for each filter center frequency, as a function of time, Fig. 2.7g, the results are essentially nil. Aside from

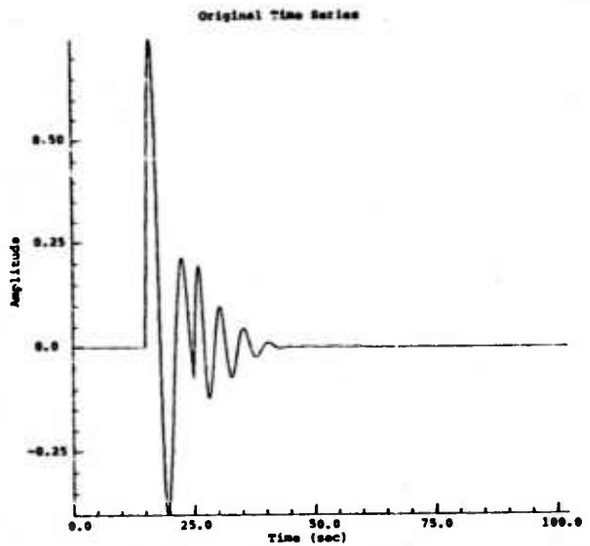

Figure 2.7a. Vertical component of displacement.

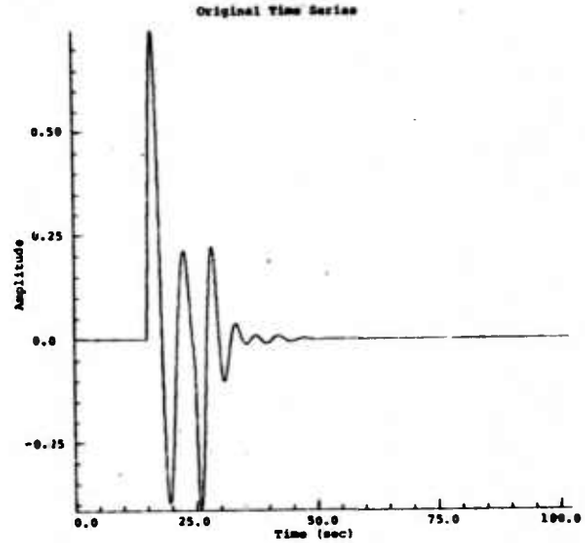

Figure 2.7b. Radial component of displacement.

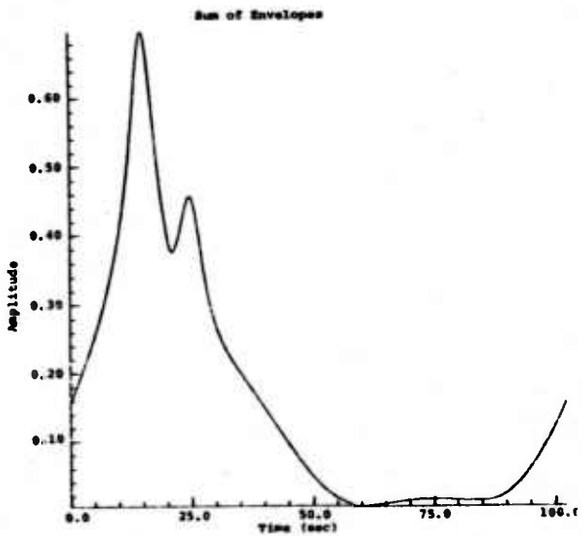

Figure 2.7c. Sum of envelopes derived from filtered vertical motion.

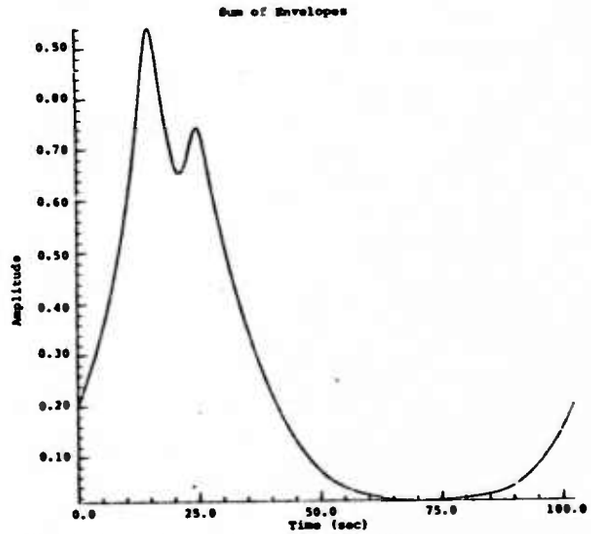

Figure 2.7d. Sum of envelopes derived from filtered radial motion.

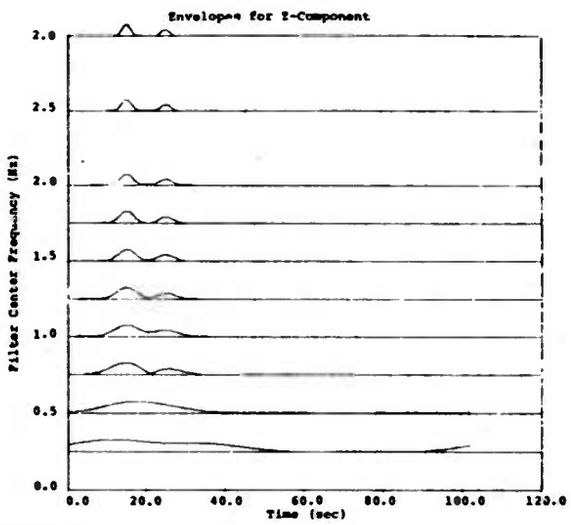

Figure 2.7e. Individual envelopes from filtered vertical displacement.

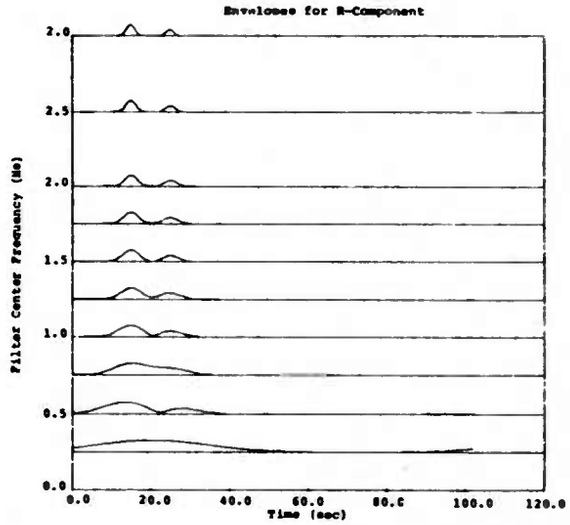

Figure 2.7f. Individual envelopes from filtered radial motion.

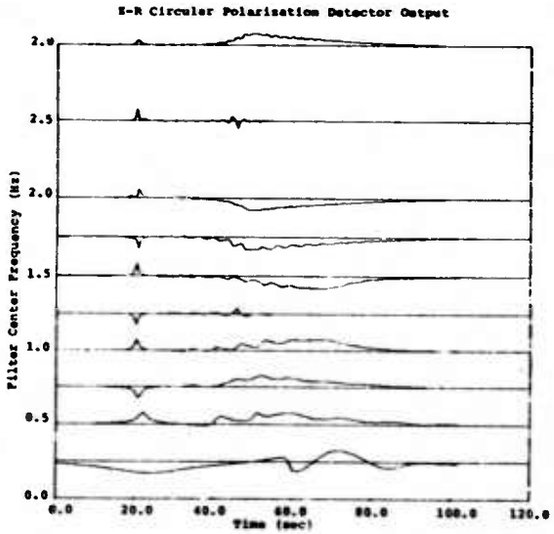

Figure 2.7g. Circular polarization fraction for the Z-R plane.

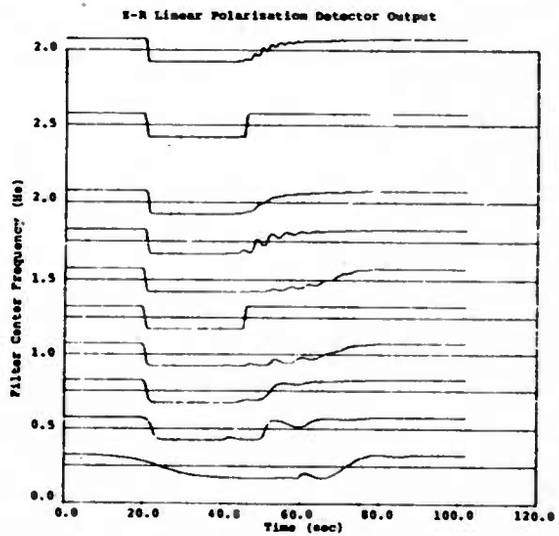

Figure 2.7h. Linear polarization fraction for the Z-R plane. Note the switch in sign near t = 25. showing separation of P and SV waves.

a spike near t = 20 (where it separates the P and SV waves), no significant circular arrivals can be seen.

The linear polarization fraction (P_L), in Fig. 2.7h, on the other hand, indicates the two wave types with great clarity. It can be seen that there is a nearly constant positive value (in fact, +1) at early times, switching rapidly to a value below zero (generally, -1) at t = 25. At much later times (t = 40-60), the lower damping of the P-wave makes itself felt, and its coda begins to dominate that of the shear excitation.

The Rayleigh wave projections (S_R) are plotted in Fig. 2.7i as functions of time, for the various filter frequencies. These data are quite inconsistent, every other filter indicating a different motion.

The P-wave (S_P, Fig. 2.7j) and SV-wave projections (S_{SV}, Fig. 2.7k) show very obvious arrivals. The lower resonant frequency of the P-wave results in the apparent delay of the SV-wave envelope at the lowest frequency — much more P-wave energy than SV arrives for this frequency, so that the latter has trouble making its appearance.

This test was then rerun, with a shorter delay time between the arrivals — the SV wave arrival time was advanced from t = 25 to t = 20 seconds. The z-component is shown in Fig. 2.8a, and the r in Fig. 2.8b. The second arrival is not easily seen in either of these records; the narrow-band filtering sum-of-envelopes plots (Figs. 2.8c and 2.8d) reveal its presence by a slight bump. Individual envelopes, in Figs. 2.8e (z-component) and 2.8f (r-component) show the shear wave at high filter frequencies. By looking at Fig. 2.8g, we can see the same strange behavior of the circular fraction as was observed earlier; the linear fraction, in Fig. 2.8h, however, still shows the very strong identification of the two waves with their different polarizations. The projected P-wave envelopes of Fig. 2.8i, and SV-wave envelopes of Fig. 2.8j are almost as they were in

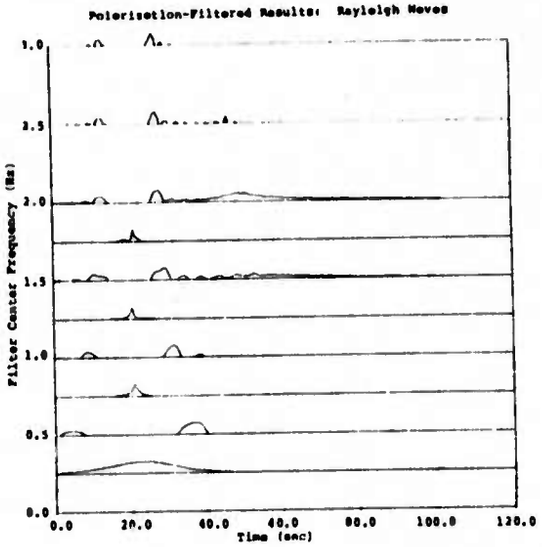

Figure 2.7i. Rayleigh wave projection, based upon circular polarization fraction.

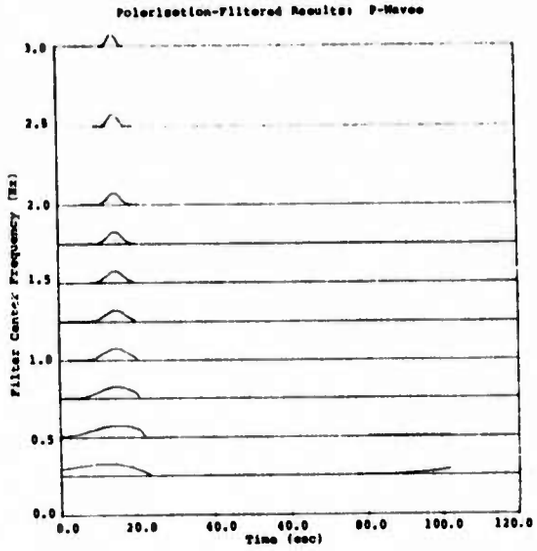

Figure 2.7j. P-wave projection, as obtained from linear polarization fraction.

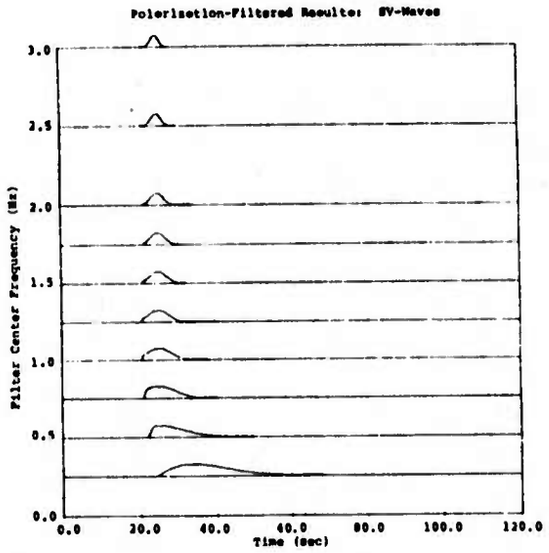

Figure 2.7k. SV-wave projection, as obtained from linear polarization fraction.

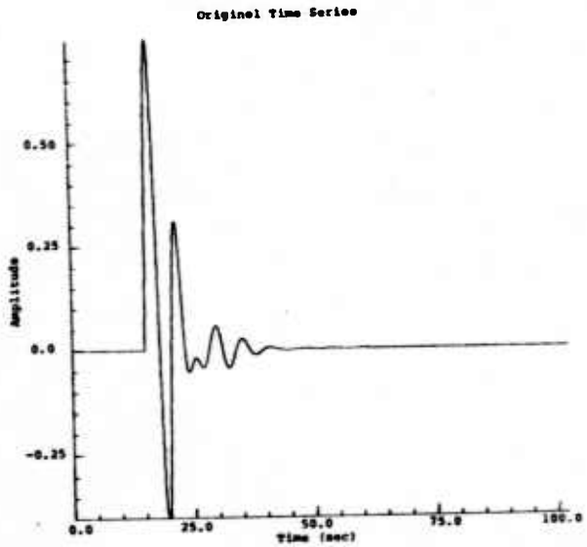

Figure 2.8a. Vertical component of motion, for second artificial event.

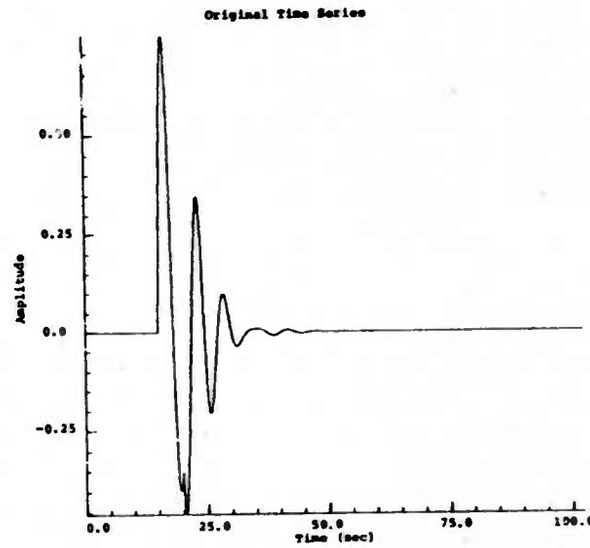

Figure 2.8b. Radial component of motion, for second artificial event.

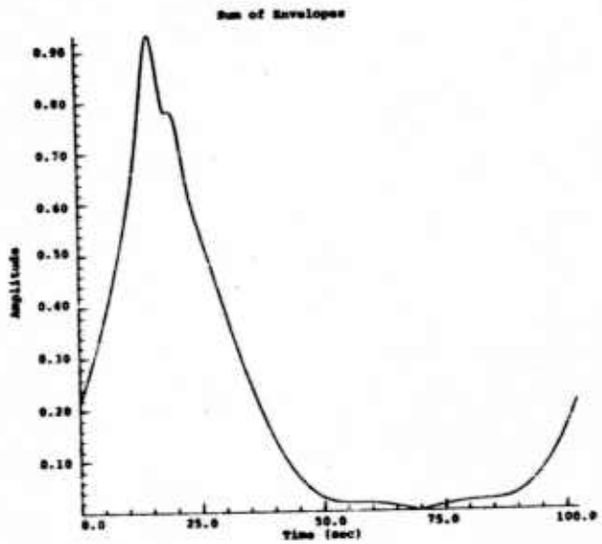

Figure 2.8c. Sum of envelopes resulting from filtered vertical motion.

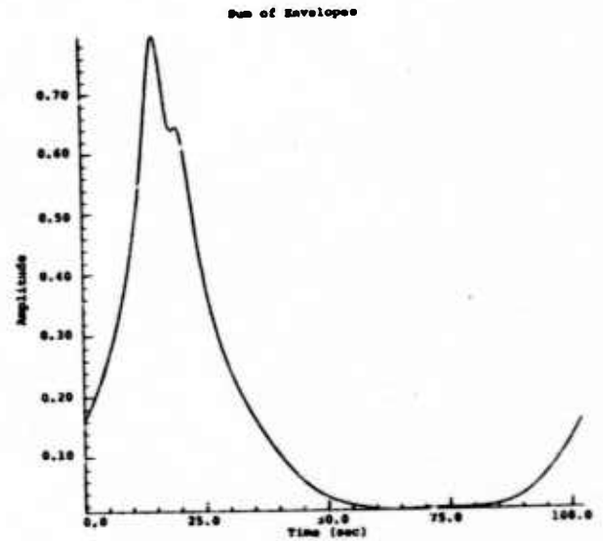

Figure 2.8d. Sum of envelopes resulting from filtered radial motion.

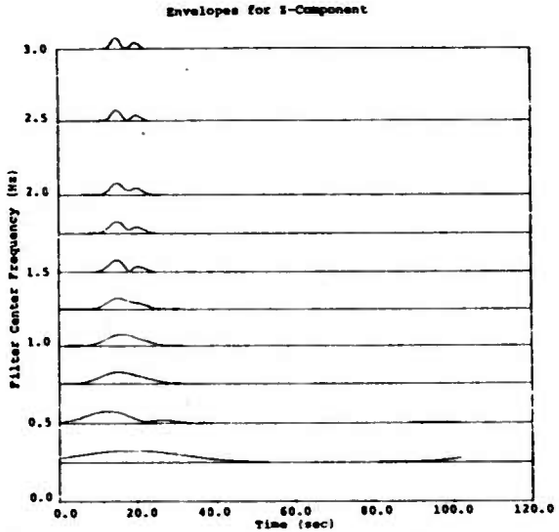

Figure 2.8e. Individual envelopes at various filter frequencies, for vertical component.

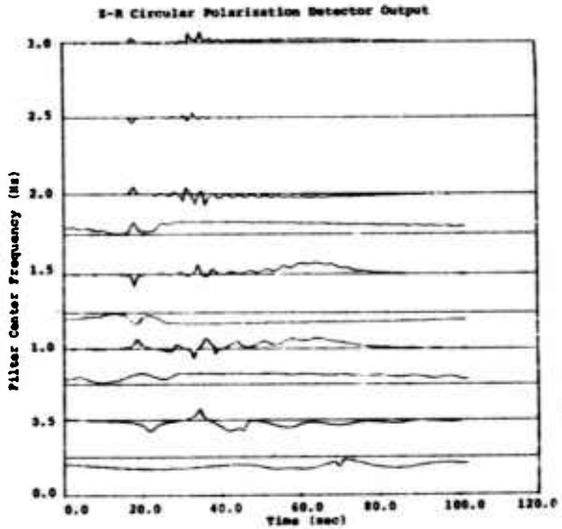

Figure 2.8g. Circular polarization fraction in the Z-R plane.

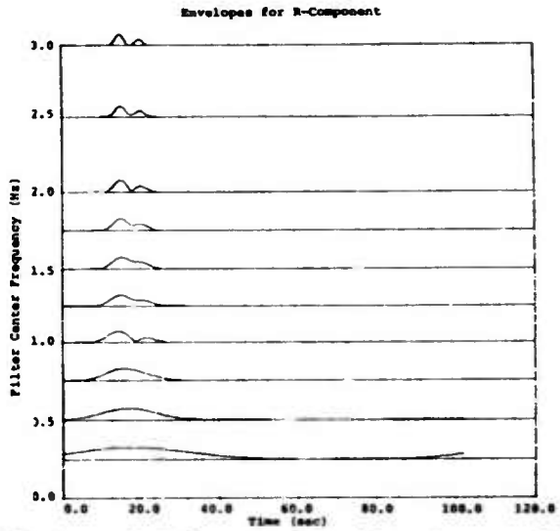

Figure 2.8f. Individual envelopes resulting from filtering radial component at different frequencies.

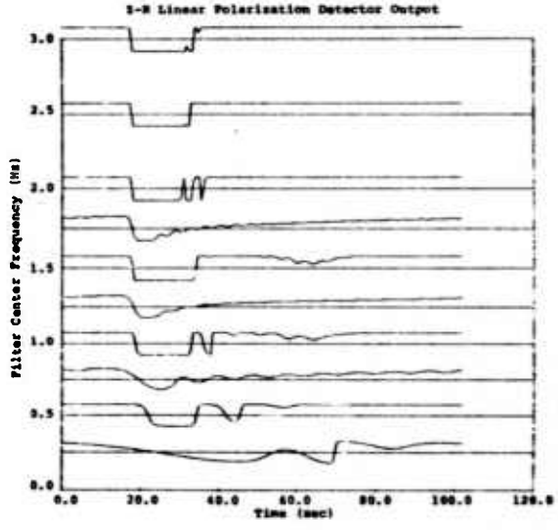

Figure 2.8h. Linear polarization in Z-R plane. Note that the separation between P and SV waves is still indicated, near t = 20.

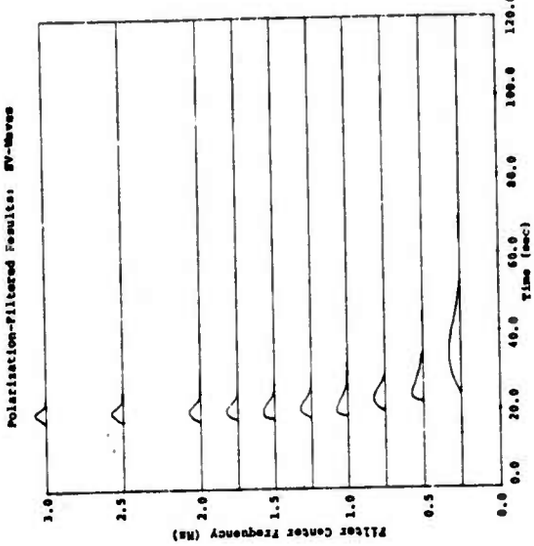

Figure 2.8j. SV-wave projection, using linear polarization fraction.

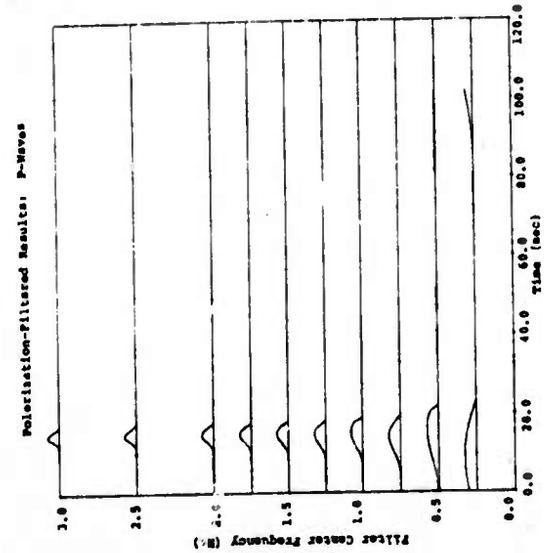

Figure 2.8i. P-wave projection, using linear polarization fraction.

the first case, demonstrating that the polarization analysis is still successful in locating the arrivals.

The test was then toughened by moving the shear wave forward some more: The P-wave now begins at t = 15, and the SV at t = 17.5. Figures 2.9a and 2.9b display the z and r displacements, respectively. No indication of the multiple-arrival nature can be seen by the eye on either of these plots. The narrow band discriminant fails, as the sum of z-envelopes, Fig. 2.9c, shows; the individual z-envelopes, Fig. 2.9d, indicate the second arrival clearly only at the highest frequency, although some of the lower frequencies exhibit a prolonged decline where the SV-wave should be.

The linear polarization fraction (Fig. 2.9e) is shaken, but not fooled. The SV-arrival is indicated plainly on three of the traces (f_c = 1.0, 2.0, and 3.0) and is hinted at by the other curves.

The P-waves are projected and drawn in Fig. 2.9f; their presence is evident. The appearance of SV-waves is also easily demonstrated in Fig. 2.9g, although again the lower frequencies suffer from P-wave domination.

2.12 POLARIZATION ANALYSIS OF SEVERAL OBSERVATIONAL EVENTS

Figures 2.10a and 2.10b show vertical, z, and radial, r, component seismograms, respectively, of ground motion from the Rex explosion at the Nevada Test Site (NTS) recorded at the LRSM station, RKON. These two records were processed by MARS for filters between 1 and 4 Hz, resulting in the envelopes shown in Figs. 2.10c and 2.10d. The displacement in the z-r plane was decomposed into circular (P_C) and linear (P_L) fractions, as exhibited in Figs. 2.10e and 2.10f.

A comparison between Figs. 2.10c, 2.10e, and 2.10f reveal this fact: When the envelopes are large, the circular fraction tends to be near zero, while the linear fraction is most likely

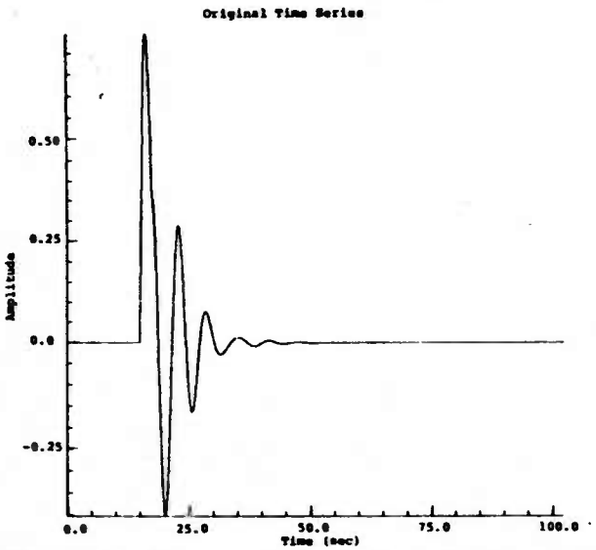

Figure 2.9a. Vertical component of motion for third artificial event. The P-wave begins at t = 15, and the SV-wave at t = 17.5.

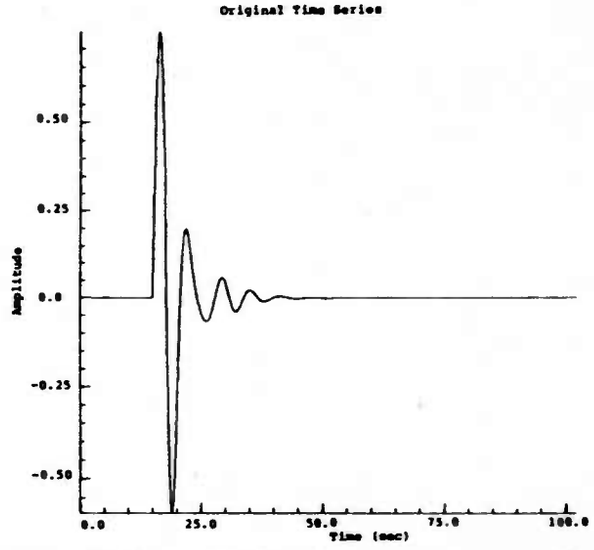

Figure 2.9b. Radial component of motion for third artificial event. Note that P and SV waves cannot be visually separated.

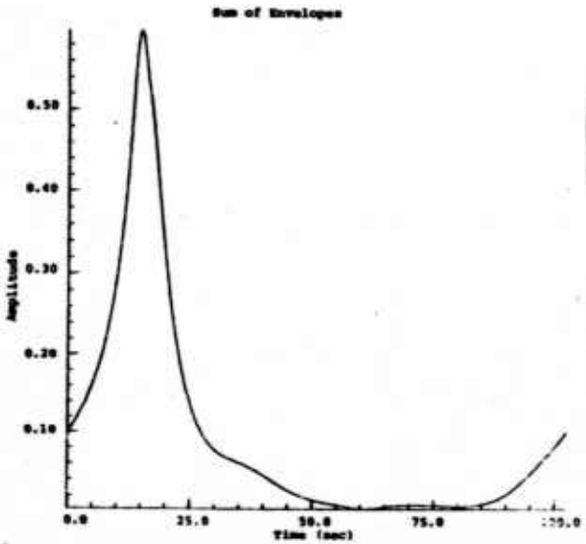

Figure 2.9c. Sum of envelopes from vertical motion. Observe that the two arrivals are not distinguishable.

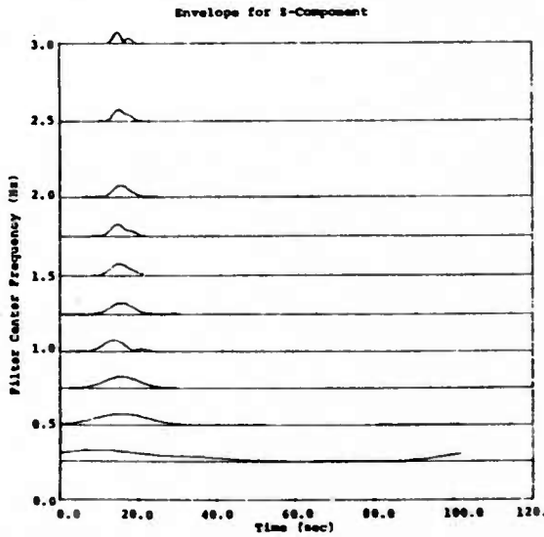

Figure 2.9d. Individual envelopes for filtered vertical motion. The second arrival is not clearly indicated.

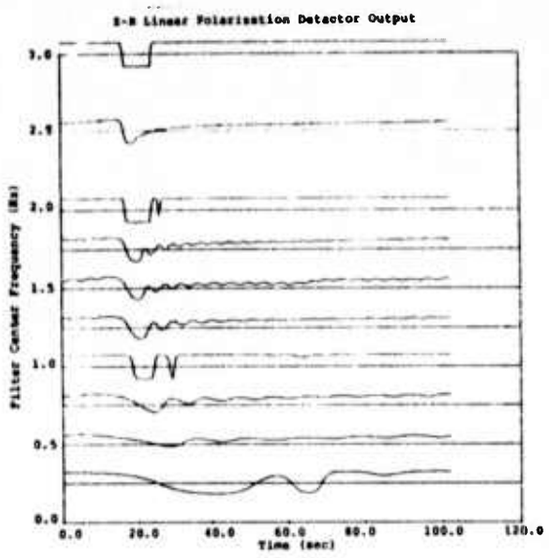

Figure 2.9e. Linear polarization fraction for the Z-R plane. Note that a change in polarization is consistently indicated near t = 17.5.

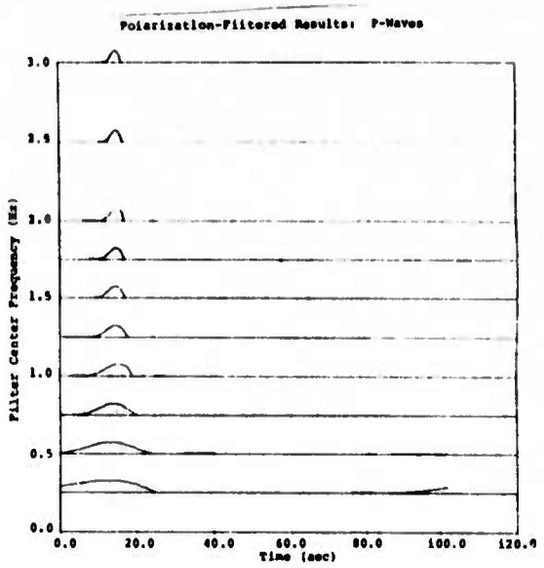

Figure 2.9f. Projected P-waves using linear polarization fraction of Fig. 2.9e.

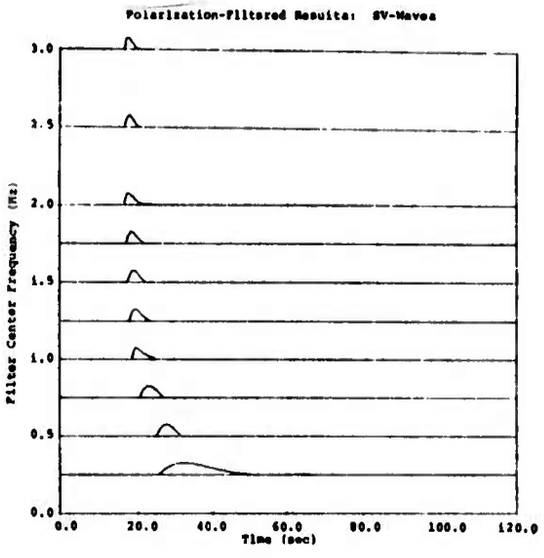

Figure 2.9g. SV-waves projection, using linear polarization fraction of Fig. 2.9e. Note that, for higher frequencies, the onset time is consistent.

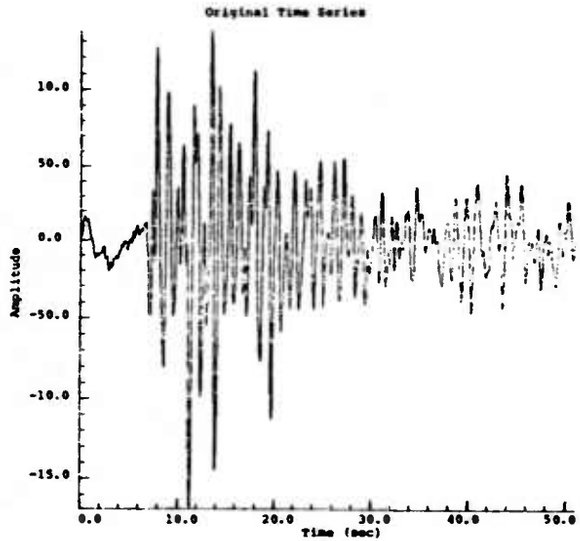

Figure 2.10a. Vertical component of displacement for Rex at RKON.

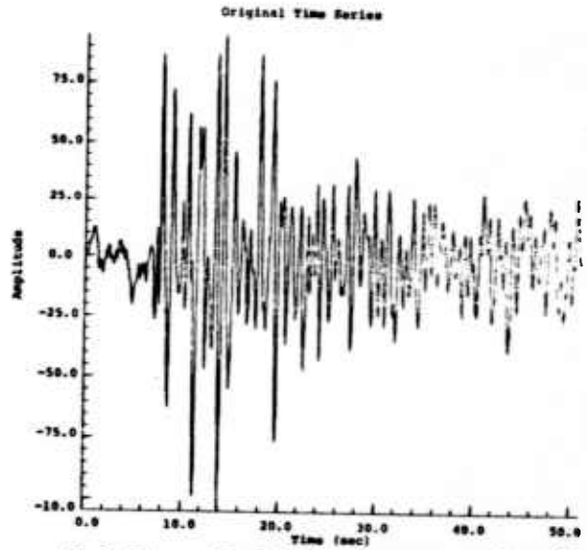

Figure 2.10b. Radial component of displacement for Rex at RKON.

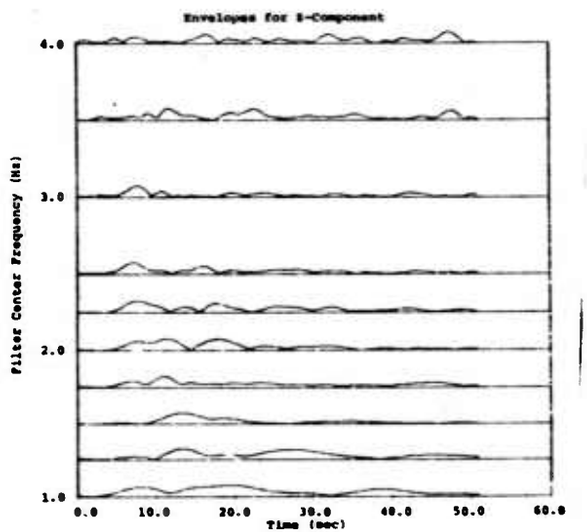

Figure 2.10c. Envelopes constructed from vertical displacement at RKON due to Rex.

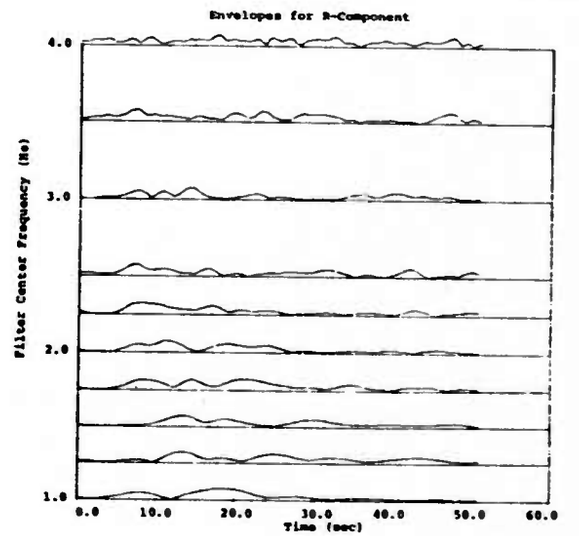

Figure 2.10d. Envelopes constructed from radial displacement at RKON due to Rex.

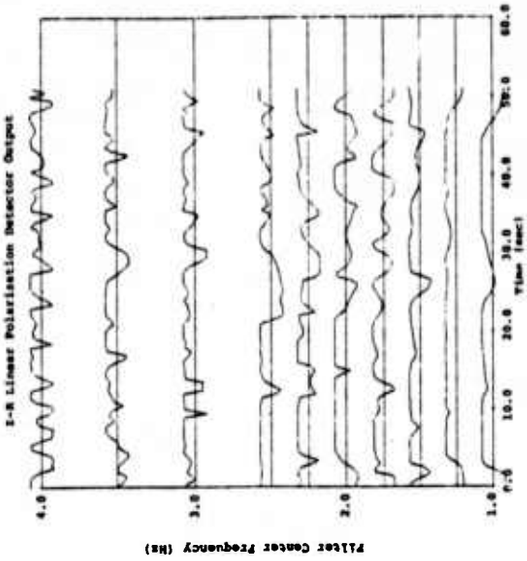

Figure 2.10f. Rex at RKON: Linear polarization fractions.

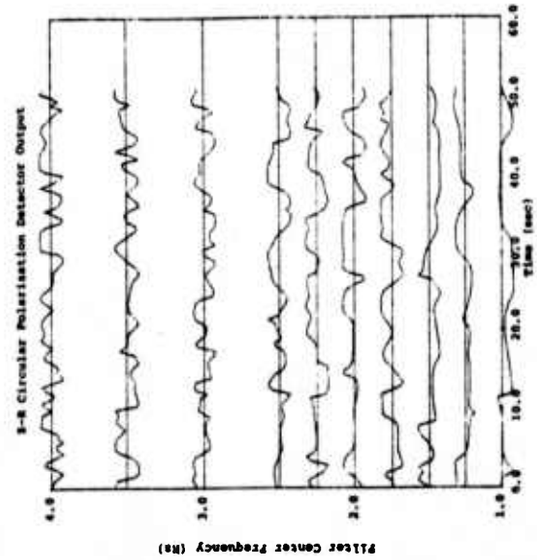

Figure 2.10e. Rex at RKON: Circular polarization fractions.

to be near +1 and flat. This is a very clear indication that the observed excitation is predominantly of a longitudinal (P-wave) nature.

When we attempt to construct the Rayleigh wave envelope projection (S_R), the results are ragged and inconsistent, as shown in Fig. 2.10g. A comparison of these traces with the envelope amplitudes show that Rayleigh waves, likely comprising the microseismic background, are indicated generally at times when no signal energy is arriving. It should be noted, in viewing this diagram, that each of the curves has been magnified so that its maximum value shows as a standard size on the plot; the relative lack of strength of this wave type is therefore not demonstrated.

Figure 2.10h shows the arrival of P-waves, as calculated by the P-wave projection (S_P). A comparison of this with Fig. 2.10c reveals that most of the envelope pulses are of this species, a fact which was noted earlier by observation of the polarization fractions. Figure 2.10i demonstrates the SV-waves, and this shows that the record is pretty clearly devoid of such excitations.

Figure 2.11a is the z-component of the NTS explosion, Greely, as measured at RKON. The corresponding r-component is shown in Fig. 2.11b while the z and r envelopes are in Figs. 2.11c and 2.11d, respectively. The circular polarization fraction (Fig. 2.11e) is basically uninteresting: When the envelopes show arrivals, this quantity is near zero, and nowhere can we see the broad, flat areas which indicate the arrival of a coherent wave. The linear polarization fraction (Fig. 2.11f), on the other hand, is just what one should expect if a definite wave type has arrived. The linear part is almost +1 at all times of significant arrival; the conclusion is that, without a doubt, we are looking at a P-wave arrival.

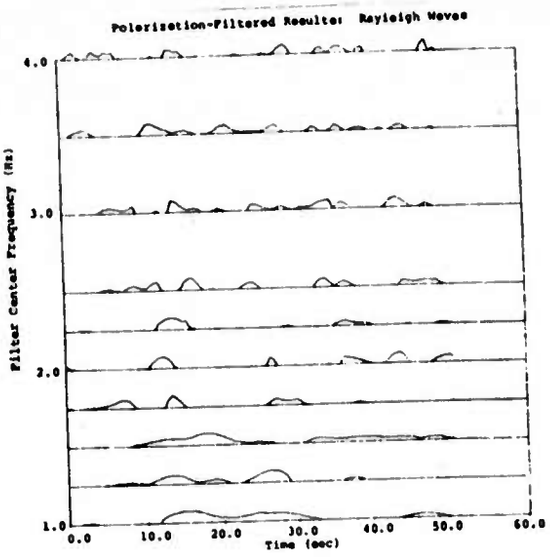

Figure 2.10g. Rex at RKON: Rayleigh wave projections.

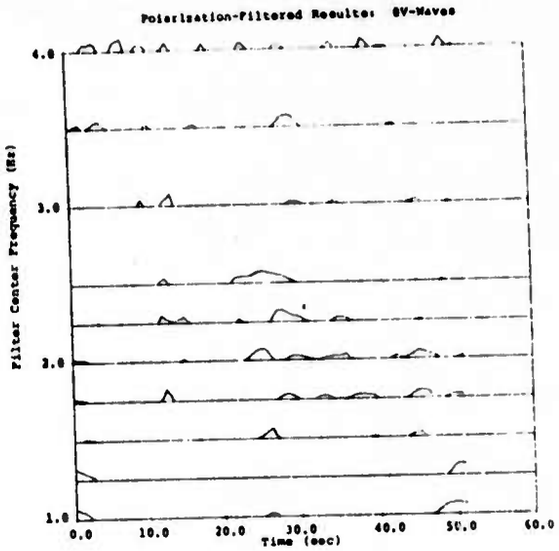

Figure 2.10i. Rex at RKON: SV-wave projections.

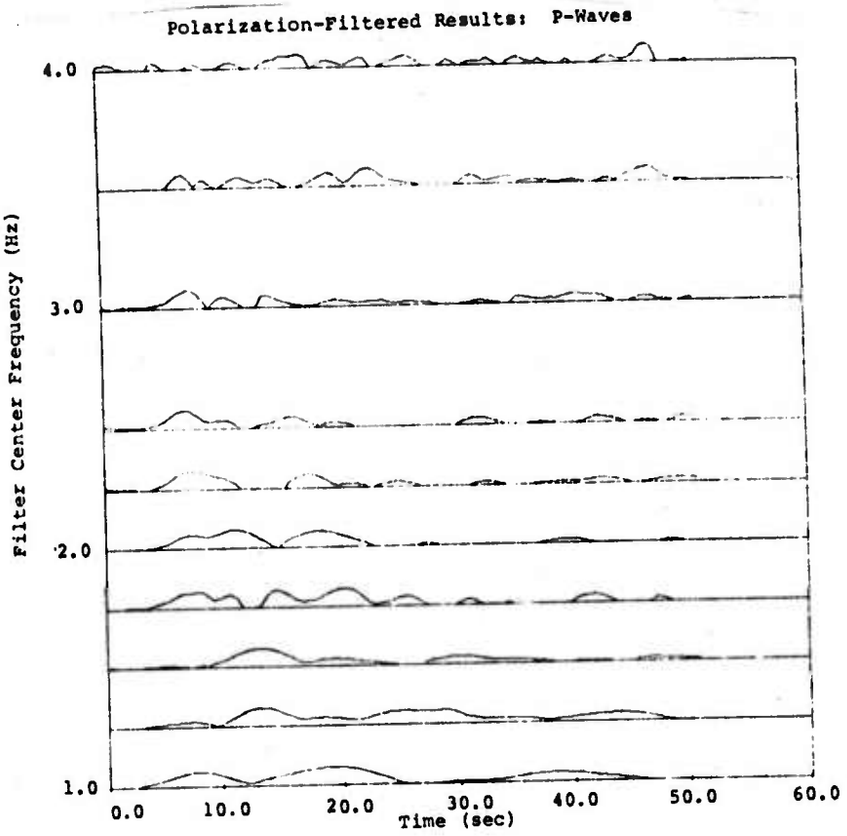

Figure 2.10h. Rex at RKON: P-wave projections.

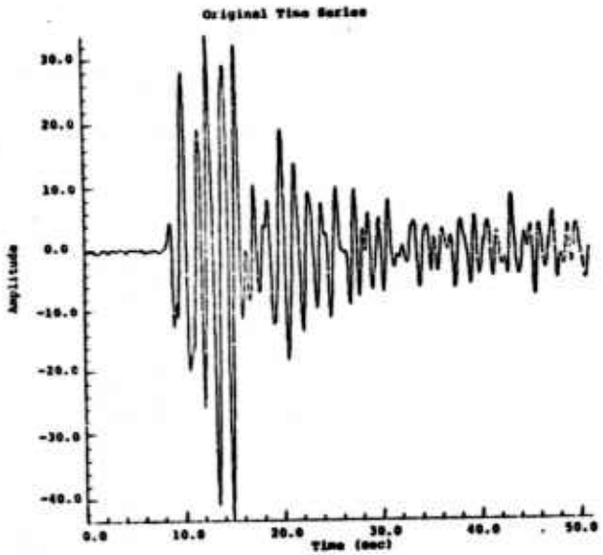

Figure 2.11a. Vertical component of displacement at RKON due to Greely.

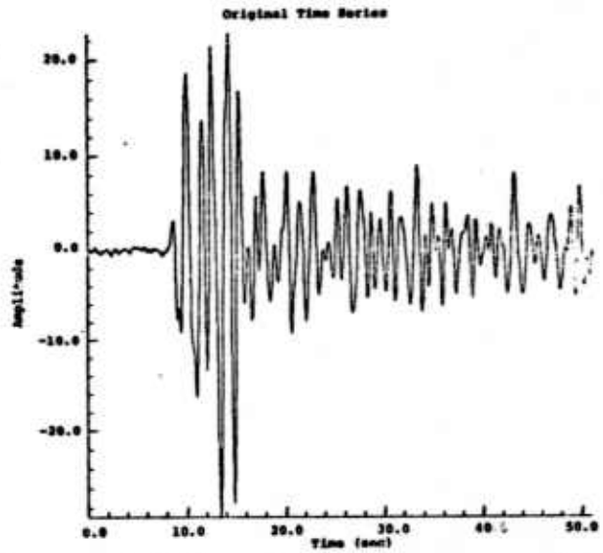

Figure 2.11b. Radial component of displacement at RKON due to Greely.

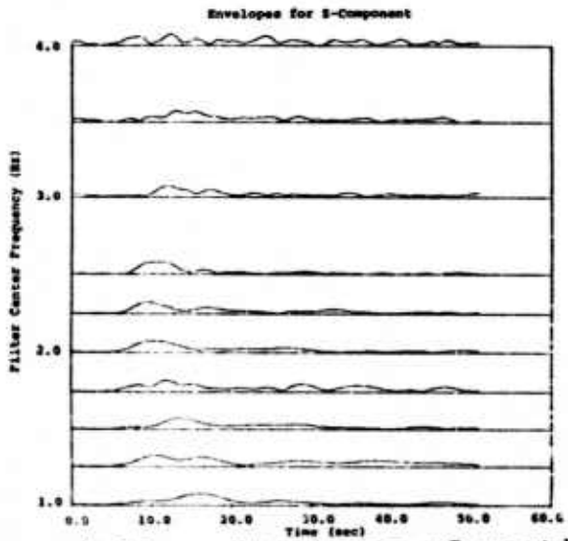

Figure 2.11c. Envelopes of vertical motion at RKON from Greely.

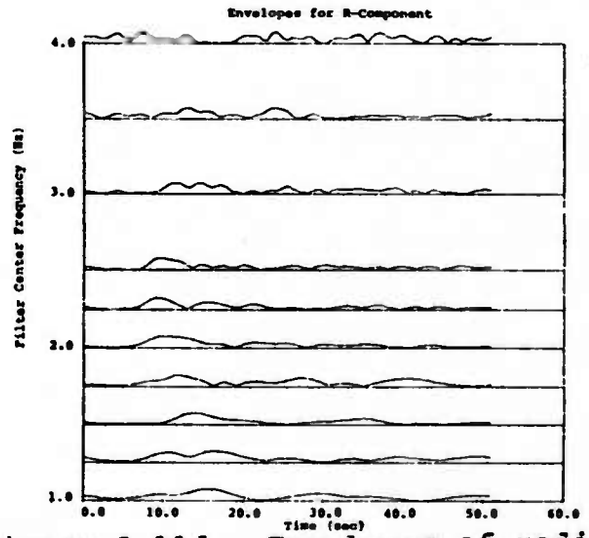

Figure 2.11d. Envelopes of radial motion at RKON from Greely.

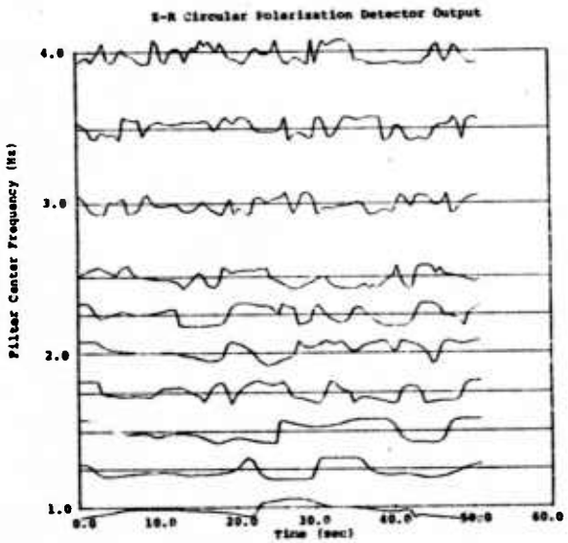

Figure 2.11e. Circular polarization fractions for Greely at RKON.

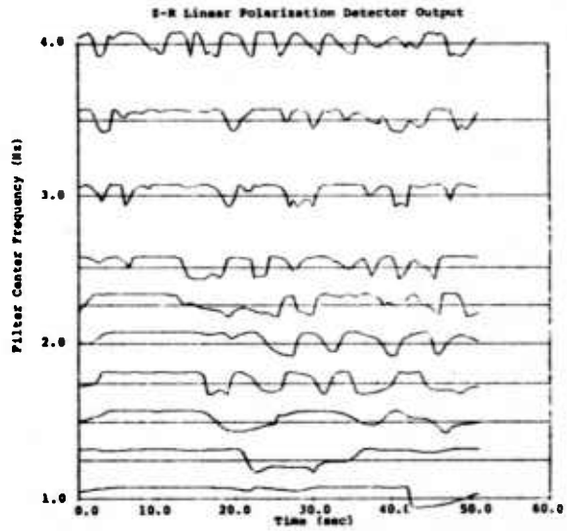

Figure 2.11f. Linear polarization fractions for Greely at RKON.

The projected Rayleigh (Fig. 2.11g), SV (Fig. 2.11h), and P waves (Fig. 2.11i) verify that result. All of the significant peaks in the z-envelope have been projected as longitudinal rectilinear waves.

The Piledriver explosion, recorded on the long-period instruments at RKON, is shown in Fig. 2.12a (z-component) and 2.12b (r-component). The envelopes due to filtering at different frequencies are in Figs. 2.12c and 2.12d. The arrival time is manifestly different for different center frequencies, with the low frequency energy arriving first. The variation of peak arrival time with frequency is smooth and continuous, making it evident that this is due to a single arrival, rather than several overlapping arrivals. This is obviously an Airy phase.

The circular polarization fraction (Fig. 2.12e) is also easy to interpret: The envelope peaks correspond to areas of strong and consistent negative circularity – this is a Rayleigh wave. The linear fraction, Fig. 2.12f, on the other hand, avoids the peaks. In Fig. 2.12g, the Rayleigh waves have been projected out, and the Airy phase dispersal is again plainly demonstrated.

Figure 2.13a is the transverse component of the same event. A Love wave can be observed, which arrives earlier than the Rayleigh. The arrival time diagram for this (Fig. 2.13b) also shows the unusual pattern characteristic of an Airy effect.

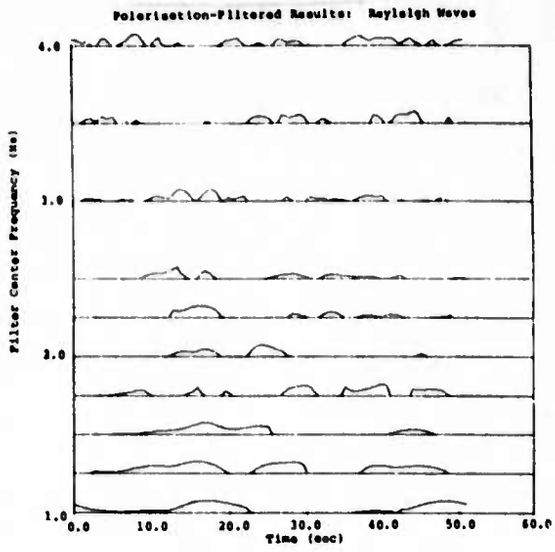

Figure 2.11g. Greely at RKON: Rayleigh wave projections.

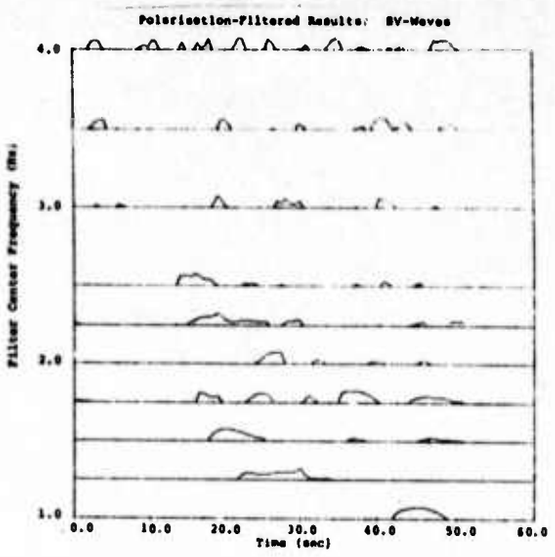

Figure 2.11h. Greely at RKON: SV-wave projections.

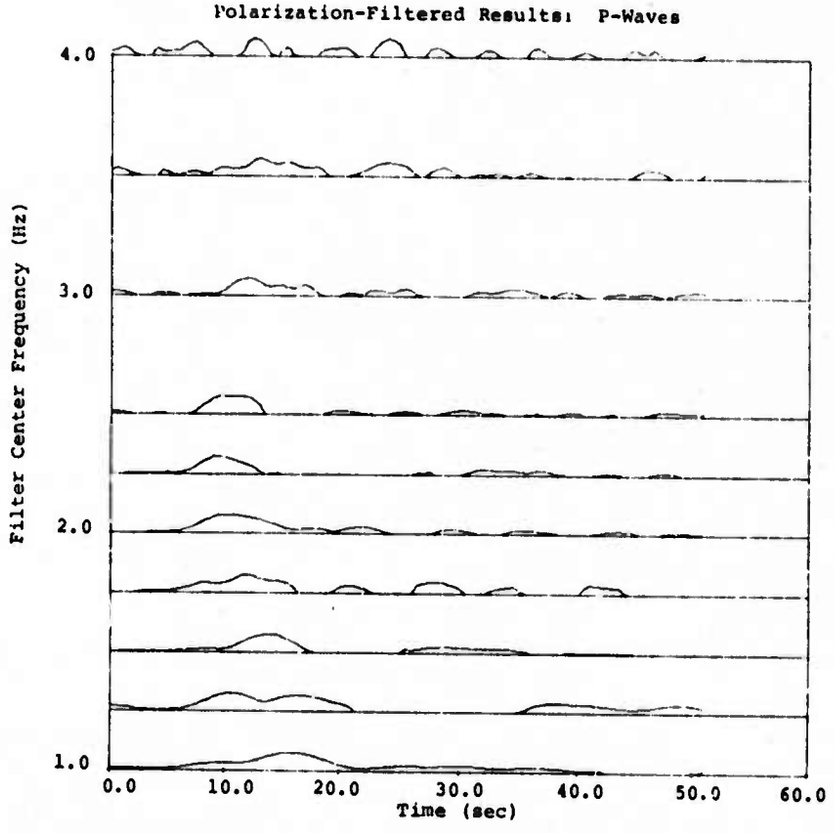

Figure 2.11i. Greely at RKON: P-wave projections.

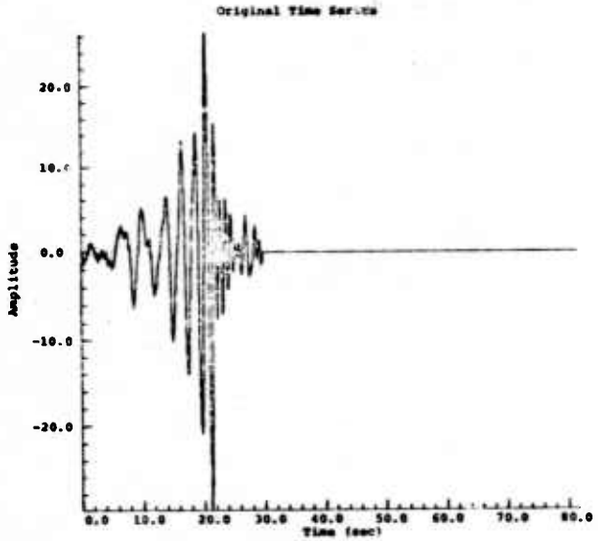

Figure 2.12a. Vertical displacement at RKON due to Piledriver.

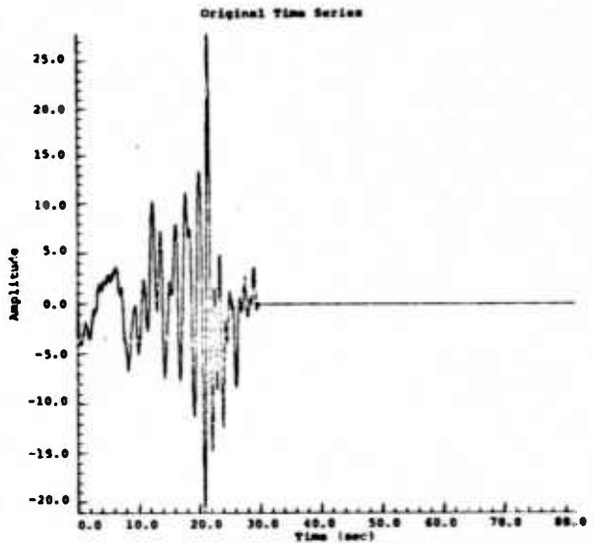

Figure 2.12b. Radial displacement at RKON due to Piledriver.

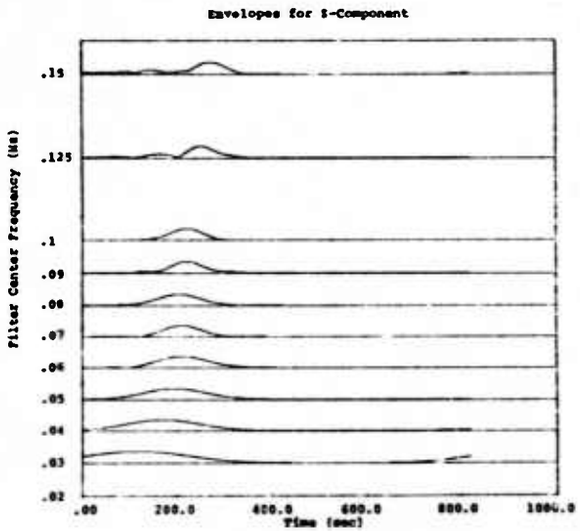

Figure 2.12c. Vertical component envelopes of Piledriver, observed at RKON.

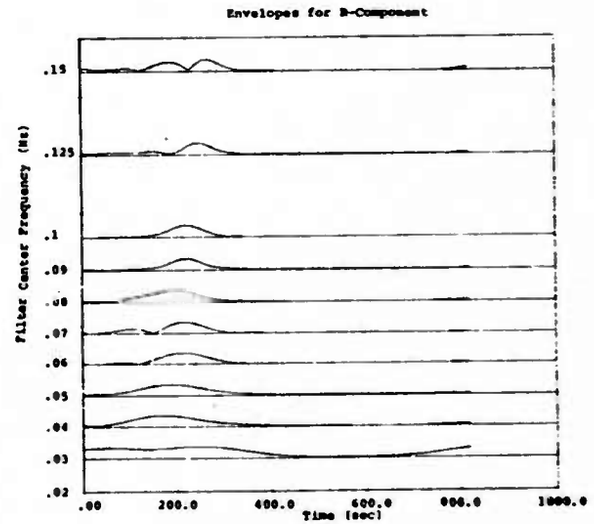

Figure 2.12d. Radial component envelopes of Piledriver, observed at RKON.

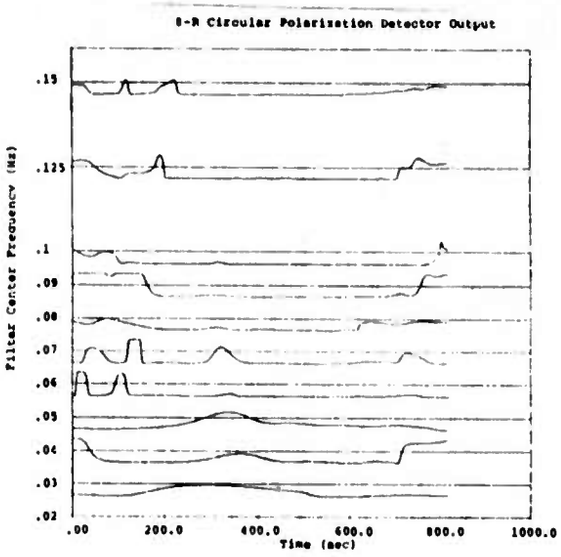

Figure 2.12e. Circular polarization fraction for Piledriver at RKON.

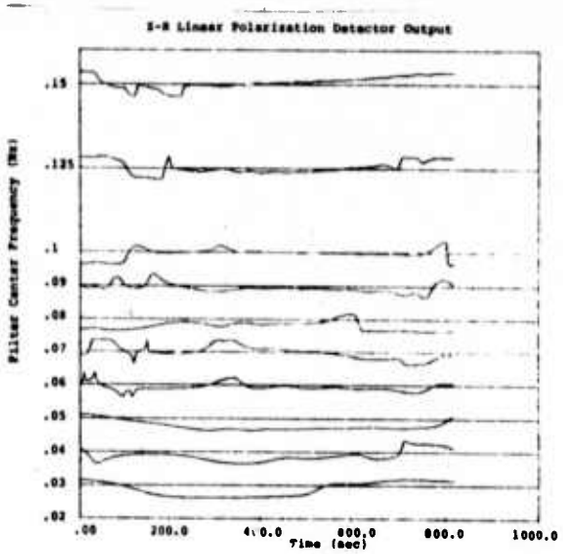

Figure 2.12f. Linear polarization fraction for Piledriver at RKON.

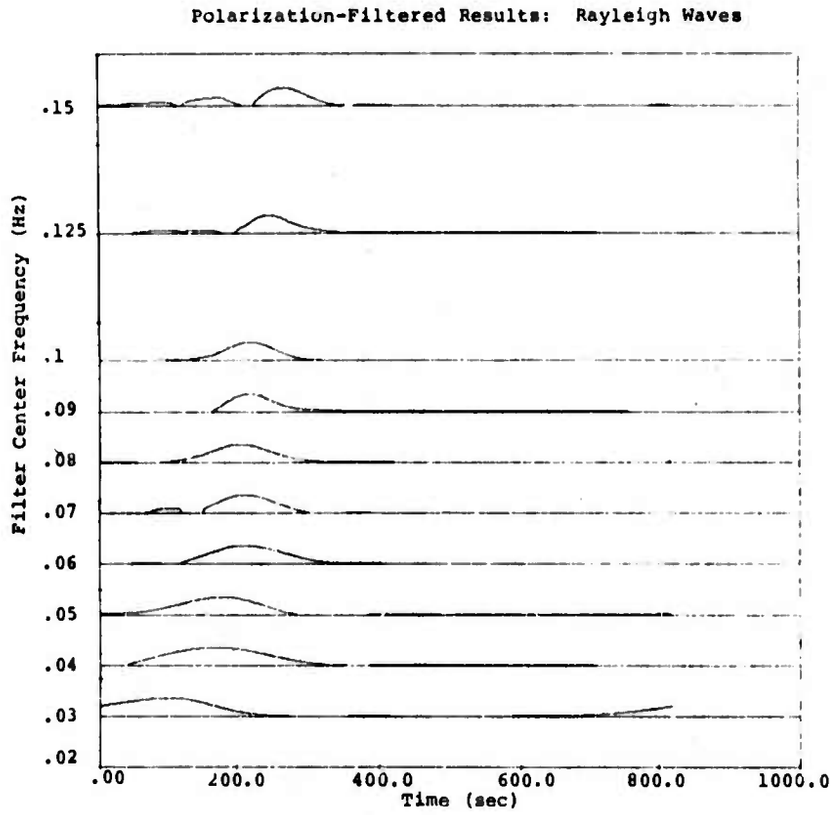

Figure 2.12g. Rayleigh wave projection from Piledriver at RKON.

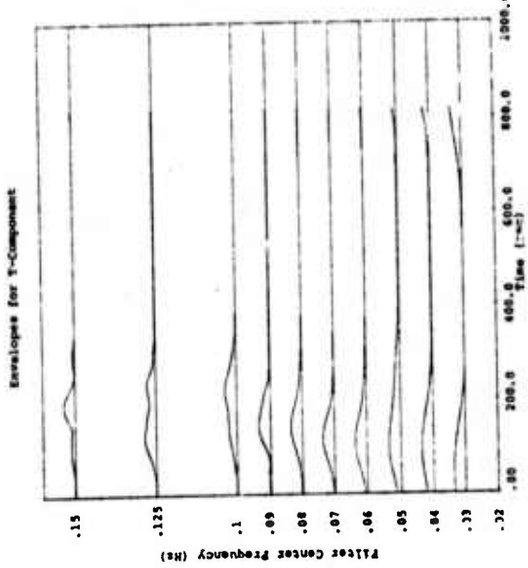

Figure 2.13b. Envelopes for transverse component of displacement from piledriver at RKON.

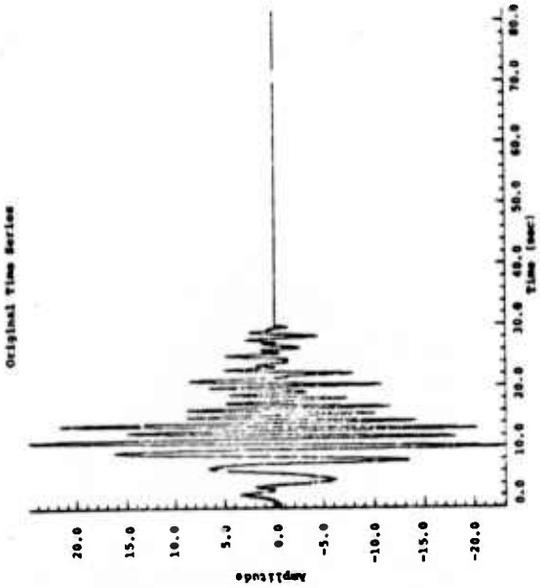

Figure 2.13a. Transverse motion at RKON from the piledriver event.

III. VARIABLE FREQUENCY MAGNITUDE DISCRIMINANT

3.1 INTRODUCTION

In a previous report (Bache, et al., 1975a) written under this contract, the formulation and results of extensive testing of a variable frequency magnitude (VFM) discriminant which exploits spectral differences between earthquakes and underground explosions were presented in detail. In addition to providing discrimination of a large population of shallow Eurasian earthquakes and presumed explosions recorded at the LASA and NORSAR arrays, it was shown that the VFM technique can discriminate a multiple explosion scenario as well. A particularly significant aspect of the VFM technique is that its application is dependent on recording short-period P-waves from events and not long-period surface waves. Thus, positive discrimination can be tested for on events (explosions) down to a much lower magnitude threshold level than is possible with the traditional $M_s - m_b$ method.

In the following sub-sections of this report we will present preliminary results on the application of the VFM technique to a large population of North American events recorded in Canada. This section will conclude with a comparison of all the VFM discrimination tests conducted to date.

3.2 NORTH AMERICAN EVENTS RECORDED IN CANADA

Data in digital format for a large population of North American earthquakes and underground explosions recorded at the 19-element short-period Yellowknife array in Canada (Manchee and Somers, 1966) were recently acquired. These data consist of vertical-component recordings of P-wave trains (preceded by at least 25 seconds of background noise) from approximately 40 earthquakes occurring in the Gulf of

California and 49 underground explosions detonated at the Nevada Test Site (NTS). While signals recorded on all 19 array elements were supplied for most of the events in the data base, our first test for discrimination with the VFM technique was performed on single-element (sensor B5 located at the crossover point of the L-shaped array arms) recordings only.

Examples of P-wave trains from two NTS explosions and two Gulf of California earthquakes recorded by the single sensor B5 of the 19-element Yellowknife array are shown in Figs. 3.1a-3.1d. These particular time series were chosen for display to give some indication of the variation in signal-to-noise ratio (S/N) of the different event signals in the data base. For instance, the S/N for the NTS explosion Wagtail (Fig. 3.1a) is more than a factor of ten higher than the S/N for the explosion Diana Mist (Fig. 3.1b).

Each of the time series tested for discrimination in this study was first divided into a noise sample and a signal sample. In the case of the explosions, both noise and signal windows were chosen to be 24 seconds long. For the earthquakes, a 24 second noise window and signal windows up to 66 seconds in duration were examined. The longer duration of the earthquake signal windows was dictated because of the difficulty in identifying the exact signal onset time. Each noise and signal window was demeaned and tapered with a cosine bell applied to 10 percent of both window ends.

The procedure employed to compute the variable frequency magnitudes was described in detail in the previous section of this report. As described there, estimates of magnitude at different frequencies are based on the peak amplitudes of the envelopes of narrow band filters applied to the signals of interest. The peak <u>signal</u> filter amplitudes were corrected for <u>noise</u> based on estimates made from

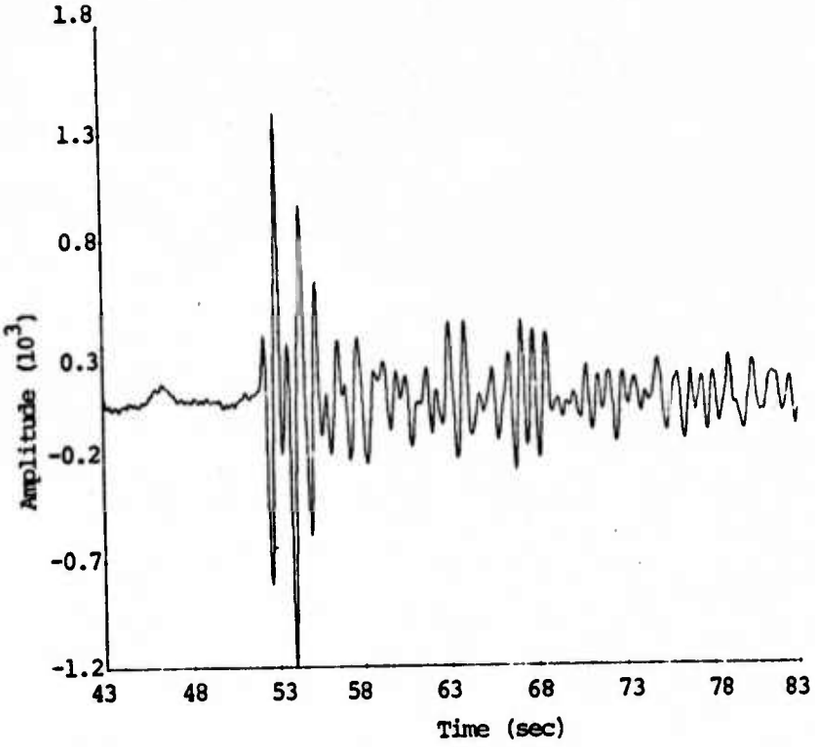

Figure 3.1a. Time series corresponding to an m_b = 5.3 NTS explosion, Wagtail, recorded at the Yellowknife array in Canada.

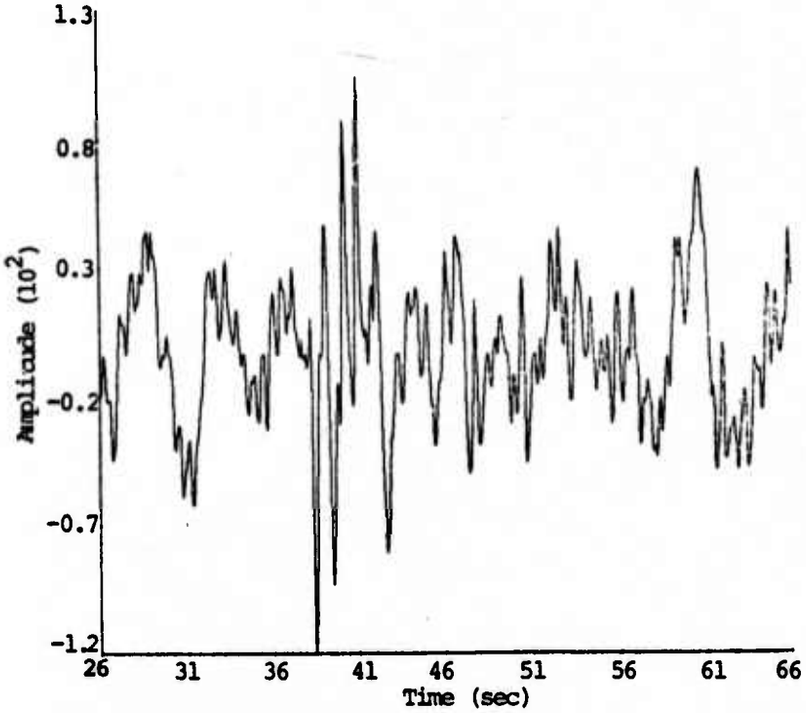

Figure 3.1b. YKA short-period recording of the m_b = 4.6 NTS explosion, Diana Mist.

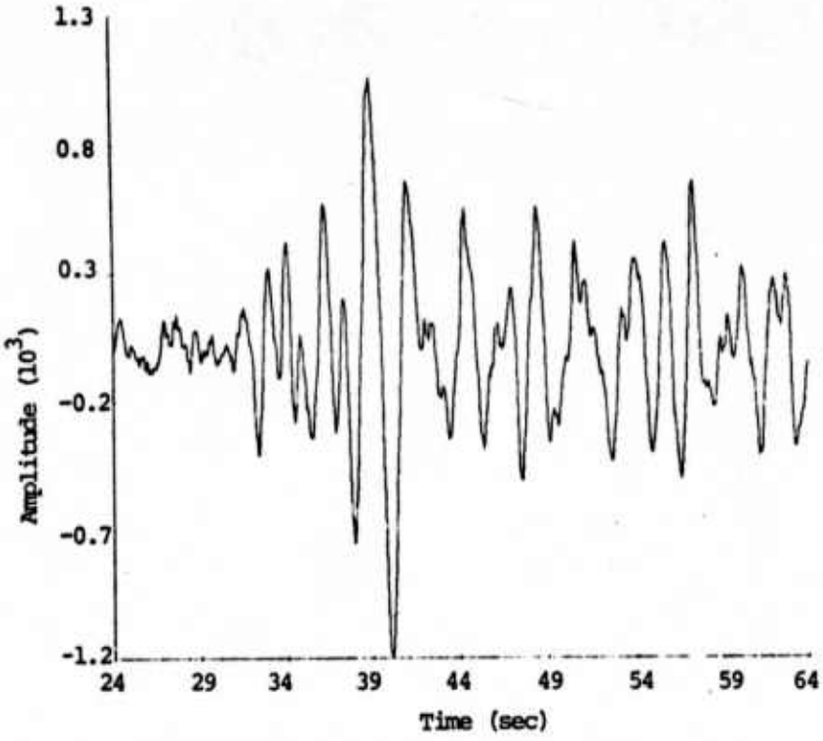

Figure 3.1c. YKA short-period recording of an m_b = 5.3 Gulf of California earthquake.

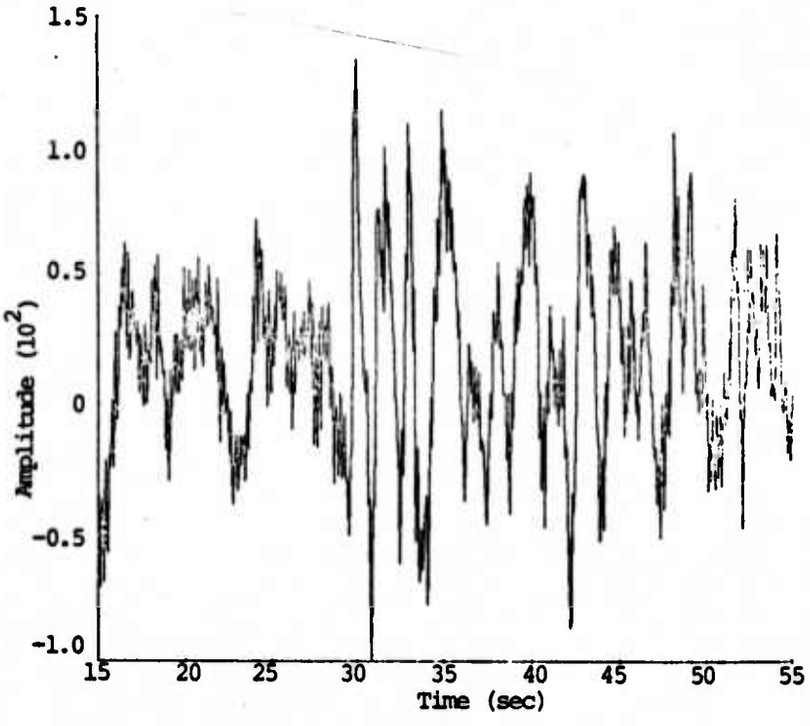

Figure 3.1d. YKA short-period recording of a small (m_b = 4.8) Gulf of California earthquake.

the 24 second noise windows preceding each signal. In the present VFM discrimination test of the Yellowknife data base, twenty filters with center frequencies ranging from 0.25 Hz to 4.0 Hz were applied to each noise and signal time series. The preliminary results of this test are discussed in the following sub-section of this report.

3.3 RESULTS OF THE VFM DISCRIMINATION TEST

As mentioned above, each of the signal time series was filtered by twenty narrow band filters with center frequencies ranging from 0.25 Hz to 4.0 Hz. The frequency range was decided on after examining spectra of ten different earthquakes and explosions. Magnitude estimates, $m_b(f)$, based on a narrow band filter with a relatively low center frequency, f_c, were then plotted versus estimates based on high frequency filters. This was repeated for various combinations of center frequencies and all of the plots were then examined for discrimination.

Figure 3.2 shows preliminary results for the North American data base. The filter center frequencies that have yielded the best discrimination results to date are, as indicated, 0.425 Hz and 2.5 Hz. In this figure the Gulf of California earthquakes are denoted by the open circles, the NTS explosions by the x's. In general most of the earthquakes on this figure, which are reported in the Preliminary Determination of Epicenters to be shallow focus, separate from the explosion population. However, compared with the VFM discrimination results previously obtained for Eurasian events recorded at LASA (Fig. 3.3) the results in Fig. 3.2 are not nearly as impressive in terms of complete separation of earthquake and explosion populations.

Before we can draw any firm conclusions about the data set in Fig. 3.2 more will have to be learned about

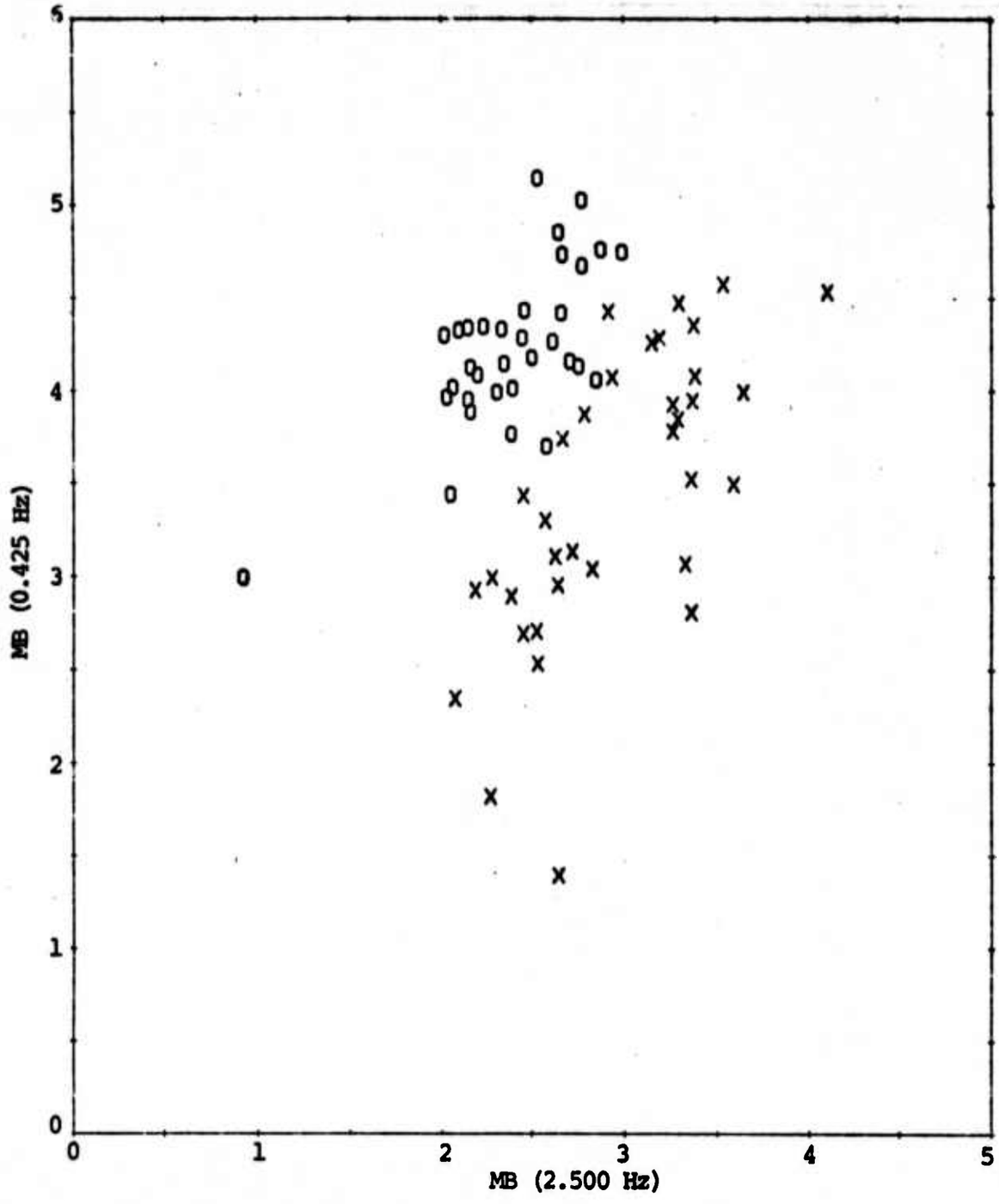

Figure 3.2. Variable frequency magnitude estimates, $m_b(f)$, computed at 0.425 Hz and 2.5 Hz for a population of Gulf of California earthquakes (O's) and NTS explosions (X's).

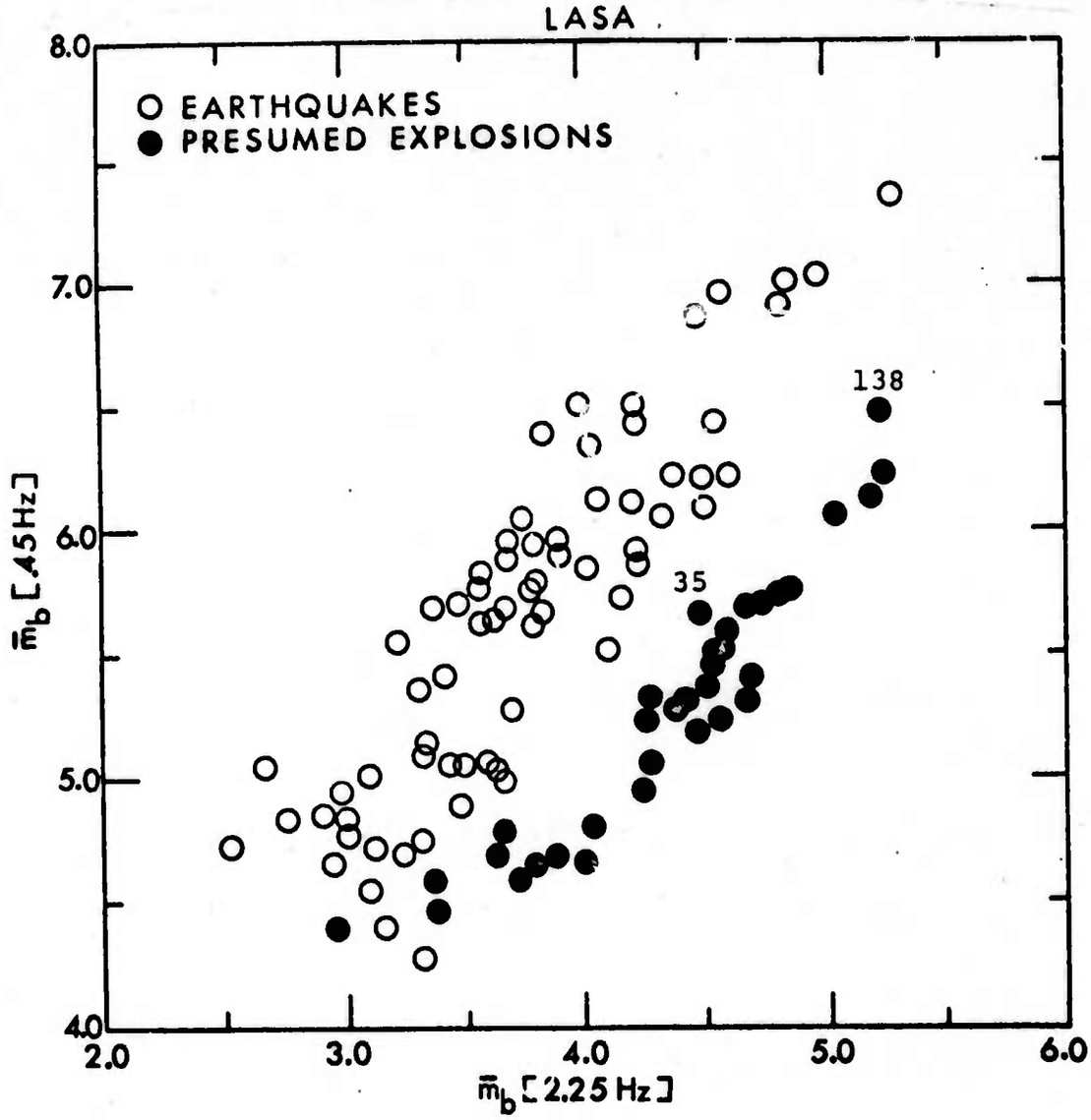

Figure 3.3. Spectral magnitudes, $\bar{m}_b$, computed at 0.45 Hz and 2.25 Hz. The presumed explosions numbered 35 and 138 occurred at Novaya Zemlya.

those earthquakes that overlap part of the explosion population. Note, however, that a very important and positive point about the populations in this figure is the complete separation of the very small magnitude events.

3.4 SUMMARY

A large population of North American events, namely Gulf of California earthquakes and NTS explosions, were tested for discrimination using the VFM technique. For certain combinations of low versus high filter center frequencies, a plot of the variable frequency magnitude estimates resulted in general discrimination of the earthquake and explosion populations, with some overlap of the two populations. While the degree of discrimination obtained to date is less for the North American event populations than for Eurasian event populations previously studied, it must be pointed out that complete separation of those Gulf of California earthquakes and NTS explosions with m_b (NOAA) values between 4.0 and 4.5 was achieved.

IV. THE EFFECT OF TECTONIC RELEASE ON THE TELESEISMIC SHORT PERIOD SEISMOGRAM

4.1 INTRODUCTION

Observations of the seismic waves generated by underground nuclear explosions have led many investigators to conclude that the explosion is often accompanied by some type of induced tectonic stress release. An excellent summary of the background leading to this conclusion may be found in Aki and Tsai [1972]. There are, in essence, two explanations of the predominant mechanism by which the stress is released. The first, advanced by Archambeau and coworkers (Press and Archambeau [1962], Archambeau [1964, 1968, 1972], Smith, et al. [1969], Lambert, et al. [1972], Archambeau and Sammis [1970]), assumes that the mechanism is stress relaxation around the predominantly spherical fracture zone created by the explosion. The second model is that of the release of stress along a pre-existing fault plane. Evidence for the latter model is summarized by Aki and Tsai [1972] where it is referred to as the "trigger model". In either case, the center of dilatation explosion source is modified by the superposition of a double-couple source which is either superimposed on the explosion (Archambeau's model) or somewhat removed in space and time.

The association of tectonic stress release with explosions is important for a number of reasons. Failure to account for its influence can lead to bias in explosion yield estimates from body and surface wave measurements. Under certain circumstances it is conceivable that tectonic release could cause a failure to contain the radioactive gases emitted by the explosion. Further, an accurate estimate of the source generated elastic wavelet is of great value for determining the modulation of this pulse by its travel through the earth and, therefore, attempts to invert seismic data to uncover the structure of the earth.

Interest in tectonic release has been primarily directed to an explanation of the commonly observed SH and Love waves excited by explosions. As far as surface waves are concerned, the two suggested mechanisms for tectonic stress release are quite similar and both have been found to be consistent with observations.

The possible effect of tectonic release on the body wave signature of explosions is also of interest. Of particular significance is the amplitude from which body wave magnitude (m_b) is determined. It is our intention here to identify the situations in which tectonic release can have an important effect on the short period recording.

Archambeau's theory has been cast in a form suitable for computation with the controlling parameters being related to the properties of the rock at the hypocenter and the magnitude and orientation of the prestress field. The computational results are given in the form of the double-couple or quadrupole terms in the multipolar expansion of the displacement field. These can be added to the explosion generated monopole to obtain a complete source representation. Theoretical seismograms can then be computed.

Varying the parameters in Archambeau's model, we can discover the values which must obtain in order for tectonic release to have an effect on the body wave recording. Applying other evidence, one can then identify those situations in which these parameters may be reasonable or likely.

The double-couple for the triggering of dislocation along a nearby fault plane is mainly different (for teleseismic body waves) from Archambeau's in that this source is separated from the explosion hypocenter. This quadrupole source spectrum would be expected to depend on stress drop and fault (weak zone) dimensions in an analogous way. While the computations to be shown are for Archambeau's model, an

extrapolation to the alternative mechanism is straightforward. The analysis presented is therefore relevant to the general question of the effect of tectonic release on the short period P wave record.

4.2 ARCHAMBEAU'S TECTONIC RELEASE MODEL

Before proceeding, a brief discussion of Archambeau's model and the important parameters controlling the size of the tectonic release component of the radiation field is in order. The physical mechanism on which Archambeau's theory is based is summarized in Fig. 4.1 (from Archambeau [1972]). The zone of radius R_c is made up of pulverized material and is assumed to be created at a rate denoted V_{R_1}. The radially cracked zone of radius R_0 is assumed to be created at a rate V_{R_2}. The zone from which the tectonic prestress is released is of radius R_s. A pure shear prestress field of amplitude $\sigma^{(0)}$ is applied.

Due to the filtering properties of the earth and the short period instrumentation, teleseismic body wave observations generally include only a narrow sampling of the source spectrum, between about 0.5 and 2.0 Hz. The important parameters for the tectonic release are then $\sigma^{(0)}$ and R_0 as the amplitude of the spectrum is directly proportional to $\sigma^{(0)}$* and R_0^3. Note that since the shatter zone volume should be proportional to yield and to R_0^3, the tectonic release amplitude is directly proportional to yield. The corner frequency depends on V_{R_2} and R_0 but is generally sufficiently high to be of little importance. Archambeau's assumption of a finite R_s, which is interpreted as representing a nonuniform prestress field, has led to considerable

*The proportionality is more fundamentally to the strain which equals the quotient of the stress and the material rigidity.

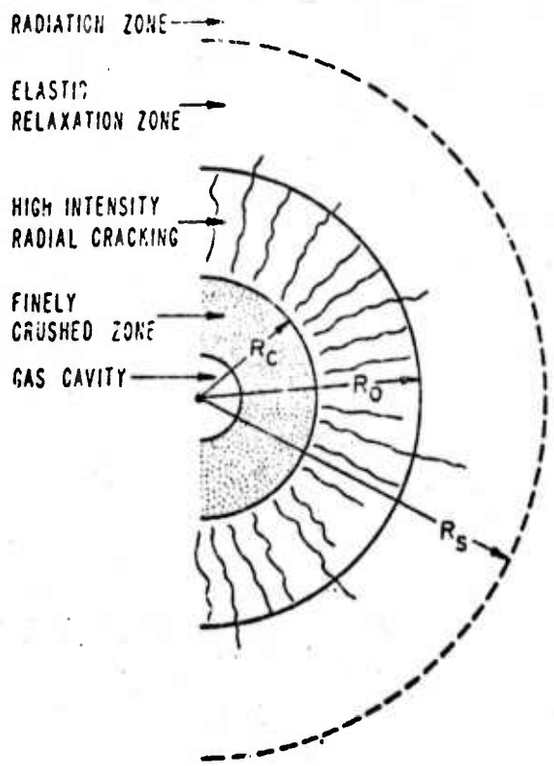

Figure 4.1. Schematic representation of the radial zone of material around a large explosion in a prestressed medium. R_c and R_o are radii enclosing zones of failure and vary with explosive yield, prestress and medium type while R_s is the radius within which most of the relaxation effects occur (from Archambeau [1972]).

controversy (see, for example, Snoke [1975]) since the resulting source spectrum is peaked. While the assumed value of R_s is of paramount importance for SH and Love wave studies it turns out to be of little consequence to the study undertaken here.

In subsequent sections we will first describe the character of the source radiation for an explosion plus tectonic release. Synthetic seismograms will then be computed and studied to determine the effect of the tectonic release.

4.3 EXPLOSION MODELING

Our objective is to determine the effect of the addition of a tectonic release generated quadrupole component to the monopole explosion. The amplitude of the elastic waves generated by the explosion itself is then obviously of critical importance. This portion of the source is discussed in this section.

The equivalent elastic source for the spherically symmetric explosion is conveniently discussed in terms of the reduced displacement potential which, in the frequency domain, is related to the monopole by

$$A_{\infty}^{(4)}(\omega) = -k_p^2 \frac{\hat{\dot{\Psi}}(\omega)}{V_p} \quad . \tag{4.1}$$

It should be pointed out that the far field component of the displacement spectrum (in a homogeneous whole space) is related to the reduced displacement potential by

$$\hat{u}_r(R,\omega) = \frac{\hat{\dot{\Psi}}(\omega)}{RV_p} e^{-ik_pR} \quad . \tag{4.2}$$

Deterministic computational methods for determining the reduced displacement potential for underground nuclear explosions have been developed by J. T. Cherry and his colleagues (Cherry, et al. [1973, 1974a], Bache, et al. [1975b]). These computations employ finite difference methods and require estimates of the constitutive behavior of the rock over the range of stresses encountered. The material behavior accounted for includes that attributable to water content, air-filled porosity, brittle failure and plastic flow. Computed source representations for various rock types encountered at NTS have been shown to be consistent with both near-source and teleseismic body wave data (Bache, et al. [1975b]).

In Fig. 4.2 is shown the amplitude of $\hat{\dot{\Psi}}(\omega)$ for two calculations, both representing NTS tuff. The second was computed specifically for a class of explosions in saturated tuff at Yucca Flat, NTS. The peaking in the source spectrum for the latter is primarily due to the form of the effective stress law in the constitutive model (see Bache, et al. [1975b] for details).

The source spectra of Fig. 4.2 shall be used to represent the explosion in the calculations to follow. The range of $|\hat{\dot{\Psi}}(\omega)|$ expected to be encountered at NTS is indicated in Fig. 4.3 which is taken from Bache, et al. [1975a]. Note that in the teleseismic frequency band, Source A is considerably smaller in amplitude than Source B.

Since the calculations leading to the source spectra of Fig. 4.3 were consistent with the available near field data as well as teleseismic body wave observations, they should provide useful guidance in selecting the important parameter, R_0, for the tectonic release. In particular, the greatest radius at which material yielding occurred was monitored. This

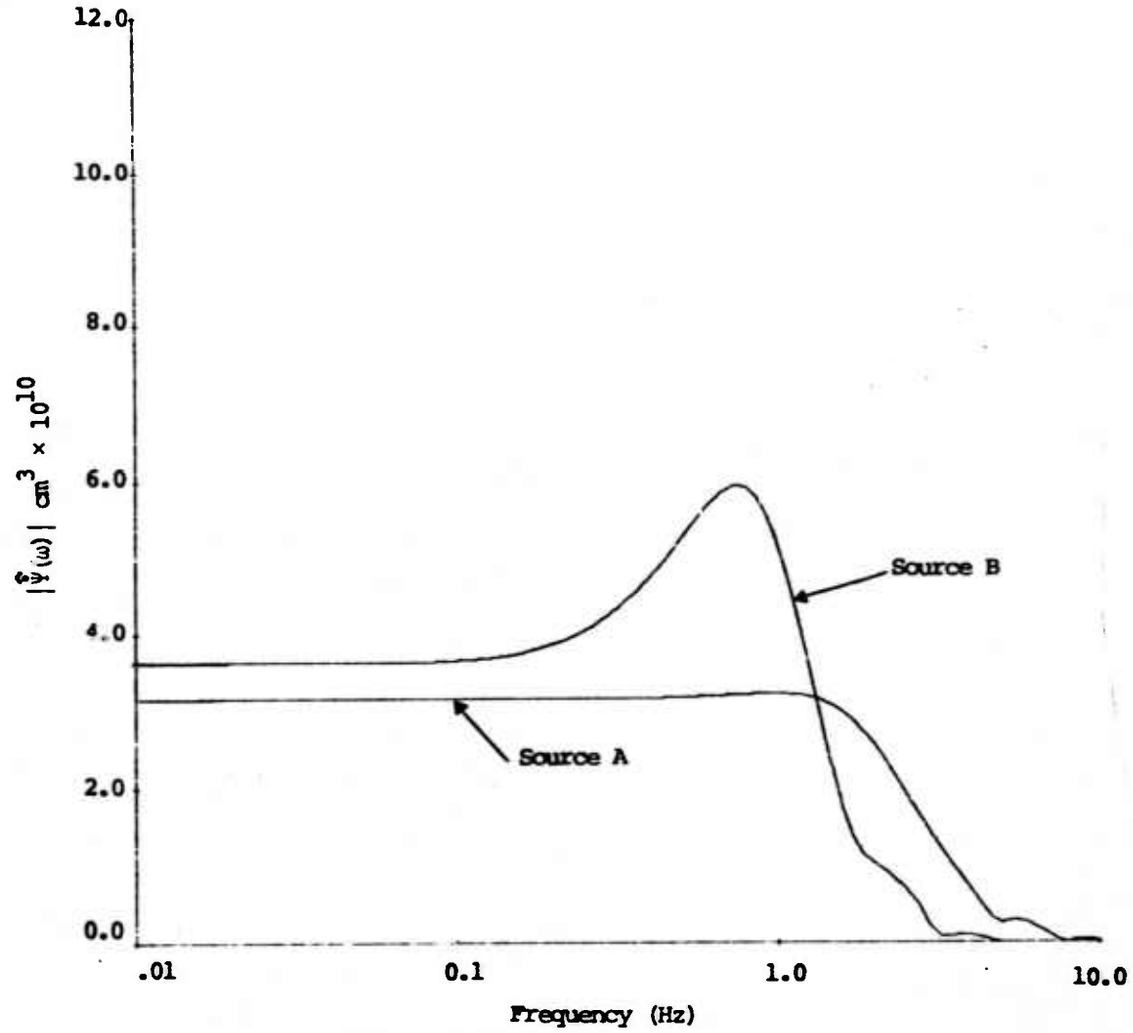

Figure 4.2. The source spectra, $|\hat{\Psi}(\omega)|$, for two calculations in NTS tuff. The explosion yield is 150 kt. For different yields the spectra scale, the amplitude directly with yield and the frequency inversely with the cube root of the yield.

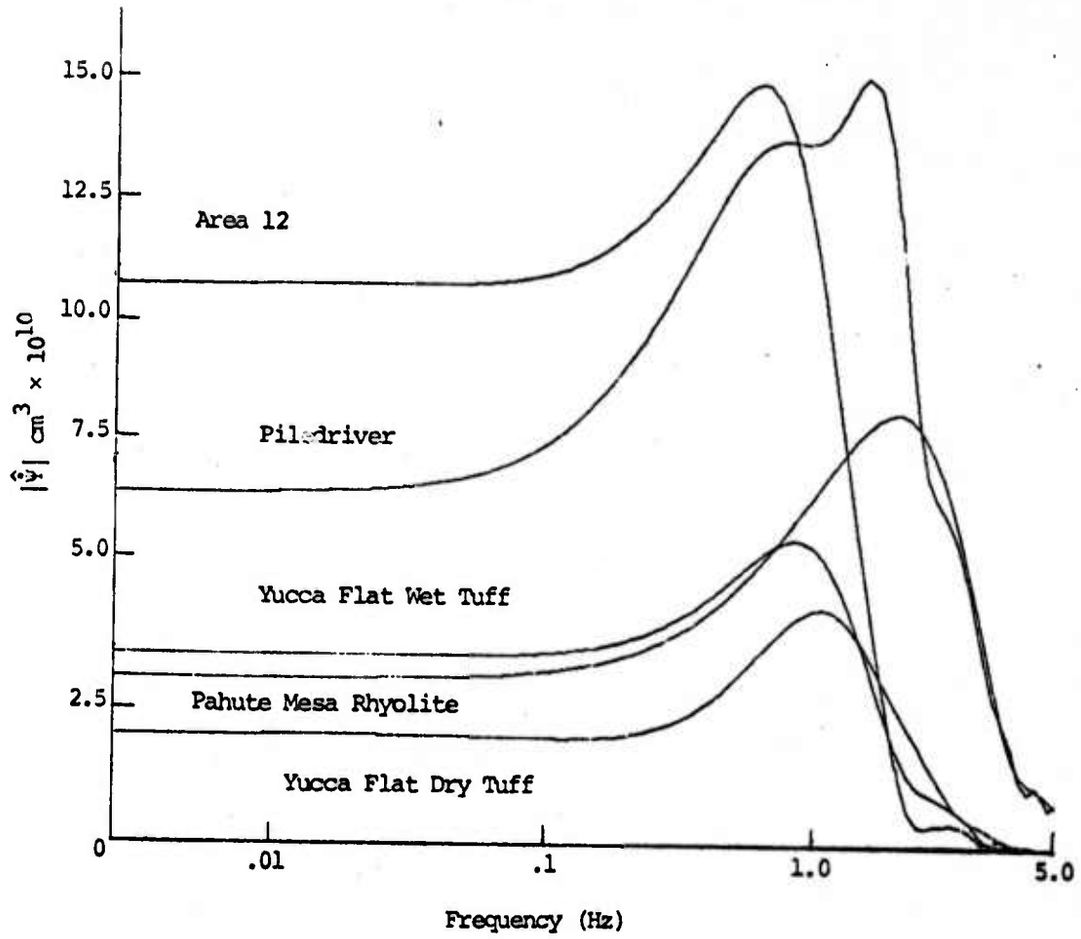

Figure 4.3. Source spectra, $|\hat{\Psi}(\omega)|$, for a variety of NTS materials. For these plots the yield is 150 kt. The source denoted Yucca Flat Wet Tuff is Source B of Fig. 4.2.

number, denoted R_e, should provide an upper limit to R_0. The computed values of R_e are summarized in Table 4.1.

TABLE 4.1. COMPUTED MAXIMUM RADIUS AT WHICH YIELDING OCCURS FOR 150 KT

Source	Radius (meters)
A	490
B (Yucca Flat Wet Tuff)	670
Yucca Flat Dry Tuff	310
Area 12	850
Pahute Mesa Rhyolite	360

4.4 THE EQUIVALENT ELASTIC SOURCE

A compatible tectonic release quadrupole component is now added to the explosion monopole and the resulting elastic field is examined. The specific example chosen is a 150 kt explosion in tuff. The important features of the four source representations to be studied are summarized in Table 4.2.

Tuff is, of course, a common material for underground tests at NTS. The yield of 150 kt is typical of many such tests. While we will be dealing with this specific case, the results will be representative of a wide range of tests and near source materials, as will be pointed out in the ensuing discussion.

The selection of parameters for the tectonic release calculations was based on the following considerations. The measured cavity radius for 150 kt shots in tuff is on the order of 60 meters. Recalling that the model is rather insensitive to R_c, a value of 60 meters was then used in all calculations. As mentioned in the previous section, an

TABLE 4.2. SUMMARY OF SOURCE CALCULATIONS (150 KT EXPLOSION IN TUFF)

Source	Explosion Model*	Elastic Velocities**	Shear Modulus (kbar)	Rupture Velocities	R_c	R_0	R_s	$\sigma(0)$ (bars)
1	A	$V_p = 2.4$ $V_s = 1.3$	31.4	$V_R = 2.45$ $V_{R_2}^1 = 1.2$	0.06	0.5	5.0	60
2	A	$V_p = 2.4$ $V_s = 1.3$	31.4	$V_R = 2.45$ $V_{R_2}^1 = 1.2$	0.06	0.3	∞	60
3	A	$V_p = 2.4$ $V_s = 1.3$	31.4	$V_R = 2.45$ $V_{R_2}^1 = 1.2$	0.06	0.3	5.0	60
4	B	$V_p = 2.5$ $V_s = 1.56$	45.0	$V_R = 2.55$ $V_{R_2}^1 = 1.4$	0.06	0.5	5.0	90

* The source model designations refer to Fig. 4.2.

** All lengths are in kilometers.

estimate of R_0 is given by the computed outer radius at which yielding occurs. Since the tectonic release scales with R_0, we shall be interested in a range of values and particularly the minimum R_0 required for tectonic release to affect the body wave. The same is true for the prestress which is initially chosen to correspond to a strain of $\approx 10^{-3}$, a value not unreasonable for NTS materials. Note that the tectonic release component for Sources 1 and 4 is essentially identical since it is prestrain which is the determining parameter.

The elastic radiation field generated by the four sources of Table 4.2 will now be studied by examining far field spectra and radiation patterns. The far field component of the radiation pattern is that which decays as R^{-1}. The coordinate system to be used is depicted in Fig. 4.4.

First, consider the case of a pure strike-slip tectonic release. That is, let $\sigma_{xy} = \sigma^{(0)}$. Spectra for Sources 1, 2, and 3 at azimuth $\phi = 45°$ and two takeoff angles, $\tau = 15°$, $45°$, are shown in Fig. 4.5. The radiation field is composed of P, SV and SH components (the outgoing S wave is polarized with respect to the free surface). For Source 1 the 1.0 Hz spectral component radiation patterns are plotted in Fig. 4.6 at azimuth 45° and takeoff angle 15°. The azimuth 45° is a maximum on the SV radiation pattern and a node for SH waves. Since we will not be concerned with SH and Love waves, the SH component will not be shown. Finally, in Fig. 4.7 the 1.0 Hz radiation patterns for Source 2 are shown.

For teleseismic body waves the important energy leaving the source is at takeoff angles $\approx$ 5°-20° for the direct P wave and $\approx$ 160°-175° for the free surface reflected pP and sP phases. For a takeoff angle of 15°, the ray parameter $p \approx 0.11$ sec/km and the free surface reflection coefficients are approximately -0.92 and 0.16 for pP and sP, respectively (Cerveny and Ravindra (1971), Section 2.4).

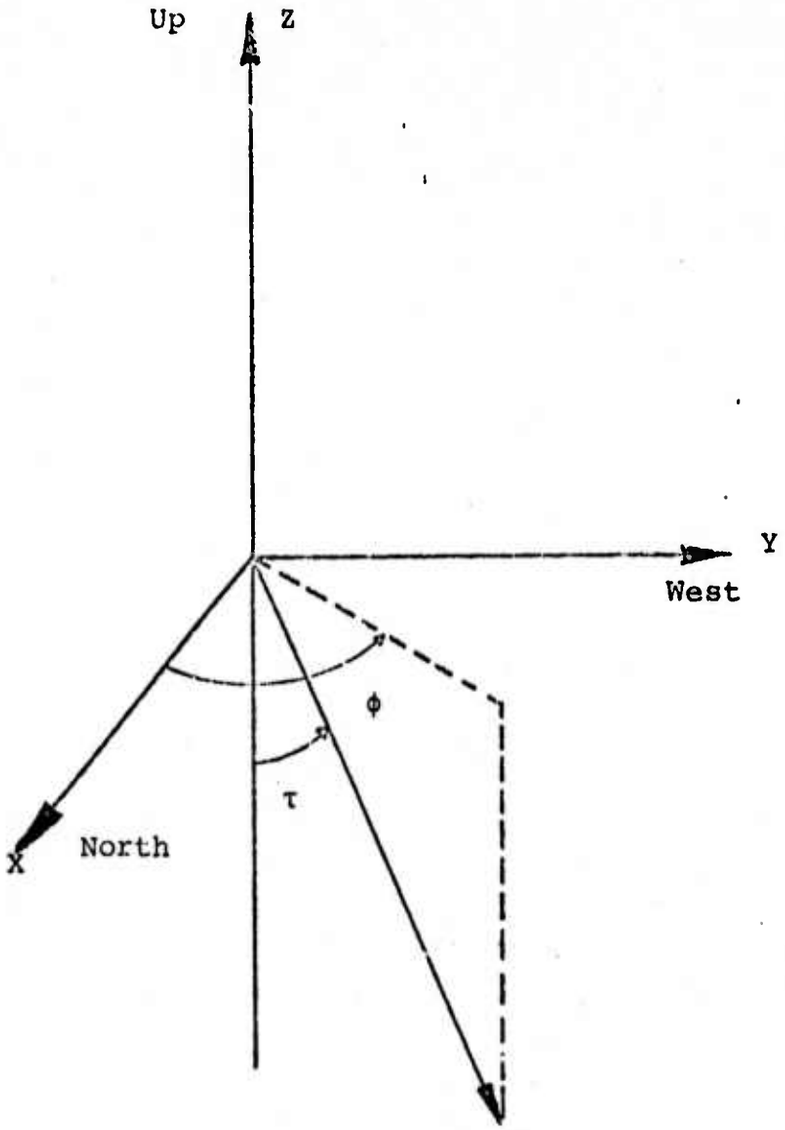

Figure 4.4. The geographic coordinate system, fixed with respect to the earth.

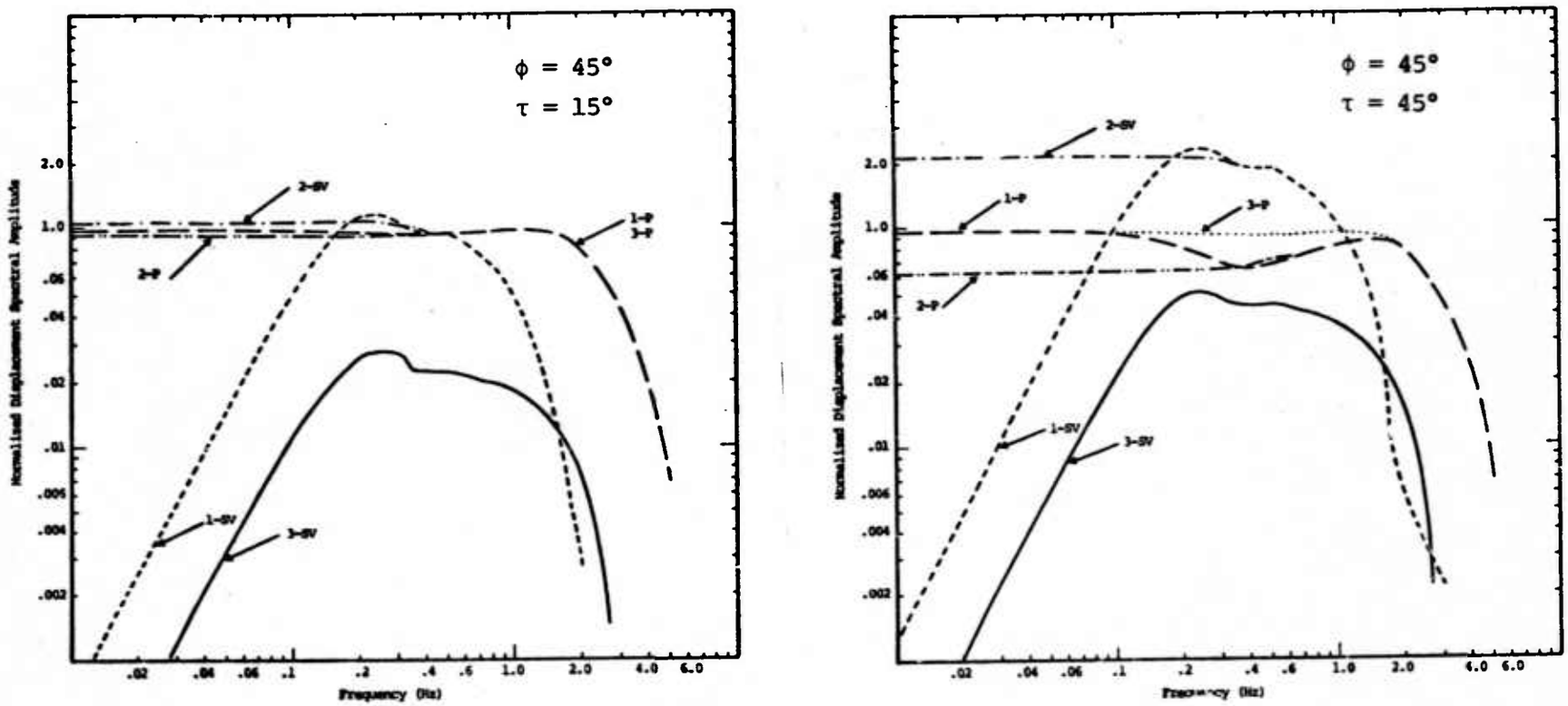

Figure 4.5. Normalized displacement spectra at azimuth $\phi = 45°$ and two takeoff angles for the sources designated 1, 2, 3 in Table 2. The P and SV components are plotted and all values are normalized to the 1 Hz displacement (at the same radius) due to the explosion alone.

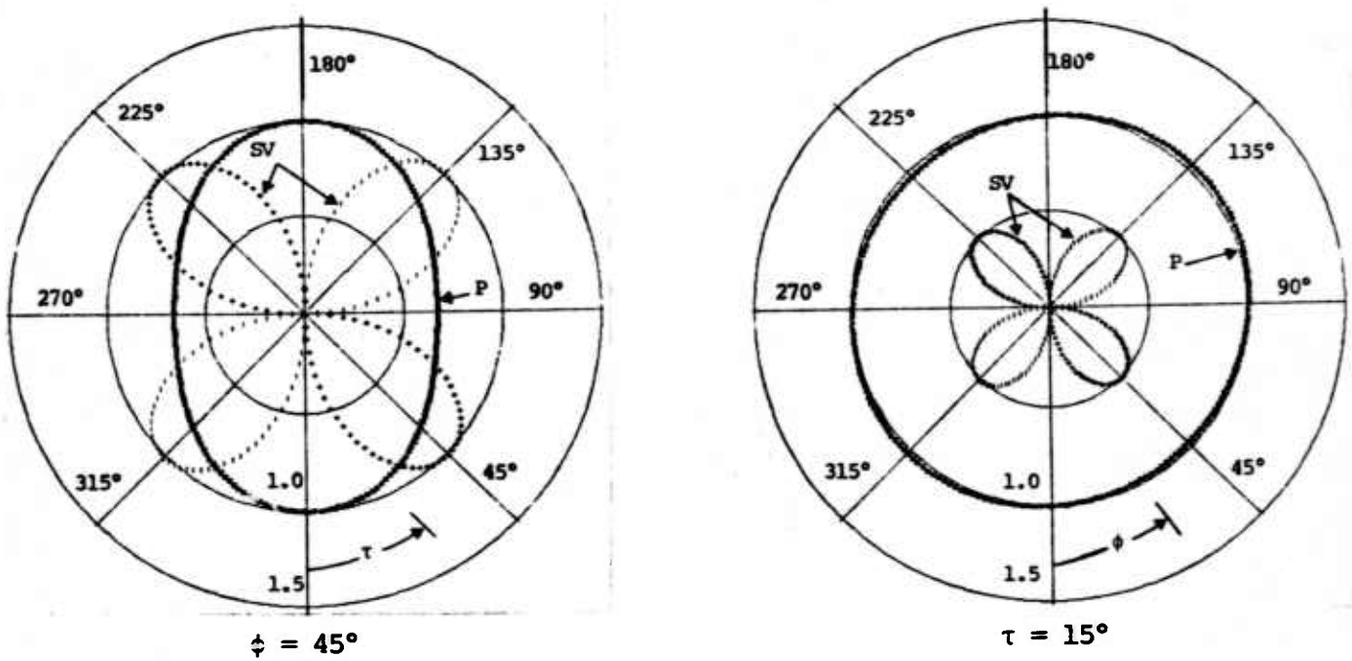

Figure 4.6. Normalized radiation patterns for the 1.0 Hz spectral component for Source 1. The normalization is as in Fig. 4.5. Thus the effect of tectonic release is represented by the presence of SV waves and the deviation of the P wave pattern from the unit circle.

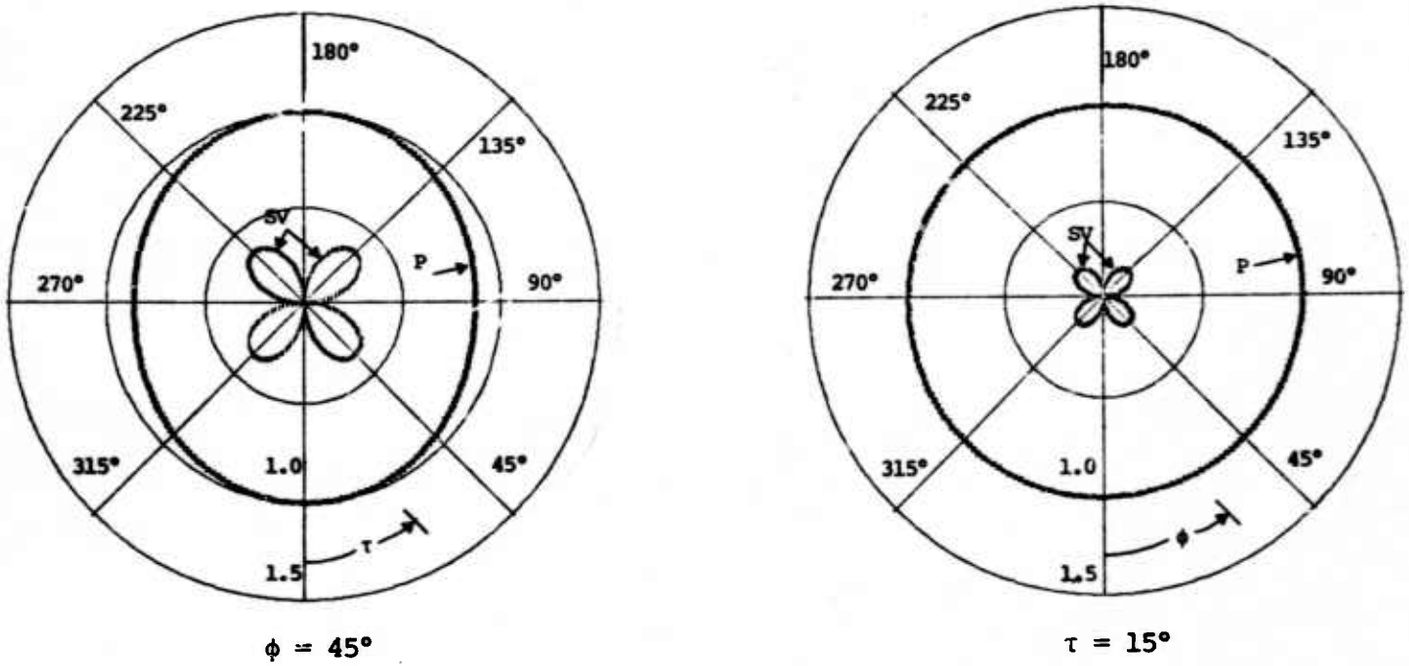

Figure 4.7. Normalized radiation patterns for the 1.0 Hz spectral component for Source 2. The normalization is as in the previous figure.

Concerning Figs. 4.5-4.7, the following observations are made:

- For the spectra shown, the SV wave is about the same size as the P wave in the band $0.5 < f < 2.0$ Hz. It must be much larger for sP to strongly affect the body wave record.
- At the relevant takeoff angles, the P wave is little affected by tectonic release.
- The portion of the spectrum which is affected by R_s is outside the band of interest for body waves. However, R_s is clearly important for long period waves.
- The effect of R_0 is primarily to scale the spectrum with R_0^3. The spectrum is also shifted to lower frequencies with increasing R_0, but this effect is minor for the range of appropriate values.
- The strike-slip orientation is rather unfavorable for observing tectonic release in teleseismic body waves. Other orientations of the prestress field are considerably more favorable.

The tectonic release controlling parameters R_0 and $\sigma^{(0)}$ used above are large but seem not unreasonable for NTS tuff explosions. We should also attempt to define a source which includes the greatest values that can be justified for this model. Therefore, let us multiply the tectonic release component in Source 1 by four. Since the amplitude is essentially directly proportional to $\sigma^{(0)}$ and R_0^3, this is equivalent to taking $\sigma^{(0)} = 240$ bars, $R_0 = 0.5$ km or $\sigma^{(0)} = 60$ bars, $R_0 = 0.79$ km or various other combinations giving $\sigma^{(0)} R_0^3 \approx 30$. The Source 1 spectrum at $\phi = 45°$, $\tau = 15°$, is compared to that for the same source with the

tectonic release multiplied by four in Fig. 4.8. Parenthetically it should be noted that it is difficult, but not impossible, to justify using values of $\sigma^{(0)} R_0^3 > 30$ in the calculations. On the other hand, one might argue that $\sigma^{(0)} R_0^3$ must be less than 1. The physics is rather poorly understood and remains a subject for conjecture. Studies of the effect of tectonic release provide the best hope for fixing these parameters.

4.5 COMPUTATION OF THEORETICAL SEISMOGRAMS

Having developed some understanding of the source displacement spectra, we now shift attention to the computation of theoretical seismograms to see directly the effect of tectonic release. The computations are based on the representation of an equivalent elastic source buried in a stack of plane elastic layers, which was developed in Appendix B, Bache, et al. [1975a]. Input to the representation includes the crustal structure, depth of burial, the multipolar coefficients defining the source and the ray parameter of interest for the teleseismic wave. The output is the displacement spectrum along the specified ray.

We are interested in isolating the source, which is taken to be the explosion plus tectonic release, and its modulation by the near source geology. Therefore, while we need realistic seismograms, modification by the upper mantle and receiver region crustal reverberations are minimized in the computations. The following elements are included:

- A constant, G_s, is used to represent the geometric spreading in the upper mantle. This constant is computed using the method of Julian and Anderson [1968] and is dependent on the upper mantle velocity model and epicentral distance chosen. The earth model CIT109

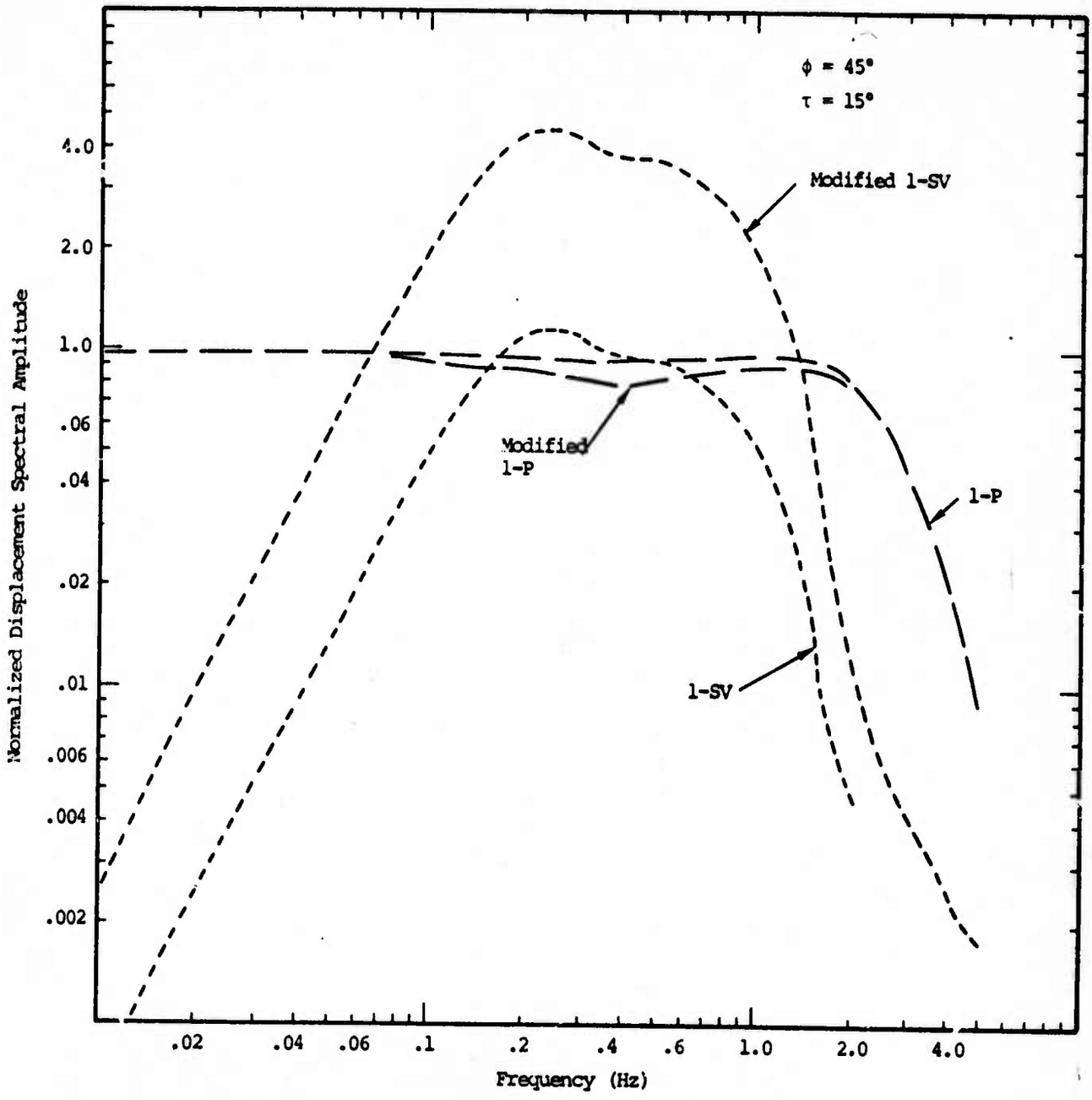

Figure 4.8. Normalized displacement spectra at $\phi = 45°$, $\tau = 15°$ for Source 1 compared to the spectra for the same source with the tectonic release component quadrupled.

(Archambeau, Flynn and Lambert [1969]) was used and the epicentral distance was fixed at 4000 km. Then, for all synthetic seismograms $G_s = 0.45 \times 10^{-4}$ and ray parameter p = 0.079 sec/km.

- Anelastic attenuation and the attendent dispersion are included by multiplying the displacement spectrum by

$$\exp\left\{-\pi f \frac{T}{Q}\left[1 - \frac{2}{\pi} i \ln\left(\frac{1000}{f}\right)\right]\right\},$$

following the suggestion of Strick [1970]. Here f is frequency and the controlling parameter T/Q is the ratio of travel time (T) to the average path material quality factor (Q). For all computations T/Q = 0.9.

- Crustal reverberations at the receiver are computed using the Thompson-Haskell method (e.g., Haskell [1962]). A crustal model having no very strong amplitude effects was chosen for all computations. The model is shown in Fig. 4.9.

- The transfer function for a standard short period instrument, the LRSM Benioff, was applied.

As the illustrative example, we have chosen a 150 kt explosion in NTS tuff. For all calculations the depth of burial was taken to be 0.8 km, a value typical of explosions in this yield range. Two crustal models were used for the source region and these are shown in Fig. 4.9. The first model (SS1) has a very strong impedance contrast between the tuff and underlying hard rock. A tuff-paleozoic rock contrast of this kind is found at Yucca Flat. The second model (SS2) has this contrast spread over a wavelength or so (at $\approx$ 1 Hz).

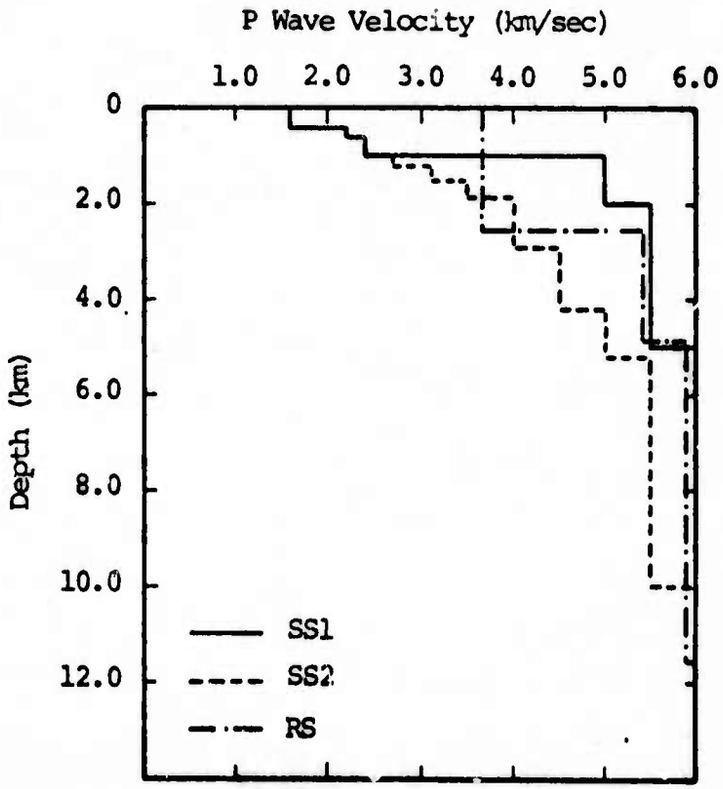

Figure 4.9. Compressional wave velocity versus depth for three crustal models used in the computations: the source region models SS1 and SS2 and the receiver region model RS.

Synthetic seismograms for the explosion alone (no tectonic release) are shown in Fig. 4.10. As an indication that these theoretical records are representative of reality, several Palmer Network observations of the Starwort event are also shown in the figure. Starwort was an 85 kt shot, buried at 0.564 km in tuff at Yucca Flat. Taking account of the shallower burial depth, we see that the frequency content and shape of the first few swings on the records are comparable.

In Figs. 4.11 and 4.12 are shown the effect of including the strike-slip tectonic release component discussed in the previous section. The tectonic release model is that designated No. 1 in Table 4.2 and the same model with the tectonic release component multiplied by two and by four. The latter is taken to represent the maximum credible amount of tectonic release for the physical model considered. Computations were made with both the crustal models SS1 and SS2. In view of the radiation patterns (Fig. 4.5), only the azimuths 45° and 135° were considered since the tectonic release influence is maximized at these azimuths.

It is immediately clear from Figs. 4.11 and 4.12 that a pure strike-slip tectonic release has insignificant influence on teleseismic body waves. Even for the maximum amount (A = 4) at the optimal azimuths, the effect is hardly noticeable, especially in view of the variation between observations at nearby stations seen in Fig. 4.10.

4.6 TECTONIC RELEASE FROM AN OPTIMALLY ORIENTED PRESTRESS FIELD

It is natural to inquire, what is the effect of tectonic release that is oriented to maximize the effect on teleseismic short period observations? Such an orientation results from a pure shear prestress field that dips at 45°.

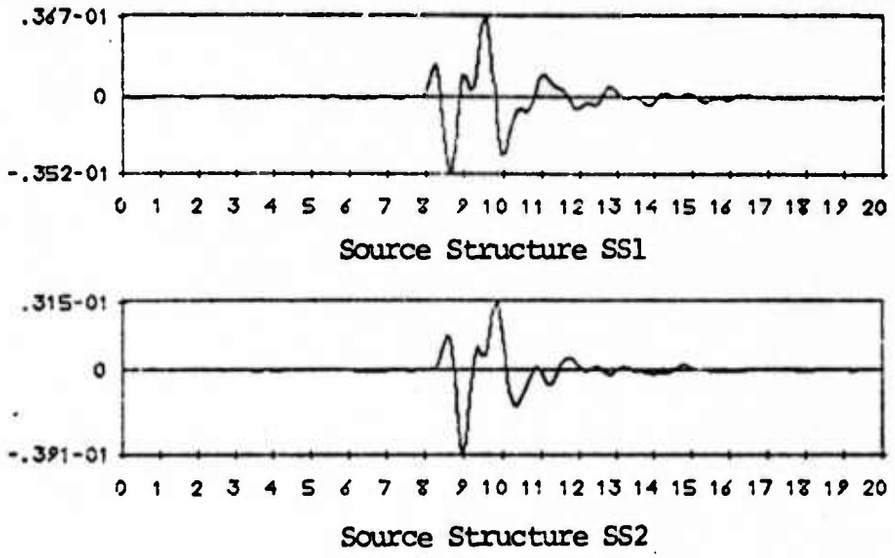

(a) Synthetic seismograms for two near source crustal structures. Amplitude in microns at 1 Hz is indicated.

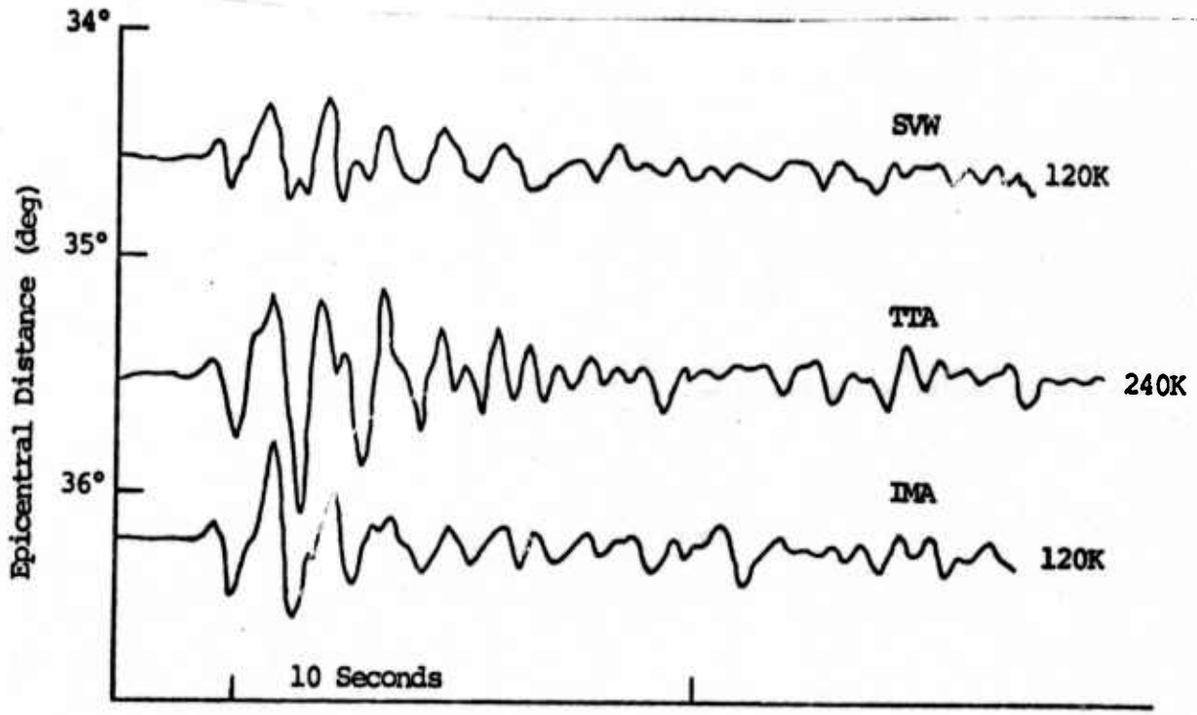

(b) Observed seismograms from the Palmer Network in Alaska for the Yucca Flat event Starwort. The station codes are indicated as is the magnification at 1 Hz.

Figure 4.10. Synthetic seismograms for the explosion alone (no tectonic release) and Palmer Network observations of an event similar to that modeled.

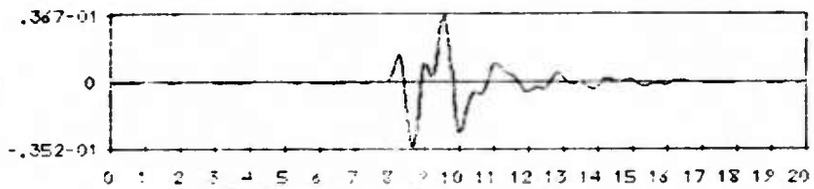

No Tectonic Release (A = 0)

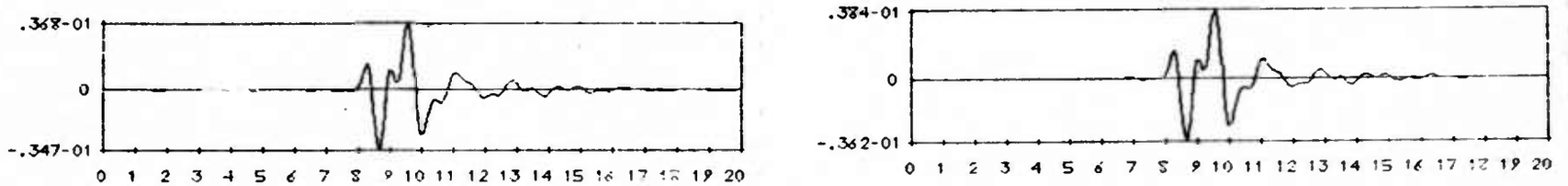

Tectonic Release, Source 1 of Table 1 (A = 1)

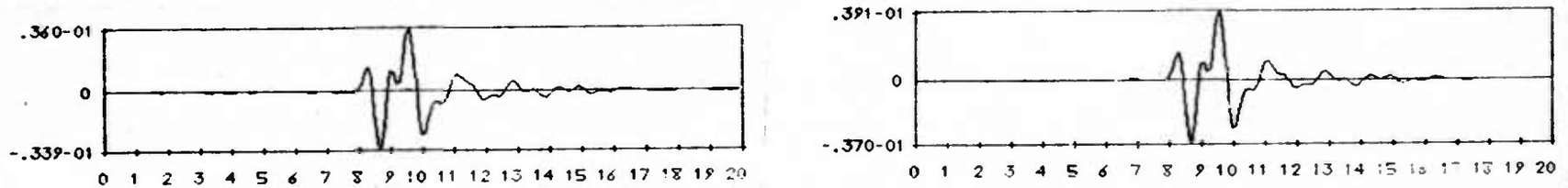

Tectonic Release Component Doubled (A = 2)

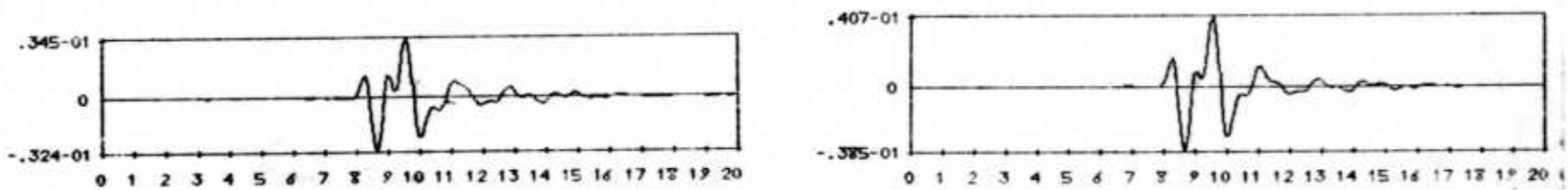

Tectonic Release Component Quadrupled (A = 4)

Azimuth 45° Azimuth 135°

Figure 4.11. Theoretical seismograms for Source 1 with the tectonic release component multiplied by the constant A. The burial depth was 0.8 km in the crustal structure SS1 of Fig. 4.9. The crustal model RS of Fig. 4.9 was used at the receiver and the upper mantle was characterized by the spreading factor $.45 \times 10^{-4}$ and T/Q = 0.9. The amplitude is indicated in microns at 1 Hz and the relative time is given in seconds.

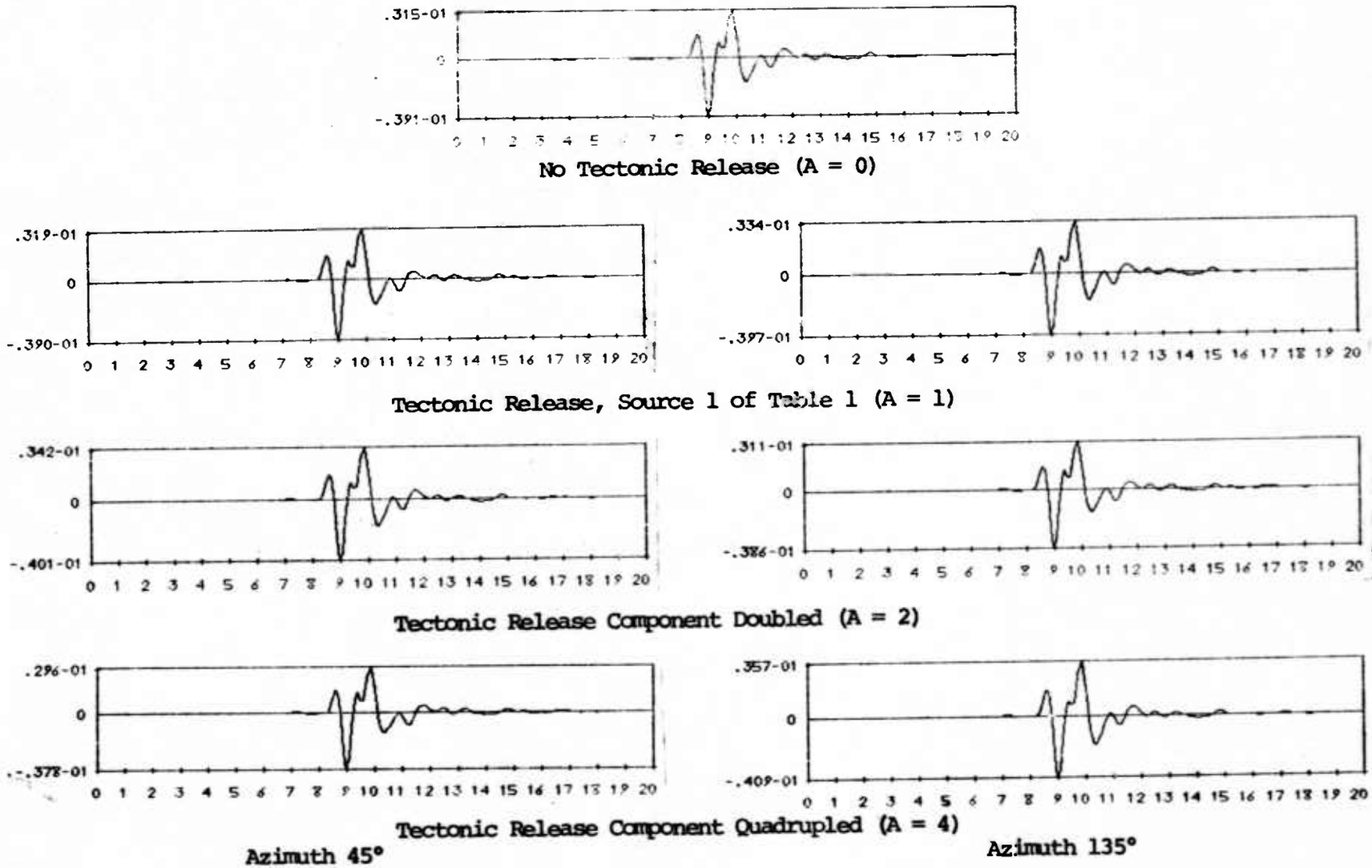

Figure 4.12. Theoretical seismograms identical to those of Fig. 4.11 except that the source region crustal model SS2 was used.

In the coordinate system of Fig. 4.4, one such field is given by $\sigma_{xz} = -\sigma_{xy} = \sigma^{(0)}/\sqrt{2}$. This corresponds to rotating the strike-slip sources of the previous section by 45° about the y-axis. Sample radiation patterns for the new source are shown in Fig. 4.13. For this source the optimal azimuths for tectonic release effects should be $\pm$ 30° from the x-axis.

Theoretical seismograms including tectonic release at the "optimal" orientation are shown in Figs. 4.14 and 4.15. Once again we have used Source 1 of Table 4.2 and the same source with the tectonic release component doubled and quadrupled. The following conclusions may be drawn:

- For the R_0 = 0.5 km, $\sigma^{(0)}$ = 60 bars source, the influence of tectonic release is rather insignificant, even at these optimal azimuths for the optimal orientation.
- For a doubled or quadrupled tectonic release, the effects become important. In particular, a strong variation with azimuth becomes apparent. The maximum amplitude from which m_b would be measured varies by as much as a factor of two, dependent on azimuth.

So far we have restricted attention to Sources 1-3 of Table 4.2 and thus the explosion model denoted A in Fig. 4.2. To be certain that our conclusions have not been unduly influenced by this choice, we now consider Source 4 of Table 4.2, which is quite similar to Source 1 except that the explosion model B is used. The relevant synthetic seismograms are shown in Fig. 4.16. For this example we only show the cases where the effect of tectonic release is maximized. We find that it is only at the optimum azimuths for the optimum orientation, that tectonic release has a noticeable effect. This is expected since the explosion induced elastic wave (see Fig. 4.2) is relatively larger than that for Source 1 while the tectonic release component remains the same.

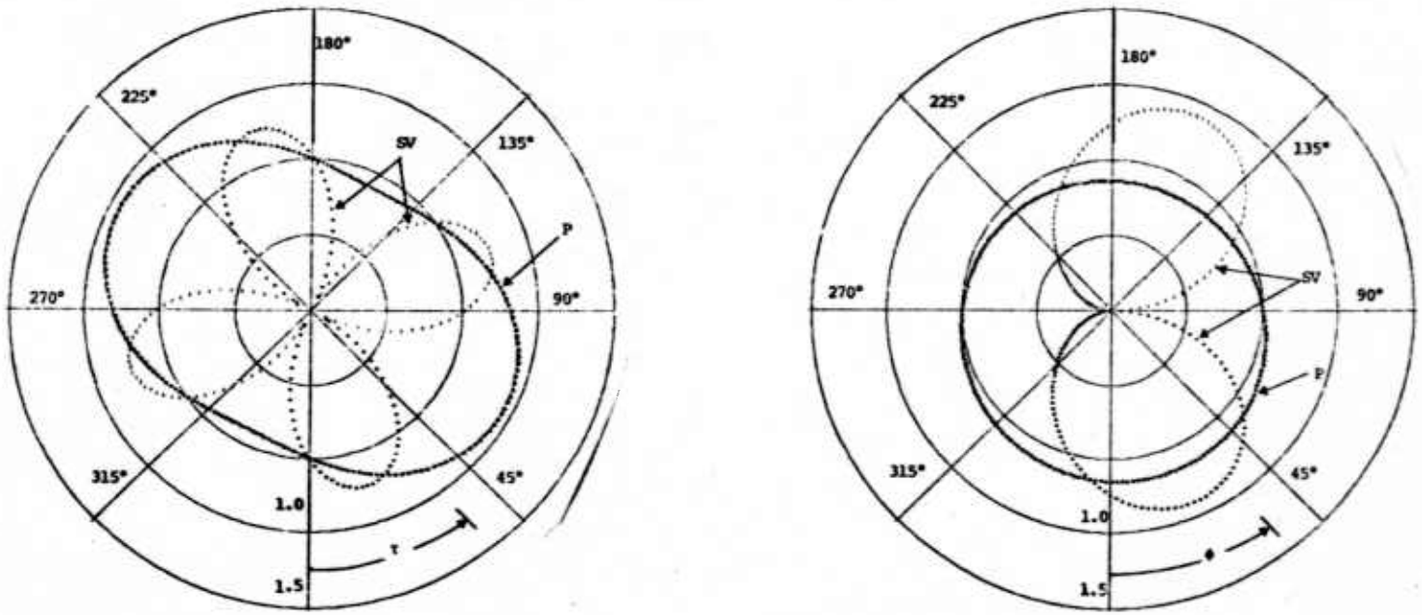

$\phi = 45°$ $\tau = 15°$

Figure 4.13. Normalized radiation patterns for the 1.0 Hz spectral component for Source 1 with the prestress field rotated 45° from the vertical (stress components are $\sigma_{xz} = -\sigma_{xy} = \sigma(0)/\sqrt{2}$). The normalization is as in Fig. 4.5.

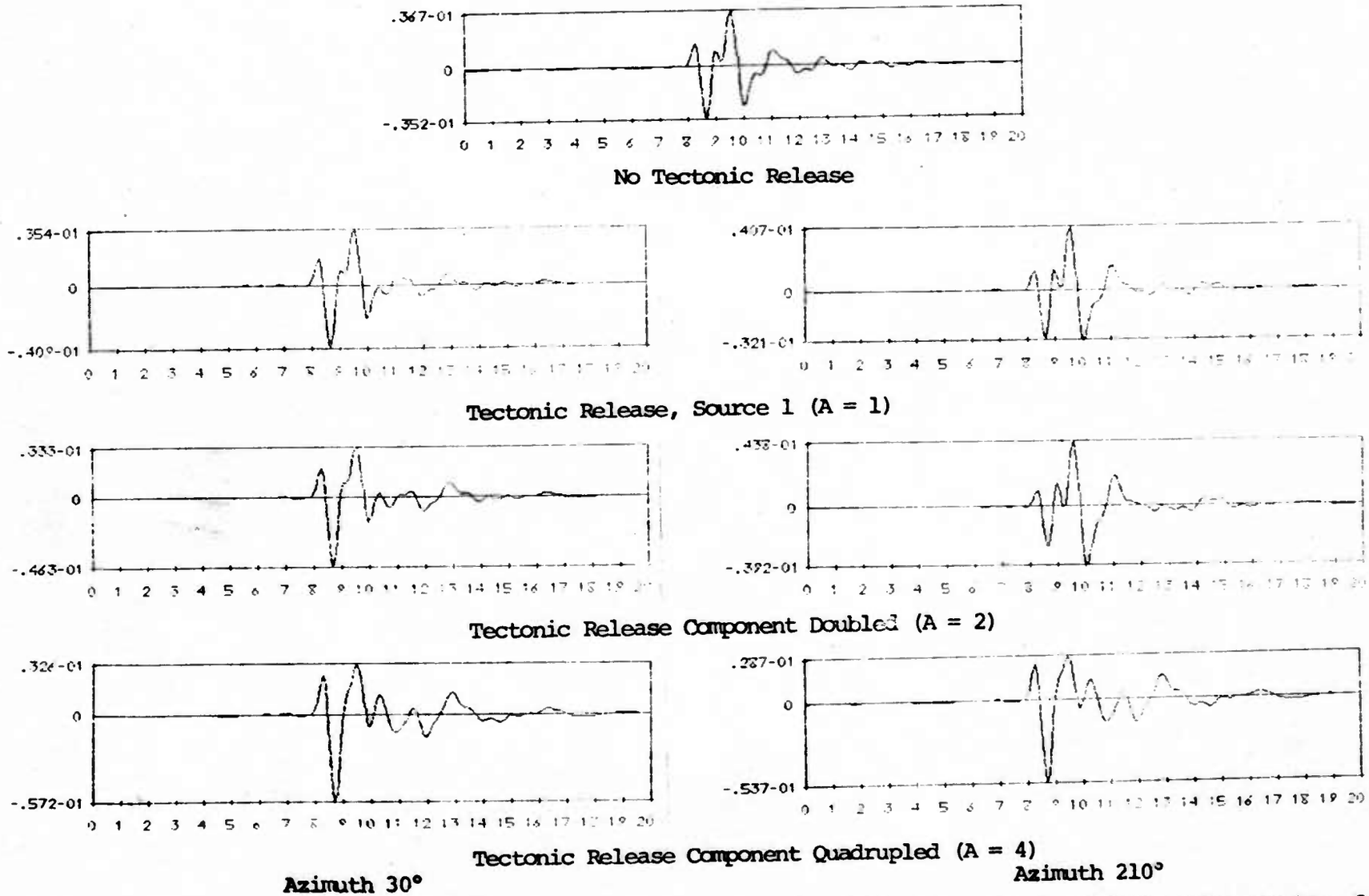

Figure 4.14. Theoretical seismograms for Source 1 rotated to the optimal orientation for body wave propagation. The tectonic release component is doubled and quadrupled and only those azimuths at which maximum effects are expected are shown. The propagation calculation was as for Fig. 4.11 with the crustal model SS1.

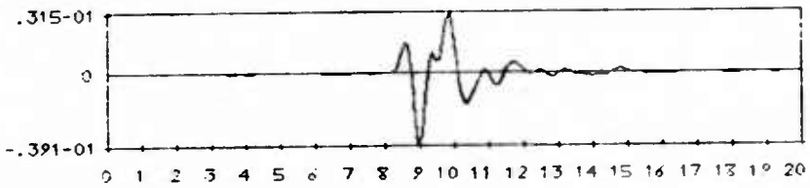

No Tectonic Release

Azimuth 30°

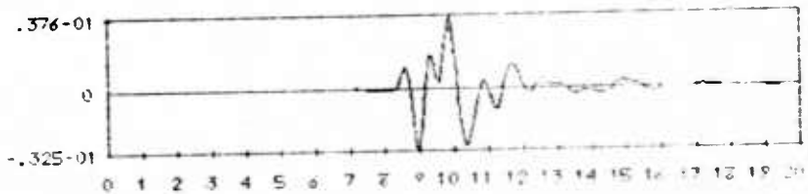

Azimuth 120°

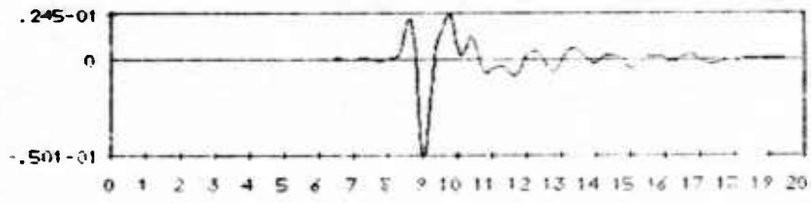

Azimuth 330°

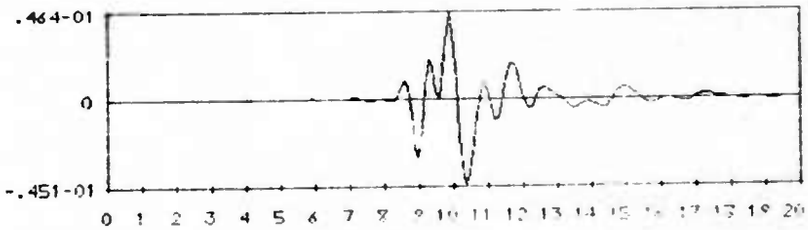

Azimuth 210°

Figure 4.15. Theoretical seismograms as for the last case of the previous figure (tectonic release component quadrupled) except that the source region crustal model SS2 was used.

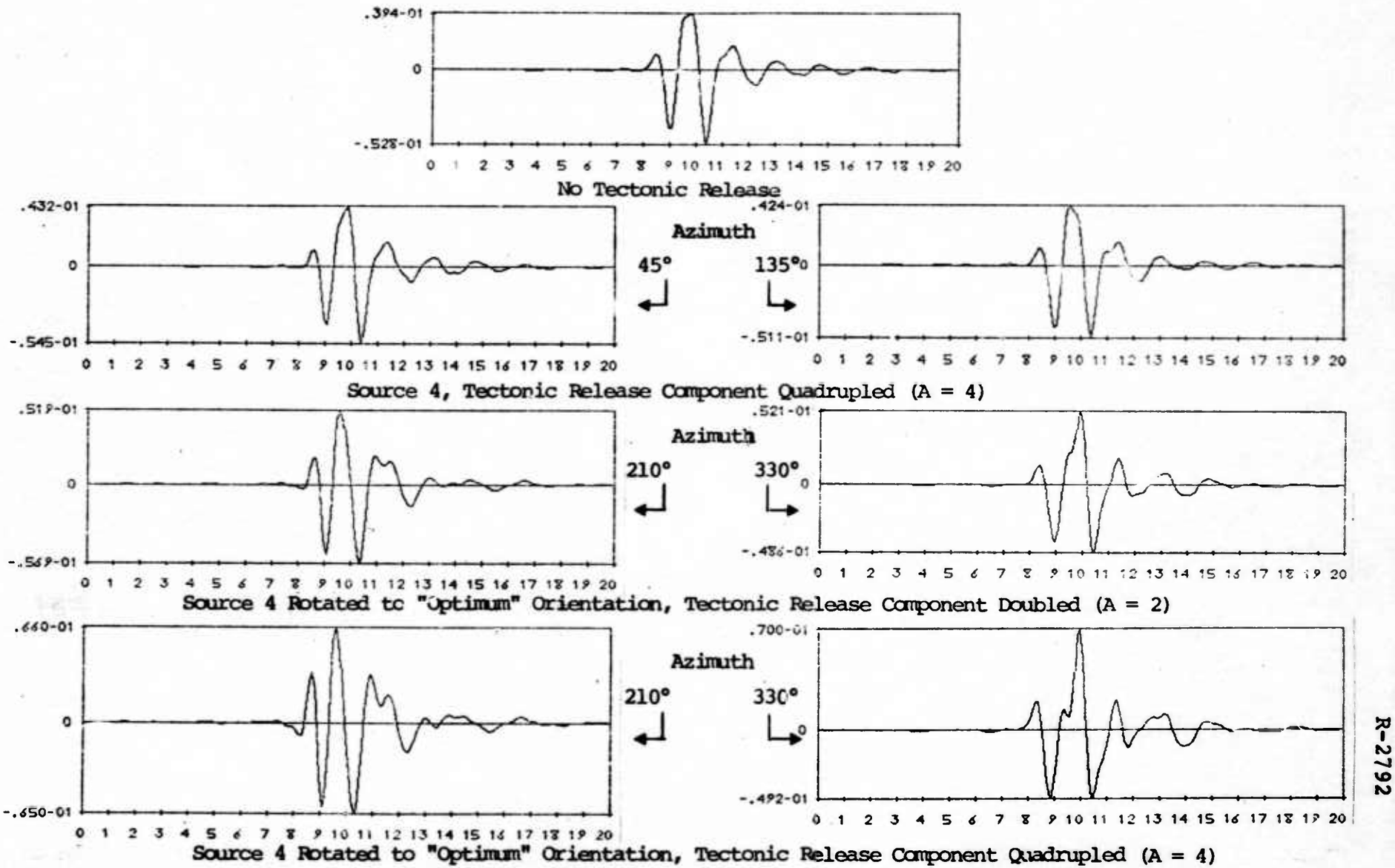

Figure 4.16. Theoretical seismograms for Source 4 with no tectonic release and with the "strike-slip" tectonic release component quadrupled. For the same prestress field rotated 45° from the vertical, seismograms are shown at the "optimum" azimuths for the tectonic release component doubled and quadrupled. The propagation path parameters are identical to those used for Fig. 4.11 and the crustal model SS1 was used.

4.7 SUMMARY AND CONCLUSIONS

This theoretical analysis represents an attempt to answer the question; under what circumstances can tectonic release have an important effect on the teleseismic body wave signature of explosions? Underlying the analysis are several fundamental assumptions: (1) The source is composed of a spherically symmetric radiator of elastic waves, the explosion, plus a double-couple representing tectonic release. (2) The computed reduced displacement potential representations of the explosion (Figs. 4.2 and 4.3) are reasonably accurate. (3) The earth models and computational techniques used for constructing the theoretical seismograms are sufficiently realistic to allow conclusions to be drawn about the contribution of the tectonic release component to the teleseismic record.

With the assumptions listed above, we have done the following:

- Since the important factor is the ratio of the explosion component of the displacement field to that due to tectonic release, the sample calculations were done for explosions which couple relatively weakly into elastic waves (Figs. 4.2 and 4.3).
- Using Archambeau's model of the tectonic stress release into the explosion created shatter zone, we chose what seemed to be the largest values that could be justified for the weak zone dimensions and prestress or prestrain.
- Two orientations of the prestress were invesgigated, one a pure strike-slip and the second rotated 45° about a horizontal axis. The latter is essentially optimal for propagating tectonic release generated body waves to teleseismic distances.

- For either orientation, theoretical seismograms were computed at azimuths where the tectonic release influence was strongest.

Let us first assume that the mechanism for the relaxation of tectonic release is that hypothesized by Archambeau. Then we can conclude that the body wave signature of explosions can only be affected if the prestress field is oriented near the optimum. That is, if the vertical component of the prestress is of the same order as the horizontal (e.g., $|\sigma_{xz}| \approx |\sigma_{xy}|$). Even for this orientation it is necessary that the tectonic release parameters be rather large. For the 150 kt example studied, we found that the product of the prestress, $\sigma^{(0)}$, and R_0^3, where R_0 is the radius of the shatter zone within which the material rigidity essentially vanishes ($\mu = 0$), must be $\approx$ 30 km-bar. For explosions characterized by a larger reduced displacement potential (e.g., those at Pahute Mesa), these parameters must be commensurately larger. For such cases tectonic release can significantly influence the shape of the displacement pulse characterizing the source and change the amplitude from which m_b is measured by a factor of two or so. These effects are, of course, strongly dependent on azimuth. Once again, it is only at optimal azimuths for the optimal orientation and the most favorable ratio of tectonic release to explosion generated elastic waves that the effect becomes important. Therefore, it seems reasonable to dismiss the tectonic release mechanism suggested by Archambeau as an important contributor to the body wave signature of explosions.

What if the tectonic release mechanism is the trigger model proposed by Aki and Tsai? First, we would expect the time lag between the explosion and tectonic release generated waves to be greater than studied here. Otherwise, the source characteristics important for teleseismic body waves should

be reasonably modeled by Archambeau's source theory. In fact, the double-couple term for the explosion induced tectonic release is essentially identical to the leading term in the multipolar expansion for the earthquake source theory developed by Archambeau and Minster (Archambeau [1964], Minster [1973]). Here R_0 is taken to be representative of half the fault length and $\sigma^{(0)}$ is the stress drop.

From the theoretical seismograms for the weak coupling 150 kt shot studied, we know that tectonic release has almost no effect on the short period P wave record when $\sigma^{(0)}R_0^3 \approx 7.5$, no matter what the orientation. For optimal orientations significant effects could be noticed when $\sigma^{(0)}R_0^3 \approx 30$. Aki and Tsai [1972] conclude that the tectonic release associated with large NTS explosions is a low stress drop ($\approx$ 10 bars) phenomenon. For $\sigma^{(0)}R_0^3 \approx 30$, we then would expect a significant contribution to the body waves for fault lengths on the order of 3 km. Aki and Tsai postulate fault lengths on the order of 4 km for the 235 kt shot Bilby and 10 km for Boxcar (1200 kt) and Benham (1100 kt, data from Springer and Kinnaman [1971]). Scaled to 150 kt and halved, these are equivalent to $R_0 \approx 1.7$ km for Bilby and ≈ 2.6 km for the two larger events. Then if the stress drop is 20-30 bars over faults of this order length, and if the fault displacement is neither strike-slip nor dip-slip but somewhere between and is associated with low coupling explosions, we would expect a significant contribution to the short period P wave record. Release of tectonic stress by this mechanism is therefore somewhat more likely to contribute to the short period record than by the mechanism proposed by Archambeau. Still, a coincidence of a number of favorable circumstances is required and this seems unlikely for most events.

With this analysis we are forced to conclude that for most, perhaps almost all, events it is safe to ignore tectonic release as a contributor to the short period P wave

recording. Still, a number of questions remain that can only be answered with further study. The choice between the trigger model and Archambeau's model of tectonic release may be resolved by a study of short period SH waves since depth of burial should be diagnostic. The amplitude of the tectonic release component could also be inferred from such a study.

The amplitude of the tectonic release component is best determined from surface wave observations. The work of Toksoz and Kehrer [1972] represents a good beginning. Recent developments in the computation of the explosion generated portion of the source (Bache, et al. [1975b]) should be quite helpful in further study.

Finally, it should be mentioned that source asymmetries, whether due to emplacement configuration or working point media inhomogeneities (e.g., jointing), can also cause the superposition of a double-couple on the source monopole (for example, see Cherry, et al. [1974]). The effect is virtually indistinguishable from that due to Archambeau's model of tectonic release. It may be that all three mechanisms for generating the double-couple are present to some degree with most explosions.

V. A THREE-DIMENSIONAL FINITE DIFFERENCE SIMULATION OF STICK-SLIP EARTHQUAKE FAULTING – THE EQUIVALENT ELASTIC SOURCE

5.1 INTRODUCTION

One of the important objectives of this contract is to uncover the nature of the earthquake source, especially those features that discriminate between earthquakes and underground explosions. With this objective in mind, a stick-slip rupture model has been incorporated into a three-dimensional Lagrangian finite difference code. The model has been exercised to compute the radiated energy due to a particular fault geometry. In this case the geometry was that of a bilateral rupture along a 1 km fault length.

A powerful technique for studying the elastic waves radiated from nonlinear source regions is first to replace the source with an equivalent elastic point source. The computational techniques of theoretical seismology can then be applied. The computation of the equivalent elastic source from finite difference source calculations was described in Appendix G of our last report under this contract (Bache, et al. [1975a]). The point source representation is unique and exact in the sense that everywhere outside the "elastic radius" at which the point source was obtained, the radiation from the equivalent point source is identical to that from the original nonlinear source.

In this section the three-dimensional finite difference earthquake (FDEQ) calculation is described with emphasis on the equivalent elastic source for this earthquake. Of particular interest is the description in Section 5.5 of the far field (propagating to teleseismic distances) displacement field radiated by the earthquake.

The important issue is what this finite difference earthquake simulation tells us about the nature of the earthquake source. To this end we are comparing the character of this source to data and to analytical models developed by others. A number of interesting results are being obtained and these will be discussed in forthcoming reports.

5.2 FAULT CONFIGURATION FOR THE THREE-DIMENSIONAL CALCULATION

A stick-slip rupture model has been incorporated into both two-dimensional (plane strain) and three-dimensional Lagrangian stress wave codes by Cherry and co-workers. Results of calculations of near-field earthquake ground motion from the plane strain version of the model were reported in Cherry [1973]. As reported by Cherry, et al. [1974b], this version of the model has been exercised to uncover the dependence of peak ground motion and response spectra on fault length, rupture velocity, and dynamic stress drop during rupture. Appendix A of Cherry [1974] shows how the fault surface is isolated in terms of the normal and tangential components of stress occurring at the interface. In Appendix B of the same reference, contact discontinuity boundary conditions are applied at the interface and the difference equations required to simulate the fault surface during rupture are given.

The basic mechanism for releasing the strain energy in this rupture model is the relaxation of the tangential stress at the slipping interface (fault surface) from its welded value to its kinetic friction value. This relaxation allows adjacent points on the interface to move apart (slip). The rupture heals (adjacent points on the interface stick), if the relative velocity between two adjacent points change sign and if the tangential stress at the interface is sufficient to maintain continuity of tangential velocity.

In the 2-D earthquake model the fault plane is of infinite extent in the direction perpendicular to the rupture direction while in the 3-D calculations the fault plane is of finite (specified) extent. In comparing calculations done to date, there is another significant difference. For all the 2-D calculations the faulting was unilateral while for the single 3-D calculation done to date the rupture was bilateral. This three-dimensional simulation of bilateral earthquake faulting is of primary interest here.

The configuration of the 3-D rupture model is illustrated schematically in Fig. 5.1. The primary model parameters characterizing the 3-D stick-slip earthquake source calculation are summarized below.

- The fault is located at the origin of a Cartesian (rectangular) coordinate system as shown in Fig. 5.1.
- The fault plane for the rupture model is in the X-Y plane.
- The rupture velocity has an average magnitude of V_R = 2.7 km/sec and is parallel to the Y-axis and in the positive Y direction for Y > 0 and in the negative Y direction for Y < 0, corresponding to a bilateral rupture. The direction of particle motion is indicated in the figure.
- The fault zone is defined by $-0.5 \leq Y \leq 0.5$ and $-0.3 \leq X \leq 0.3$, in units of kilometers, corresponding to a fault of length (L) 1.0 km and width (W) 0.6 km.
- The prestress is composed of a single component, S_{ZY} = -1 kbar. However, the stress drop across the fault boundary is taken to be 0.15 kbar.

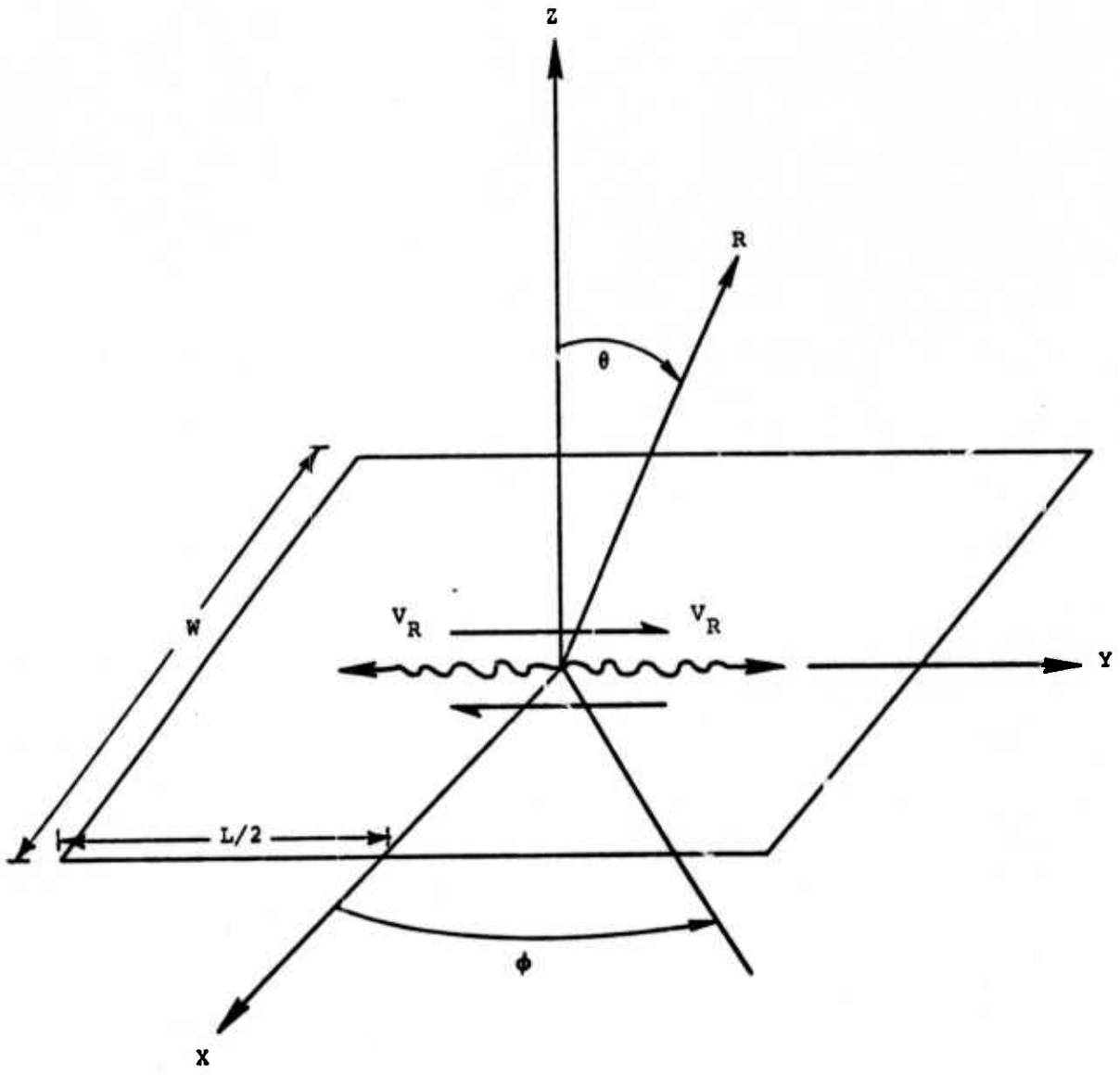

Figure 5.1. Configuration of the bilateral rupture model with fault length L, width W, and prestress component S_{ZY} as used in the 3-D finite difference earthquake source calculation. The relation between the Cartesian (X,Y,Z) and spherical (R,θ,ϕ) source coordinate systems is illustrated.

- The 3-D finite difference calculation used a rectangular grid system extending from 0.0 to 6.472 km in the X and Y directions and from -6.427 to +6.427 km in the Z direction. A total of 50 × 50 × 100 = 250,000 cells were required. The rectangular grid was evenly spaced with a grid length of 0.1 km from 0.0 to 3.0 km in all three directions; the grid was progressively stretched beyone 3.0 km. The time step was fixed at 0.005 sec and the numerical source calculation was run out to a total elapsed time of 1.2150 sec or a total of 243 cycles.

- A total of 319 monitoring stations were arranged in the neighborhood of the spherical surface of radius R = 1.5 km extending over one octant defined by $0° \leq \theta \leq 90°$ and $0° \leq \phi \leq 90°$, where θ is the colatitude measured from the Z-axis downward to a point on the sphere and ϕ is the azimuthal angle measured from the XZ plane. The primary source variables, namely the dilatation and rotation displacement potentials, at the centers of the eight rectangular cells surrounding each station were sampled for every time step. Also, the particle displacement and velocity field components were sampled at each monitoring station.

- The material properties in the elastic region are

P-wave velocity:	v_p = 5.7 km/sec
S-wave velocity:	v_s = 3.4 km/sec
Density:	ρ = 2.8 g/cc
Bulk modulus:	K = 478 kbar
Shear modulus:	μ = 324 kbar

As a consequence of the symmetry properties of the 3-D stick-slip earthquake source, a set of symmetry relations can be derived for the dilatation and rotation potentials. By applying these symmetry properties, numerical values of the potentials in the 2nd - 8th octants on the spherical surface can be related to values on the first octant. Therefore, the set of monitoring stations can be restricted to a single octant in three-dimensional space. This restriction allows a substantial reduction in the total computing expenditure required to carry out a full 3-D deterministic simulation of a stick-slip earthquake without any compromise of physical reality.

The symmetry properties and related displacement boundary conditions for the stick-slip bilateral rupture model are discussed in Appendix A. The derivation of the symmetry properties of the displacement potentials is also given in the same Appendix, along with a discussion of the special computational considerations required to treat stations near the boundary surfaces, represented by the XZ, YZ, and XY planes. Finally, the symmetry properties relating values of both displacement and potential fields to those in the first octant are summarized in Tables A.1 - A.3.

5.3 EQUIVALENT ELASTIC SOURCE REPRESENTATION

Fundamental to studies of the far-field signature of the 3-D finite difference simulation of a stick-slip earthquake is a representation of the rupture model in terms of an equivalent elastic source. The representation of a spatially limited source in terms of a multipole expansion in spherical harmonics has been discussed in a number of S^3 reports (e.g., Cherry, et al. [1975]; Bache, et al. [1974] and Bache, et al. [1975a]). Only the final analytic

expressions will be introduced here to provide a convenient starting point and to establish the notational conventions for the following discussions.

The Fourier transform of the displacement potentials is expanded in terms of spherical eigensolutions of the wave equation in a homogeneous, isotropic linearly elastic medium as follows:

$$\tilde{\chi}_\alpha\ (r,\theta,\phi,\omega) = \sum_{\ell=0}^{\infty} \sum_{m=0}^{\ell} \sum_{s=0}^{1} h_\ell^{(2)}\ (k_\alpha r)\ \tilde{A}_{\ell ms}^{(\alpha)}\ (\omega)\ Y_{\ell ms}\ (\theta,\phi)\ , \tag{5.1}$$

where $\tilde{A}_{\ell ms}^{(\alpha)}(\omega)$ are multipole coefficient, $h_\ell^{(2)}$ are spherical Hankel functions of the second kind, and $Y_{\ell ms}$ are (unnormalized) spherical harmonics (Morse and Feshbach [1953]), namely

$$Y_{\ell ms}\ (\theta,\phi) = \left\{ \begin{array}{l} P_\ell^m\ (\cos\theta)\ \cos m\phi,\ s=0 \\ \\ P_\ell^m\ (\cos\theta)\ \sin m\phi,\ s=1 \end{array} \right\}\ , \tag{5.2}$$

where P_ℓ^m are associated Legendre functions. The multipole coefficients in the time domain can be expressed in terms of the potentials as

$$A_{\ell ms}^{(\alpha)}\ (R,t) = \frac{1}{N_{\ell m}^2} \int_0^{2\pi} \int_0^{\pi} \chi_\alpha\ (R,\theta,\phi,t) \times Y_{\ell ms}\ (\theta,\phi)\ \sin\theta\ d\theta\ d\phi, \tag{5.3}$$

where the displacement potentials χ_α are defined by Eq. (A.11) in Appendix A, and the normalization factor $N_{\ell m}$ is

$$N_{\ell m}^2 = \frac{(4\pi/\varepsilon_m)\,(\ell+m)\,!}{(2\ell+1)\,(\ell-m)\,!} \tag{5.4}$$

with $\varepsilon_0 = 1$ and $\varepsilon_m = 2$, $m \neq 0$.

The multipole coefficients $\tilde{A}^{(\alpha)}_{\ell ms}(\omega)$ characterizing the earthquake source are then calculated by taking the Fourier transform

$$\begin{aligned} \tilde{A}^{(\alpha)}_{\ell ms}(\omega) &= \frac{1}{h_\ell^{(2)}(k_\alpha R)}\, \mathcal{F}\left[A^{(\alpha)}_{\ell ms}(R,t)\right] , \\ &= \frac{1}{h_\ell^{(2)}(k_\alpha R)} \int_{-\infty}^{\infty} A^{(\alpha)}_{\ell ms}(R,t)\, e^{-i\omega t}\, dt . \end{aligned} \tag{5.5}$$

The numerical calculation of the multipole coefficients in the time domain expressed by Eq. (5.3) is performed first by the series of general purpose computer program MULTEES described in Appendix G of Bache, et al. [1975a]. The 3-D Lagrangian finite difference code (TRES) was carried into the small displacement elastic region and linked to MULTEES. The saved quantities were time histories for the four potentials χ_α (α = 1, 2, 3, 4) defined at the centers of the eight rectangular cells surrounding a total of 319 monitoring stations. This set of monitoring stations was distributed over the first octant at grid points in the neighborhood of a spherical surface of radius R = 1.5 km with $0° \leq \theta \leq 90°$ and $0° \leq \phi \leq 90°$. A 3-D spatial interpolation routine is applied to derive values of the potentials at a pre-selected set of points on the spherical surface. Once this interpolation is accomplished, the double numerical integration over the two

angular variables θ and ϕ is performed as indicated in Eq. (5.3). The Fourier transform given in Eq. (5.5) is then computed, yielding the multipole coefficients which completely specify the equivalent elastic source.

5.4 THE EQUIVALENT ELASTIC SOURCE FOR THE BILATERAL RUPTURE

The symmetry properties of the stick-slip earthquake for the configuration illustrated in Fig. 5.1 are developed in Appendix A. These relations were applied to the double surface integrations defined by Eq. (5.3) to derive the set of nonvanishing multipole coefficients for the bilateral rupture model (see Appendix B). A summary of these coefficients is given in Table B.1. The notation introduced above for the coefficients is related to that used in earlier reports by $\tilde{A}^{(\alpha)}_{\ell m} \equiv \tilde{A}^{(\alpha)}_{\ell m o}$ and $\tilde{B}^{(\alpha)}_{\ell m} \equiv \tilde{A}^{(\alpha)}_{\ell m 1}$. Only even order terms are found to exist ($\ell = 0, 2, 4, 6, \ldots$); all terms of odd order are identically zero. There is a single nonzero monopole term $\tilde{A}^{(1)}_{oo}$. There are five quadrupole terms, which specify the double-couple portion of the equivalent elastic source, nine octupole terms, etc. The spectral ranges where such terms must be included to ensure convergence of the multipolar series will be a subject of later discussions.

In order to determine the general nature of the equivalent elastic source representation of the bilateral rupture, the spectral displacement potentials in the source coordinate system can be expressed explicitly in terms of the nonzero multipole coefficients as

$$\tilde{\chi}_1 (R,\theta,\phi,\omega) = \tilde{A}^{(1)}_{00}(\omega)\, h^{(2)}_0 (k_s R)$$
$$+ \Big[\tilde{A}^{(1)}_{20}(\omega)\, P^0_2 (\cos\theta)$$
$$+ \tilde{A}^{(1)}_{22}(\omega)\, P^2_2 (\cos\theta) \cos 2\phi\Big] h^{(2)}_2 (k_s R)$$
$$+ \Big[\tilde{A}^{(1)}_{40}(\omega)\, P^0_4 (\cos\theta) + \tilde{A}^{(1)}_{42}(\omega)\, P^2_4 (\cos\theta) \cos 2\phi$$
$$+ \tilde{A}^{(1)}_{44}(\omega)\, P^4_4 (\cos\theta) \cos 4\phi\Big] h^{(2)}_4 (k_s R)$$
$$+ \ldots , \qquad (5.6)$$

$$\tilde{\chi}_2 (R,\theta,\phi,\omega) = \tilde{B}^{(2)}_{22}(\omega)\, P^2_2 (\cos\theta) \sin 2\phi\, h^{(2)}_2 (k_s R)$$
$$+ \Big[\tilde{B}^{(2)}_{42}(\omega)\, P^2_4 (\cos\theta) \sin 2\phi$$
$$+ \tilde{B}^{(2)}_{44}(\omega)\, P^4_4 (\cos\theta) \sin 4\phi\Big] \times h^{(2)}_4 (k_s R)$$
$$+ \ldots , \qquad (5.7)$$

$$\tilde{\chi}_3 (R,\theta,\phi,\omega) = \tilde{A}^{(3)}_{21}(\omega)\, P^1_2 (\cos\theta) \cos\phi\, h^{(2)}_2 (k_s R)$$
$$+ \Big[\tilde{A}^{(3)}_{41}(\omega)\, P^1_4 (\cos\theta) \cos\phi$$
$$+ A^{(3)}_{43}(\omega)\, P^3_4 (\cos\theta) \cos 3\phi\Big] \times h^{(2)}_4 (k_s R)$$
$$+ \ldots , \qquad (5.8)$$

$$\tilde{\chi}_4 (R,\theta,\phi,\omega) = \tilde{B}^{(4)}_{21}(\omega)\, P^1_2 (\cos\theta) \sin\phi\, h^{(2)}_2 (k_p R)$$

$$+ \left[\tilde{B}^{(4)}_{41}(\omega)\, P^1_4 (\cos\theta) \sin\phi \right.$$

$$\left. + \tilde{B}^{(4)}_{43}(\omega)\, P^3_4 (\cos\theta) \sin 3\phi \right] \times h^{(2)}_4 (k_p R)$$

$$+ \ldots , \qquad (5.9)$$

where $k_s = \omega/v_s$ and $k_p = \omega/v_p$.

The radiation field is therefore made up of monopole ($\ell = 0$), quadrupole ($\ell = 2$), octupole ($\ell = 4$), and higher order even multipole terms. The monopole term corresponds to a rotation about the x-axis that is the same at every point on the surface of any sphere in the elastic region. The time history of the multipole coefficient $A^{(1)}_{00}(R,t)$ indicates that the propagating rupture produces primarily a positive rotation about the x-axis (in a positive rotation the y-axis rotates towards the z-axis as in the "right-hand rule") that is preceded and followed by a negative rotation about the same axis. There is no permanent offset so that the net effect of the monopole term is an oscillating rotation which returns the medium to its original state at long times. The presence of the monopole term is somewhat unusual, since even rather complex analytical earthquake source models such as Archambeau's [1964] do not generate such a term. Monopole radiation is spherically symmetric as, for example, the monopole or reduced displacement potential representation of an explosion. While perhaps it is not intuitively obvious, the excitation of S-wave monopole radiation is a reasonable consequence of the model formulation. In the model considered the prestress is assumed to be pure shear, with only a single nonvanishing component S_{ZY}. Since the fault plane is the XY plane, a rotational displacement potential with an X component is consistent with the prestress condition.

A dominantly quadrupole equivalent elastic source is expected for the fault model considered. The perturbation by the even multipoles of higher order is associated with the finite rupture propagation velocity. The absence of odd multipoles is found to be associated with the bilateral nature of the rupture.

The radiation pattern is specified by the Legendre functions $P_\ell^m(\cos\theta)$ and the trigonometric functions $\cos m\phi$ and $\sin m\phi$. The radial decay enters via the functions $h_\ell^{(2)}(k_\alpha r)$, which are spherical Hankel functions of the second kind, while the frequency dependence of the source is specified by the multipole coefficients $\tilde{A}_{\ell m}^{(\alpha)}(\omega)$.

The multipolar expansion for the equivalent elastic source is non-separable. As a consequence, discussions of the frequency behavior, spatial behavior, and the relative contribution of the various multipolar terms cannot be treated independently. Conclusions about the nature of the source must then be derived from displacement spectra and radiation patterns and, therefore, must consider the special conditions (spectral range, spatial location and series truncation) pertinent to the result under consideration.

The asymptotic behavior of the equivalent elastic source is described in Appendix C. In the low-frequency limit when $\omega << 1$, the far-field radiation is expected to be dominated by the quadrupole field, which depends on the first power of ω, namely,

$$|\tilde{\chi}_\alpha(R,\theta,\rho,\omega)| \sim \omega \tag{5.10}$$

for $k_\alpha R >> 1$ and $\omega << 1$. The monopole and higher-order terms in the potential spectrum behave as ω^2, ω^3, ω^5, etc. The asymptotic behavior of the far-field displacement spectrum in the low-frequency limit will be independent of frequency, approaching a DC spectral level.

In the high-frequency limit the far-field displacement spectrum is expected to behave as

$$|\tilde{u}_i(R,\theta,\rho,\omega)| \sim \omega^{-q} \tag{5.11}$$

for $\omega >> 1$ with $q \leq 3$. The high frequency behavior is more complex, since multipole fields of all orders contribute to the radiation. One objective in analyzing spectral amplitudes is to define the frequency range where the multipole series converges rapidly, so that retaining only the first few terms is sufficient to describe the radiation field at all frequencies of interest at teleseismic distances. High-frequency dispersion and errors due to the discrete grid used in the 3-D finite difference calculation introduce a high-frequency cutoff (Appendix D). The existence of such a cutoff limits the high-frequency information that can be extracted from the numerical source calculation. The cutoff frequencies for P and S waves for the 3-D stress wave calculation are estimated to be

$$f_c(P) \approx 5 \text{ Hz} \tag{5.12}$$

and

$$f_c(S) \approx 3 \text{ Hz}.$$

These high frequency limits will not affect the radiation of interest teleseismically, where frequencies of interest are generally below 1-3 Hz.

5.5 FAR-FIELD DISPLACEMENT SPECTRA

In this section the character of the far-field displacement spectra for the finite difference bilateral earthquake calculation is discussed. The far-field displacement field is composed of the radial or P-wave displacement $\tilde{u}_r$ and the two components of the S-wave, $\tilde{u}_\theta$ and $\tilde{u}_\phi$. Expressions for these displacements as functions of R, θ, ϕ, ω are

given by Eqs. (C.9 - C.14) of Appendix C. From these expressions we see that the R dependence is separable but that the dependence on the radiation pattern coordinates (θ, ϕ) is not. Spectra are therefore dependent on the portion of the radiation pattern sampled.

The coordinate system used for specifying position with respect to the fault is shown in Fig. 5.1. Therefore, for this discussion θ is the colatitude and is measured from the z-axis while ϕ is the azimuth measured from the x-axis. One usually thinks of the z-axis as being normal to the free surface, hence the nomenclature for θ and ϕ. However, this places the fault at an unusual and not very interesting orientation so this interpretation of the coordinate system is not pursued. Rather, the θ, ϕ locations are thought of with respect to the source coordinate system of Fig. 5.1. Minster [1973] has given a computationally convenient scheme for obtaining the multipole coefficients in a rotated coordinate system so the fault studied here can be represented at any desired orientation with respect to a free surface.

To portray the far-field displacement spectra radiated by the FDEQ it is necessary to show radiation patterns for specific frequency components and spectra at specific locations on the radiation patterns. These are shown in Figs. 5.2 - 5.4. Figures 5.2 and 5.3 show a fairly comprehensive sampling of radiation patterns while the three spectral plots are typical. In the radiation pattern plots only the u_θ component of the S-wave is shown for simplicity. Taken together, these plots give a detailed understanding of the far-field displacement spectra radiated by the FDEQ. In the radiation patterns illustrated in Figs. 5.2 and 5.3 the inner graph represents the P-wave pattern. Compressional (+) lobes and rarefaction (-) lobes are indicated by the plus and minus signs. In the S-wave patterns the direction of transverse particle motion is also indicated by arrows.

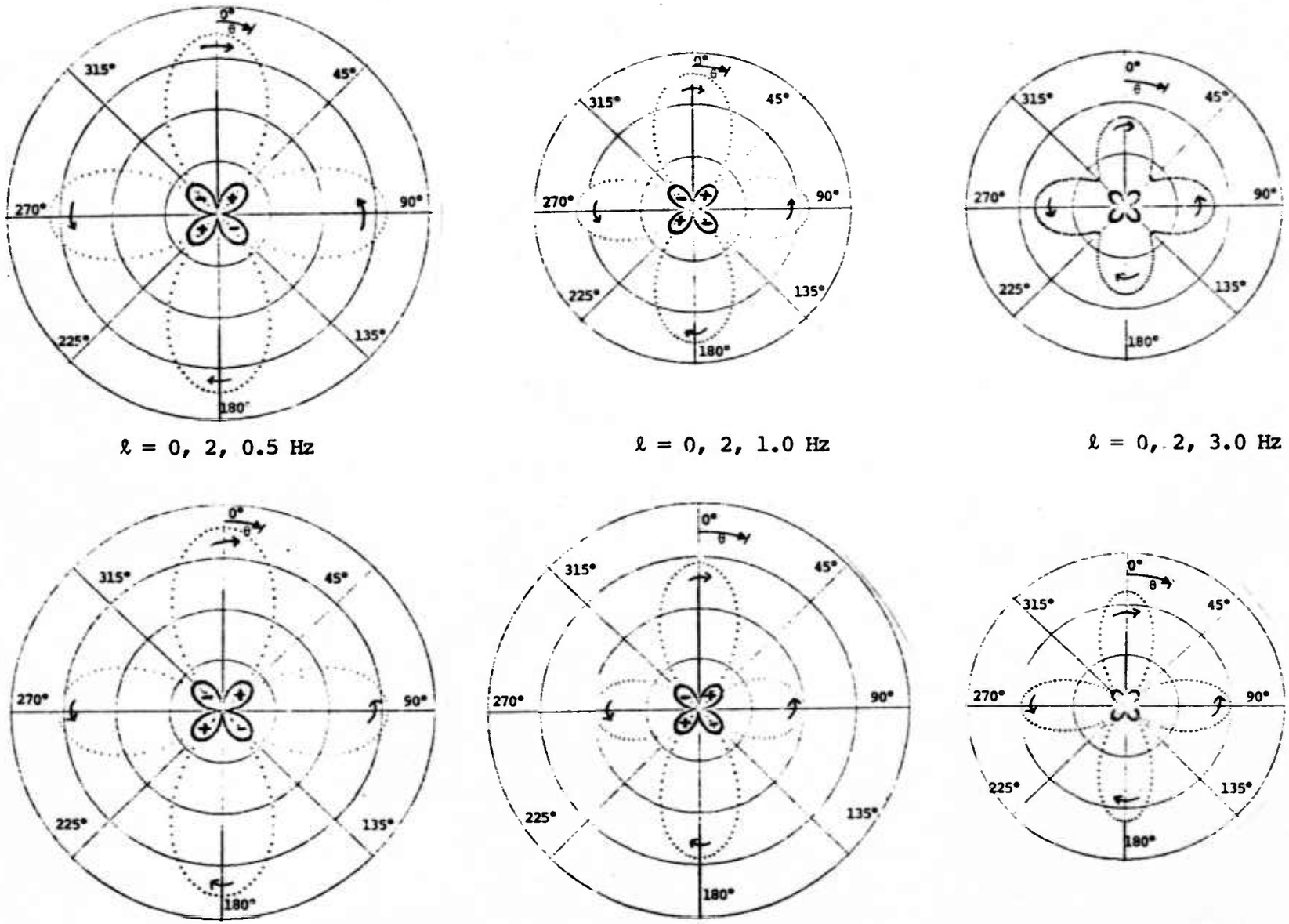

ℓ = 0, 2, 0.5 Hz

ℓ = 0, 2, 1.0 Hz

ℓ = 0, 2, 3.0 Hz

ℓ = 0, 2, 4, 0.5 Hz

ℓ = 0, 2, 4, 1.0 Hz

ℓ = 0, 2, 4, 3.0 Hz

Figure 5.2. Far-field radiation patterns for the 3-D finite difference earthquake source at azimuth $\phi = 90°$ and distance R = 1.5 km. Comparison of the top and bottom patterns shows the effect of retaining the octupole($\ell = 4$) term.

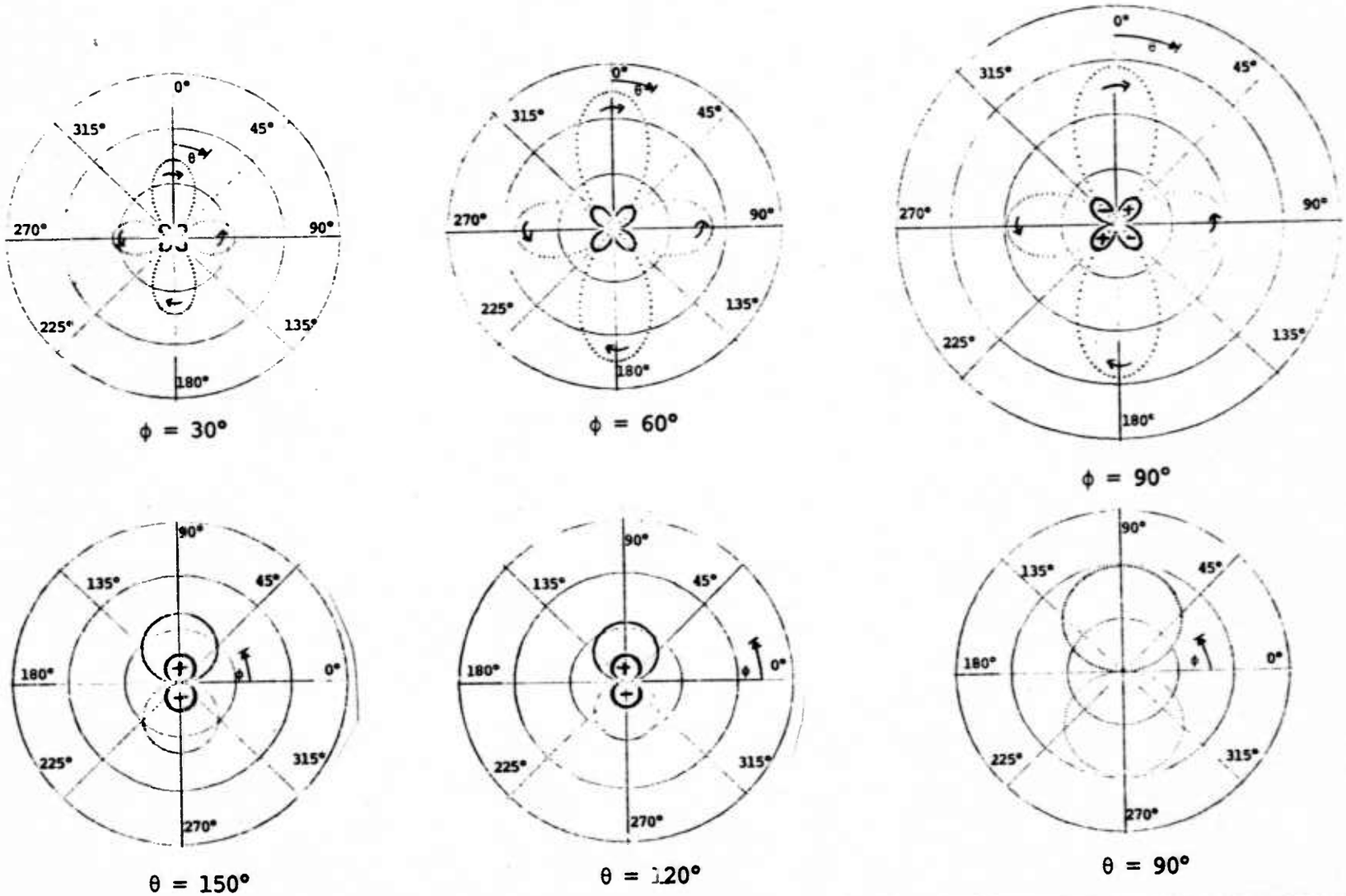

Figure 5.3. Far-field radiation patterns for the 3-D finite difference earthquake source for several azimuths and colatitudes. For each pattern the frequency is 1 Hz and terms through the octupole (ℓ = 0, 2, 4) were retained.

In Fig. 5.2 a number of radiation patterns are shown on the plane specified by $\phi = 90°$; that is, the ZY plane. In this figure $\theta = 0°$ is the +Z-axis, $\theta = 90°$ is the +Y axis, etc. The fault break is along the Y-axis. Recalling that the displacement spectra are inversely proportional to R, the displacements in the figures are scaled to 1.5 kilometers, the elastic radius. The radiation patterns are for three frequencies spanning the teleseismic band and show the influence of the octupole term. In the top three plots only the monopole and quadrupole terms were retained in computing the displacements ($\ell = 0, 2$). In the bottom three plots the octupole term ($\ell = 0, 2, 4$) was included. From Fig. 5.2 we deduce the following:

- At 0.5 Hz the source is essentially a pure double-couple. The deviations from double-couple symmetry are quite small.
- At 1.0 Hz the contribution of the monopole and quadrupole terms becomes evident in the S-wave pattern. At this frequency the monopole causes a noticeable asymmetry in the pattern which is enhanced by the addition of the octupole. For the more complete solution the vertically radiated "+" u_θ waves are nearly 1.5 times as large as those radiated from the ends of the fault. For a pure double-couple source the two would, of course, be equal.
- At 3.0 Hz the monopole and octupole are larger yet compared to the quadrupole source.
- Retaining terms through the octupole ($\ell = 0, 2, 4$) is found to be sufficient for frequencies to 3.0 Hz or a little longer. Beyond this, higher-order terms begin to be felt.

- Even for this small earthquake, terms other than the quadrupole contain significant information for far-field radiation at frequencies observed teleseismically.

The patterns of Fig. 5.2 are all for radiation in the ZY plane. A series of patterns at different slices are shown in Fig. 5.3. The patterns are all with ℓ = 0, 2, 4 and at 1.0 Hz. Three azimuths (ϕ = 30°, 60°, 90°) and three colatitudes (θ = 90°, 120°, 150°) are shown. These are shown to indicate that the conclusions drawn above are not influenced by the particular azimuth chosen.

In Figs. 5.4 are shown spectra for all three components of displacement at representative locations on the radiation pattern. The plotted spectra are for the azimuths ϕ = 30°, 60°, 90° and the colatitudes θ = 90°, 120°, 150°. For these spectra, the following comments are appropriate:

- Only u_ϕ is radiated at θ = 90°; that is, in the XY plane.
- The S-wave radiation is entirely u_θ at ϕ = 90°.
- The spectral shape is quite simple for all frequencies, being flat at low frequency and rolling off smoothly at high frequencies.
- Inequality between the θ = 120° and θ = 150° components of u_r and u_θ is a measure of the asymmetry introduced by the monopole and octupole terms.
- At low frequency the source is nearly pure quadrupole or double-couple.
- The spectral shape is essentially unchanged for all ϕ and θ shown. The spectra merely scale according to their ratios at a single

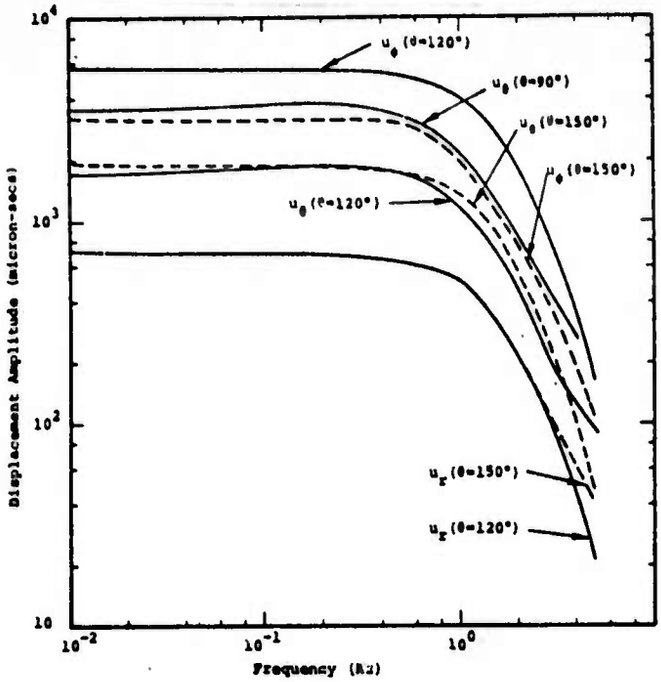

ϕ = 30°

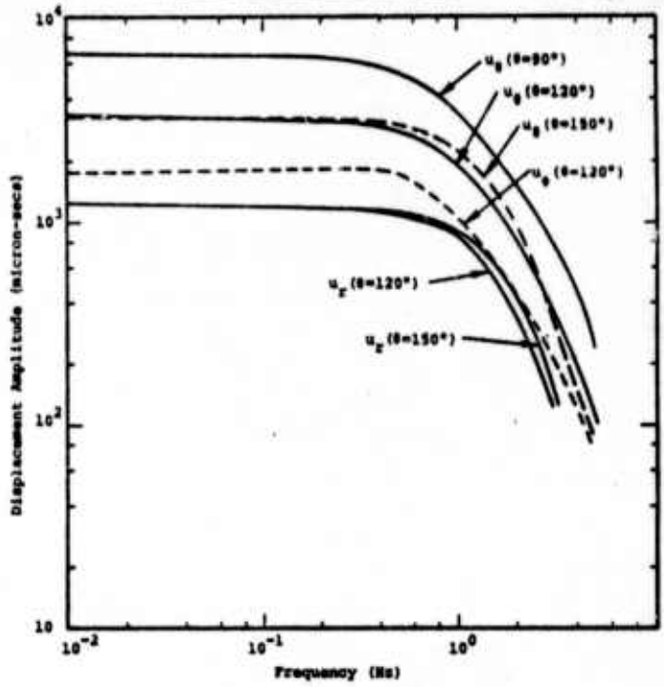

ϕ = 60°

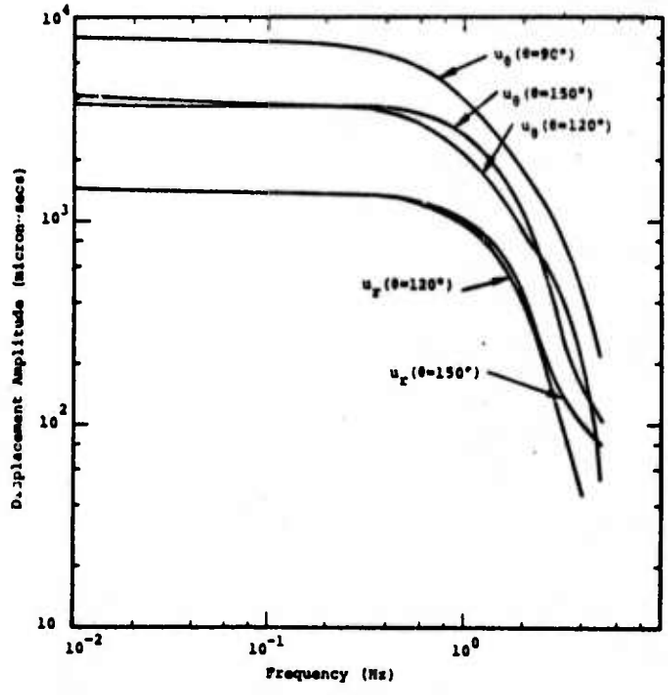

ϕ = 90°

Figure 5.4. Far-field spectral amplitudes for the finite difference earthquake source, ℓ = 0, 2, 4, R = 1.5 km.

frequency. That is, these representative spectra together with radiation patterns (Figs. 5.2 - 5.3) completely describe the displacement spectra from the FDEQ.

Two other features of the spectra are of interest, the P/S amplitude ratio and the corner frequency. For the P/S ratio the radiation pattern effect is deleted by considering only the peak values on the respective P and S patterns. Then for this study we define

$$P/S\ (\omega) = \frac{(\tilde{u}_r(R,\ \theta = 45°,\ \phi = 90°,\ \omega))}{(\tilde{u}_\theta(R,\ \theta = 0°,\ \phi = 90°,\ \omega))} \quad . \tag{5.13}$$

At low frequencies, i.e., in the flat portion of the spectra, this ratio is 0.22. At 1.0 Hz the P/S ratio decreases to 0.20 while P/S (3.0 Hz) = 0.15. Therefore, the P/S ratio is constant at low frequencies and decreases at higher frequencies.

Corner frequency is a somewhat arbitrary quantity. The usual technique is to draw asymptotes to the high and low frequency portions of the spectrum and identify their intersection with the corner frequency. Following this procedure with the spectra in Fig. 5.4, we find the corner frequencies to be weakly dependent on azimuth but to be in the range 1.3 - 1.7 Hz for both P and S waves. Blandford [1975] suggests that corner frequency be defined as that frequency at which the displacement spectrum is half its low frequency limit. Following this procedure, we find the corner frequencies to be nearly independent of azimuth and to have the values

$$f_0^{(P)} = 1.50 \text{ Hz} ,$$
$$f_0^{(S)} = 1.55 \text{ Hz} . \tag{5.14}$$

In either case, the FDEQ does not exhibit corner frequencies that are substantially different for P and S waves. This result is at variance from the observation by a number of authors that the corner frequencies for P are higher than for S.

The corner frequency is often used to estimate the earthquake source dimension D using the relationship

$$D = \frac{C_{P,S}\, V_S}{f_0^{P,S}} \tag{5.15}$$

where V_S is the S velocity. For example, Brune [1970] gives $C_{P,S} = 0.37$. Wyss and Shaney [1975] recently determined $C_{P,S}$ for two deep earthquakes to be

$$C_P = 0.41 - 0.45 \,, \qquad C_S = 0.30 - 0.36 \,, \tag{5.16}$$

which are consistent with Brune's results.

For the FDEQ we have $V_S = 3.4$ km/sec while the fault zone had a length and width of 1.0 km and 0.6 km. If we take $f_0 = 1.5$ Hz, $C_{P,S} = 0.37$, we find from (5.15) that $D \approx 0.84$ km, a value which is quite consistent with the fault dimensions of the FDEQ.

VI. REFERENCES

Aki, K. and Y. Tsai [1972], "The Mechanism of Love Wave Excitation by Explosive Sources," J. Geophys. Res., 77, pp. 1452-1475.

Archambeau, C. B. [1964], Elastodynamic Source Theory, Ph.D. Thesis, California Institute of Technology.

Archambeau, C. B. [1968], "General Theory of Elastodynamic Source Fields," Rev. of Geophys., 6, p. 241.

Archambeau, C. B., E. A. Flinn and D. G. Lambert [1969], "Fine Structure of the Upper Mantle," J. Geophys. Res., 74, pp. 5825-5865.

Archambeau, C. B. and C. Sammis [1970], "Seismic Radiation from Explosions in Prestressed Media and the Measurement of Tectonic Stress in the Earth," Rev. of Geophys., 8, p. 473.

Archambeau, C. B. [1972], "The Theory of Stress Wave Radiation from Explosions in Prestressed Media," Geophys. J. Roy. Astr. Soc., 29, p. 329.

Bache, T. C., J. T. Cherry, and J. M. Savino [1974], "Application of Advanced Methods for Identification and Detection of Nuclear Explosions from the Asian Continent," Systems, Science and Software Semi-annual Report, SSS-R-75-2483.

Bache, T. C., J. T. Cherry, K. G. Hamilton, J. F. Masso and J. M. Savino [1975a], "Application of Advanced Methods for Identification and Detection of Nuclear Explosions from the Asian Continent," Systems, Science and Software Semi-annual Report, SSS-R-75-2646.

Bache, T. C., J. T. Cherry, N. Rimer, J. M. Savino, T. R. Blake, T. G. Barker and D. G. Lambert [1975b], "An Exploration of the Relative Amplitudes Generated by Explosions in Different Test Areas at NTS," Systems, Science and Software Final Report (Draft), SSS-R-76-2746, October.

Båth, M. [1968], Mathematical Aspects of Seismology, Elsevier Publishing Company, New York, p. 58.

Blandford, R. R. [1975], "A Source Theory for Complex Earthquakes, Bull. Seism. Soc. Am., 65, pp. 1385-1406.

Bocre, D. M. [1972], "Finite Difference Methods for Seismic Wave Propagation in Heterogeneous Materials," in Methods in Computational Physics, B. A. Bolt (ed.), Academic Press, New York.

Bracewell, P. N. [1965], The Fourier Transform and Its Applications, McGraw-Hill, New York.

Brune, J. N. [1970], "Tectonic Stress and the Spectra of Seismic Shear Waves from Earthquakes," J. Geophys. Res., 75, pp. 4997-5009.

Bullen, K. E. [1965], An Introduction to the Theory of Seismology, Cambridge University Press, Cambridge.

Cerveny, V. and R. Ravindra [1971], Theory of Seismic Head Waves, University of Toronto Press.

Cherry, J. T. [1973], "Calculations of Near Field Earthquake Ground Motion," Systems, Science and Software Report SSS-R-73-1759.

Cherry, J. T., C. B. Archambeau, G. A. Frazier, A. J. Good, K. G. Hamilton and D. J. Harkrider [1973], "The Teleseismic Radiation Field from Explosions: Dependence of Seismic Amplitudes upon Properties of Materials in the Source Region," Systems, Science and Software Final Contract Report, DNA 3113Z.

Cherry, J. T. [1974], "Near Field Small Earthquake-Computer Simulation," Systems, Science and Software Report SSS-R-75-2475.

Cherry, J. T., T. C. Bache and C. B. Archambeau [1974a], "A Deterministic Approach to the Prediction of Teleseismic Ground Motion from Nuclear Explosions," Systems, Science and Software Final Contract Report, DNA 2231F.

Cherry, J. T., E. J. Halda and K. G. Hamilton [1974b], "A Deterministic Approach to the Prediction of Free Field Ground Motion and Response Spectra from Stick-Slip Earthquakes," Systems, Science and Software Report submitted for publication in Earthquake Engineering and Structural Dynamics.

Cherry, J. T., T. C. Bache and D. F. Patch [1975], "The Teleseismic Ground Motion Generated by a Nuclear Explosion in a Tunnel and Its Effects on the M_S/m_b Discriminant," Systems, Science and Software Final Contract Report, DNA 3645F.

Ewing, W. M., W. S. Jardetsky and F. Press [1957], Elastic Waves in Layered Media, McGraw-Hill, New York.

Haskell, N. A. [1962], "Crustal Reflection of Plane P and SV Waves," J. Geophys. Res., 67, pp. 4751-4767.

Herrin, E., et al. [1968], Bull. Seis. Soc. Am., 58, p. 1193.

Julian, B. R. and D. L. Anderson [1968], "Travel Times, Apparent Velocities and Amplitudes of Body Waves," Bull. Seismol. Soc. Amer., 58, p. 339.

Kisslinger, Carl [1971], "Seismological Instrumentation," International Institute of Earthquake Engineering Lecture Notes No. 2 (revised), Tokyo, Japan.

Lambert, D. G., E. A. Flinn and C. B. Archambeau [1972], "A Comparative Study of the Elastic Wave Radiation from Earthquakes and Underground Explosions," Geophys. J. Roy. Astr. Soc., 29, p. 403.

Manchee, E. B. and H. Somers [1966], "The Yellowknife Seismological Array," Publications of the Dominion Observatory, 32, No. 2, 84 pages.

Minster, J. B. [1973], "Elastodynamics of Failure in a Continuum," Ph.D. Thesis, California Institute of Technology, Pasadena.

Press, F. and C. B. Archambeau [1962], "Release of Tectonic Strain by Underground Nuclear Explosions," J. Geophys. Res., 67, p. 337.

Randall, M. J. [1966], "Seismic Radiation from a Sudden Phase Transition," J. Geophys. Res., 71, p. 5297.

Smith, S. W., C. B. Archambeau and W. Gile [1969], "Transient and Residual Strains from Large Underground Explosions," Bull. Seism. Soc. Am., 56, pp. 2185-2196.

Snoke, J. A. [1975], "Archambeau's Elastodynamic Source Model Solution and Low-Frequency Spectral Peaks in the Far-Field Displacement Amplitude from Earthquakes or Explosions," submitted to Geophysical Journal.

Strick, E. [1970], "A Predicted Pedestal Effect for Pulse Propagation in Constant-Q Solids," Geophysics, 35, pp. 387-403.

Toksoz, M. N. and H. H. Kehrer [1972], "Tectonic Strain Release by Underground Nuclear Explosions and Its Effect on Seismic Discrimination," Geophys. J. Roy. Astr. Soc., 31, pp. 141-161.

Wyss, M. and L. J. Shamey [1975], "Source Dimensions of Two Deep Earthquakes Estimated from Aftershocks and Spectra," Bull. Seism. Soc. Am., 65, pp. 403-409.

APPENDIX A

SYMMETRY PROPERTIES OF THE STICK-SLIP RUPTURE SOURCE MODEL

A.1 SYMMETRY PROPERTIES OF THE PARTICLE DISPLACEMENT FIELD

The symmetry properties of the particle displacement field are a consequence of the specific set of boundary conditions chosen for the stresses at the fault plane. This set of boundary conditions is required to complete the definition of the stick-slip rupture model. In order to check the validity of the boundary specifications incorporated in the 3-D finite difference stress wave code (TRES), a full-grid computation was performed for a limited number (11) of time cycles. The fault center was located at the origin of a rectangular coordinate system, identified by the cell indices (26,26,26). A detailed examination was made of the particle displacements (u, v, w), and velocities ($\dot{u}$, $\dot{v}$, $\dot{w}$) at the grid points defining the eight cells surrounding the fault center. A comparison of the displacement and velocity components at the grid point (27,27,27) in the first octant with the points (25,27,27), (25,25,27), (27,25,27), (27,27,25), (25,27,25), (25,25,25) and (27,25,25) representing points in the 2nd, 3rd, 4th, 5th, 6th, 7th and 8th octants, respectively, yields a set of symmetry relations and boundary conditions for the particle displacement and velocity fields. The fault plane lies in the XY plane and rupture propagates along the Y-axis (see Fig. 5.1).

Reflection across the YZ plane from the 1st to the 2nd octant yields

$$\begin{aligned} u(-x,y,z,t) &= -u(x,y,z,t) \ , \\ v(-x,y,z,t) &= +v(x,y,z,t) \ , \\ w(-x,y,z,t) &= +w(x,y,z,t) \ , \end{aligned} \tag{A.1}$$

and in the YZ plane (x=0) the boundary condition is

$$u(0,y,z,t) = \dot{u}(0,y,z,t) = 0 \,. \tag{A.2}$$

Reflection across the XZ plane from the 2nd to the 3rd octant yields

$$\begin{aligned} u(-x,-y,z,t) &= +u(x,y,z,t) \,, \\ v(-x,-y,z,t) &= +v(x,y,z,t) \,, \\ w(-x,-y,z,t) &= -w(x,y,z,t) \,. \end{aligned} \tag{A.3}$$

Reflection across the XZ plane from the 4th to the 1st octant yields

$$\begin{aligned} u(x,-y,z,t) &= -u(x,y,z,t) \,, \\ v(x,-y,z,t) &= +v(x,y,z,t) \,, \\ w(x,-y,z,t) &= -w(x,y,z,t) \,, \end{aligned} \tag{A.4}$$

and in the XZ plane (y=0) the boundary conditions are

$$\begin{aligned} u(x,0,z,t) &= \dot{u}(x,0,z,t) = 0 \,, \\ w(x,0,z,t) &= \dot{w}(x,0,z,t) = 0 \,. \end{aligned} \tag{A.5}$$

Reflection across the XY plane from the 1st to the 5th octant yields

$$\begin{aligned} u(x,y,-z,t) &= -u(x,y,z,t) \,, \\ v(x,y,-z,t) &= -v(x,y,z,t) \,, \\ w(x,y,-z,t) &= +w(x,y,z,t) \,. \end{aligned} \tag{A.6}$$

Similar properties are found relating displacements between the 6th and 2nd, 7th and 3rd, and 8th and 4th octants. The boundary conditions at the XY plane (z=0) are

$$\begin{aligned} u(x,y,0,t) &= \dot{u}(x,y,0,t) = 0 \,, \\ v(x,y,0,t) &= \dot{v}(x,y,0,t) = 0 \,. \end{aligned} \tag{A.7}$$

On the Z-axis (x=y=0),

$$u(0,0,z,t) = 0 \ .$$

$$w(0,0,z,t) = 0 \ .$$

Since the pressure is a zone-centered variable, values of P at the center of each of the eight cells surrounding the fault center at grid indices (26,26,26) were examined. The following symmetry properties for the pressure were derived:

Octant

$$\begin{aligned}
&2 \quad P(-x,y,z,t) = +P(x,y,z,t) \ , \\
&3 \quad P(-x,-y,z,t) = -P(x,y,z,t) \ , \\
&4 \quad P(x,-y,z,t) = -P(x,y,z,t) \ , \\
&5 \quad P(x,y,-z,t) = -P(x,y,z,t) \ , \\
&6 \quad P(-x,y,-z,t) = -P(x,y,z,t) \ , \\
&7 \quad P(-x,-y,-z,t) = +P(x,y,z,t) \ , \\
&8 \quad P(x,-y,-z,y) = +P(x,y,z,t) \ .
\end{aligned} \tag{A.8}$$

The boundary conditions observed for the pressure are

$$\begin{aligned}
&P(x,0,z,t) = 0 \quad \text{XZ plane} \ , \\
&P(x,y,0,t) = 0 \quad \text{XY plane} \ .
\end{aligned} \tag{A.9}$$

The symmetry properties of the rupture model source are given for the particle displacement field in Table A.1. The symbols u, v, and w represent the X, Y, and Z components of the displacement field. Values for the displacement components in each octant are related to the corresponding values in the first octant. Consequently, particle displacements, velocities, and potentials at all points of interest on the surface of the sphere in the elastic region can be derived from the time histories generated by the numerical source calculation for the first octant.

TABLE A.1. SYMMETRY PROPERTIES OF THE DISPLACEMENT FIELD (RECTANGULAR COORDINATES) FOR THE RUPTURE MODEL

(u, v, w = X, Y, and Z component of particle displacement)

Octant	
2	$u(-x,y,z) = -u(x,y,z)$
	$v(-x,y,z) = +v(x,y,z)$
	$w(-x,y,z) = +w(x,y,z)$
3	$u(-x,-y,z) = +u(x,y,z)$
	$v(-x,-y,z) = +v(x,y,z)$
	$w(-x,-y,z) = -w(x,y,z)$
4	$u(x,-y,z) = -u(x,y,z)$
	$v(x,-y,z) = +v(x,y,z)$
	$w(x,-y,z) = -w(x,y,z)$
5	$u(x,y,-z) = -u(x,y,z)$
	$v(x,y,-z) = -v(x,y,z)$
	$w(x,y,-z) = +w(x,y,z)$
6	$u(-z,y,-z) = +u(x,y,z)$
	$v(-z,y,-z) = -v(x,y,z)$
	$w(-z,y,-z) = +w(x,y,z)$
7	$u(-x,-y,-z) = -u(x,y,z)$
	$v(-x,-y,-z) = -v(x,y,z)$
	$w(-x,-y,-z) = -w(x,y,z)$
8	$u(x,-y,-z) = +u(x,y,z)$
	$v(x,-y,-z) = -v(x,y,z)$
	$w(x,-y,-z) = -w(x,y,z)$

While the source symmetry properties are first defined in rectangular coordinates corresponding to the use of a rectangular grid system in the 3-D finite difference source code, in studies of the far-field displacement spectra spherical components are of most interest. Symmetry properties for the displacement field in spherical coordinates derived from the following coordinate transformation are presented in Table A.2.

$$u_r(r,\theta,\phi) = \sin\theta\cos\phi\, u + \sin\theta\sin\phi\, v + \cos\theta\, w ,$$
$$u_\theta(r,\theta,\phi) = \cos\theta\cos\phi\, u + \cos\theta\sin\phi\, v - \sin\theta\, w , \qquad (A.10)$$
$$u_\phi(r,\theta,\phi) = -\sin\phi\, u + \cos\phi\, v .$$

A.2 SYMMETRY PROPERTIES OF THE DISPLACEMENT POTENTIALS

The (scalar) dilatation displacement potential and the (vector) rotation displacement potential are defined in terms of the displacement field $\underset{\sim}{u}(\underset{\sim}{r},t)$ by,

$$\chi^{(4)} = \nabla \cdot \underset{\sim}{u} ,$$
$$\underset{\sim}{\chi} = \frac{1}{2} \nabla \times \underset{\sim}{u} . \qquad (A.11)$$

The symmetry properties of the potentials can therefore be derived from these for the displacement field. The results of this derivation are given in Table A.3 for χ_4 and the rectangular components of $\underset{\sim}{\chi}$. Since the pressure is directly proportional to the dilatation

$$P = -K \nabla \cdot u , \qquad (A.12)$$

where K is the bulk modulus, the symmetry properties derived for χ_4 via those for u, v, and w are identical to those observed for the pressure given in Eq. (A.8).

TABLE A.2. SYMMETRY PROPERTIES OF THE DISPLACEMENT FIELD (SPHERICAL COORDINATES) FOR THE RUPTURE MODEL

(u_r, u_θ, u_ϕ = spherical components of particle displacement)

Octant	
2	$u_r(r,\theta,\pi-\phi) = + u_r(r,\theta,\phi)$
	$u_\theta(r,\theta,\pi-\phi) = + u_\theta(r,\theta,\phi)$
	$u_\phi(r,\theta,\pi-\phi) = - u_\phi(r,\theta,\phi)$
3	$u_r(r,\theta,\pi+\phi) = - u_r(r,\theta,\phi)$
	$u_\theta(r,\theta,\pi+\phi) = - u_\theta(r,\theta,\phi)$
	$u_\phi(r,\theta,\pi+\phi) = - u_\phi(r,\theta,\phi)$
4	$u_r(r,\theta,-\phi) = - u_r(r,\theta,\phi)$
	$u_\theta(r,\theta,-\phi) = - u_\theta(r,\theta,\phi)$
	$u_\phi(r,\theta,-\phi) = + u_\phi(r,\theta,\phi)$
5	$u_r(r,\pi-\theta,\phi) = - u_r(r,\theta,\phi)$
	$u_\theta(r,\pi-\theta,\phi) = + u_\theta(r,\theta,\phi)$
	$u_\phi(r,\pi-\theta,\phi) = - u_\phi(r,\theta,\phi)$
6	$u_r(r,\pi-\theta,\pi-\phi) = - u_r(r,\theta,\phi)$
	$u_\theta(r,\pi-\theta,\pi-\phi) = + u_\theta(r,\theta,\phi)$
	$u_\phi(r,\pi-\theta,\pi-\phi) = + u_\phi(r,\theta,\phi)$
7	$u_r(r,\pi-\theta,\pi+\phi) = + u_r(r,\theta,\phi)$
	$u_\theta(r,\pi-\theta,\pi+\phi) = - u_\theta(r,\theta,\phi)$
	$u_\phi(r,\pi-\theta,\pi+\phi) = + u_\phi(r,\theta,\phi)$
8	$u_r(r,\pi-\theta,-\phi) = + u_r(r,\theta,\phi)$
	$u_\theta(r,\pi-\theta,-\phi) = - u_\theta(r,\theta,\phi)$
	$u_\phi(r,\pi-\theta,-\phi) = - u_\phi(r,\theta,\phi)$

TABLE A.3. SYMMETRY PROPERTIES OF THE POTENTIAL FUNCTIONS IN RECTANGULAR COORDINATES FOR THE RUPTURE MODEL

Octant	
2	$\chi_4(-x,y,z) = +\chi_4(x,y,z)$
3	$\chi_4(-x,-y,z) = -\chi_4(x,y,z)$
4	$\chi_4(x,-y,z) = -\chi_4(x,y,z)$
5	$\chi_4(x,y,-z) = -\chi_4(x,y,z)$
6	$\chi_4(-x,y,-z) = -\chi_4(x,y,z)$
7	$\chi_4(-x,-y,-z) = +\chi_4(x,y,z)$
8	$\chi_4(x,-y,-z) = +\chi_4(x,y,z)$
2	$\chi_1(-x,y,z) = +\chi_1(x,y,z)$
3	$\chi_1(-x,-y,z) = +\chi_1(x,y,z)$
4	$\chi_1(x,-y,z) = +\chi_1(x,y,z)$
5	$\chi_1(x,y,-z) = +\chi_1(x,y,z)$
6	$\chi_1(-x,y,-z) = +\chi_1(x,y,z)$
7	$\chi_1(-x,-y--z) = +\chi_1(x,y,z)$
8	$\chi_1(x,-y,-z) = +\chi_1(x,y,z)$

TABLE A.3. (Continued)

2	$\chi_2(-x,y,z) = -\chi_2(x,y,z)$
3	$\chi_2(-x,-y-z) = +\chi_2(x,y,z)$
4	$\chi_2(x,-y,z) = -\chi_2(x,y,z)$
5	$\chi_2(x,y,-z) = +\chi_2(x,y,z)$
6	$\chi_2(-x,y,-z) = -\chi_2(x,y,z)$
7	$\chi_2(-x,-y,-z) = +\chi_2(x,y,z)$
8	$\chi_2(x,-y,-z) = -\chi_2(x,y,z)$
2	$\chi_3(-x,y,z) = -\chi_3(x,y,z)$
3	$\chi_3(-x,-y,z) = -\chi_3(x,y,z)$
4	$\chi_3(x,-y,z) = +\chi_3(x,y,z)$
5	$\chi_3(x,y,-z) = -\chi_3(x,y,z)$
6	$\chi_3(-x,y,-z) = +\chi_3(x,y,z)$
7	$\chi_3(-x,-y,-z) = +\chi_3(x,y,z)$
8	$\chi_3(x,-y-,z) = -\chi_3(x,y,z)$

Two examples will illustrate the method employed above. From the definition of the dilatation potential,

$$\chi_4(x,y,z,t) = \frac{\partial u}{\partial x}(x,y,z,t) + \frac{\partial v}{\partial y}(x,y,z,t) + \frac{\partial w}{\partial z}(x,y,z,t) . \tag{A.13}$$

Applying the properties in Table A.1 for the 2nd octant yields

$$\begin{aligned} \chi_4(-x,y,z,t) &= \frac{\partial u}{\partial(-x)}(-x,y,z,t) + \frac{\partial v}{\partial y}(-x,y,z,t) \\ &\quad + \frac{\partial w}{\partial z}(x,y,z,t) , \\ &= + \chi_4(x,y,z,t) . \end{aligned} \tag{A.14}$$

From the definition of the rotation potential,

$$\begin{aligned} \chi_1 &= \frac{1}{2}[\text{curl } \underset{\sim}{u}]_x = \frac{1}{2}\left(\frac{\partial w}{\partial y} - \frac{\partial v}{\partial z}\right) , \\ \chi_1(x,-y,z,t) &= \frac{1}{2}\left(-\frac{\partial w}{\partial(-y)} - \frac{\partial v}{\partial(-z)}\right) , \\ &= \chi_1(x,y,z,t) . \end{aligned} \tag{A.15}$$

The relationships for the other octants and other potential functions are derived in a similar manner.

As a consequence of the symmetry properties for the potential functions the following boundary conditions were observed in the time histories generated by the 3-D finite difference source code:

1. On the X-Z plane corresponding to y=0 or ϕ=0°

$$\chi_4(R,\theta,\ 0,t) = 0\ ,$$
$$\chi_2(R,\theta,\ 0,t) = 0\ . \qquad \text{(A.16)}$$

2. On the Y-Z plane corresponding to x=0 or ϕ=90°

$$\chi_2(R,\theta,\pi/2,t) = 0\ ,$$
$$\chi_3(R,\theta,\pi/2,t) = 0\ . \qquad \text{(A.17)}$$

3. On the X-Y (fault) plane corresponding to z=0 or θ=90°

$$\chi_4(R,\pi/2,\phi,t) = 0\ ,$$
$$\chi_3(R,\pi/2,\phi,t) = 0\ . \qquad \text{(A.18)}$$

4. On the Z-axis corresponding to x=y=0 or θ=0°

$$\chi_2(R,0,\phi,t) = 0\ ,$$
$$\chi_3(R,0,\phi,t) = 0\ , \qquad \text{(A.19)}$$
$$\chi_4(R,0,\phi,t) = 0\ .$$

A.3 APPLICATION OF SYMMETRY PROPERTIES TO BOUNDARY STATIONS

A principal application of the symmetry properties for the potential functions is the determination of the χ_α for monitoring stations on boundaries of the first octant in which the 3-D finite difference calculation is carried out. As described in Bache, et al. [1975a], in order to perform the double numerical integration defined in Eq. (5.3), values of

χ_α must be available at selected integration points on the surface of the sphere of fixed radius in the elastic region. The 3-D finite difference code generates time histories for χ_α at the centers of the eight cells surrounding each of the monitoring or "save" stations defined at selected grid points. The notation for labeling these 8 cells is according to Bache, et al. [1975a]. A cell is identified by the three indices of the grid point with the three highest integer values. The station (I,J,K) will sample χ_α's at the centers of the following eight cells, in the sequence indicated:

1. I+1, J+1, K+1
2. I, J+1, K+1
3. I, J, K+1
4. I+1, J, K+1
5. I+1, J+1, K
6. I, J+1, K
7. I, J, K
8. I+1, J, K

(A.20)

The MULTEES program applies a 3-D spatial interpolation routine in order to calculate values of χ_α at the integration points of interest. The set of χ_α generated by the 3-D source code is deficient, whenever the monitoring station is located near the XY, YZ, or XZ planes, which form the boundaries of the first octant in which the χ_α are located.

If a monitoring station is on the Y-Z plane (x=0), ϕ=90°), χ_α are available only for cells 1, 4, 5 and 8 surrounding the station. Applying the symmetry relations for the 2nd octant yields,

$$\left.\begin{aligned} \chi_\alpha(2) &= \chi_\alpha(1) \\ \chi_\alpha(3) &= \chi_\alpha(4) \\ \chi_\alpha(6) &= \chi_\alpha(5) \\ \chi_\alpha(7) &= \chi_\alpha(8) \end{aligned}\right\} \quad \alpha = 1,4$$

$$\left.\begin{aligned} \chi_\alpha(2) &= -\chi_\alpha(1) \\ \chi_\alpha(3) &= -\chi_\alpha(4) \\ \chi_\alpha(6) &= -\chi_\alpha(5) \\ \chi_\alpha(7) &= -\chi_\alpha(8) \end{aligned}\right\} \quad \alpha = 2,3 \qquad \text{(A.21)}$$

where the integers in parentheses refer to the cell numbers defined according to the sequence in Eq. (A.20).

If the station is on the X-z plane (y=0, ϕ=0°), χ_α are available only for cells 1, 2, 5 and 6 surrounding the station. Applying the symmetry relations for the 4th octant yields,

$$\left.\begin{aligned} \chi_\alpha(3) &= \chi_\alpha(2) \\ \chi_\alpha(4) &= \chi_\alpha(1) \\ \chi_\alpha(7) &= \chi_\alpha(6) \\ \chi_\alpha(8) &= \chi_\alpha(5) \end{aligned}\right\} \quad \alpha = 1,3$$

$$\left.\begin{aligned} \chi_\alpha(3) &= -\chi_\alpha(2) \\ \chi_\alpha(4) &= -\chi_\alpha(1) \\ \chi_\alpha(7) &= -\chi_\alpha(6) \\ \chi_\alpha(8) &= -\chi_\alpha(5) \end{aligned}\right\} \quad \alpha = 2,4 \qquad \text{(A.22)}$$

If the station is on the X-Y plane (z=0, θ=90°), χ_α are available only for cells 1, 2, 3 and 4 surrounding the station. Applying the symmetry relations for the 5th octant yields,

$$\left.\begin{aligned} \chi_\alpha(5) &= \chi_\alpha(1) \\ \chi_\alpha(6) &= \chi_\alpha(2) \\ \chi_\alpha(7) &= \chi_\alpha(3) \\ \chi_\alpha(8) &= \chi_\alpha(4) \end{aligned}\right\} \quad \alpha = 1,2$$

$$\left.\begin{aligned} \chi_\alpha(5) &= -\chi_\alpha(1) \\ \chi_\alpha(6) &= -\chi_\alpha(2) \\ \chi_\alpha(7) &= -\chi_\alpha(3) \\ \chi_\alpha(8) &= -\chi_\alpha(4) \end{aligned}\right\} \quad \alpha = 3,4 \qquad \text{(A.23)}$$

If the station is on the Z-axis (x=y=0, θ=0°), χ_α are available only for cells 1 and 5. Values of χ_α for cells 2 and 6 are obtained from those for cells 1 and 5 by applying the rules given in Eq. (A.21) for the Y-Z plane. χ_α values for cells 3, 4, 7 and 8 are next obtained from those for cells 1, 2, 5 and 6 by applying the rules given in Eq. (A.22) for the X-Z plane. If a station is on the Y-axis (x=z=0, θ=90°), ϕ=90°), χ_α are available for only cells 1 and 4. Values for cells 2 and 3 are obtained by first applying the rules of the Y-Z plane and values for cells 5, 6, 7 and 8 by next applying rules for the X-Y plane. If a station is on the X-axis (y=z=0, θ=90°, ϕ=0°), χ_α are available only for cells 1 and 2. Values for cells 3 and 4 are obtained by first applying the rules for the X-Z plane and values for cells 5,

6, 7 and 8 by next applying the rules for the X-Y plane. In short, no special rules are required for stations on either the X-, Y-, or Z-axis if the rules for the Y-Z, X-Z and X-Y planes, when applicable, are applied in sequence.

The FORTRAN subroutine INTER3 called by the MULTEES program M3 first applies the rules defined above for any station located at a boundary of the first octant. The 3-D spatial interpolation routine is then applied using the "raw" χ_α at the eight surrounding cells and the corresponding shape functions defined in Section G.6 of Bache, et al. [1975a]. By means of the above defined symmetry properties the MULTEES programs are able to perform the double numerical integration indicated in the definition of the multipole coefficients in the time domain Eq. (5.3), when linked to a 3-D finite difference calculation that generates source variables only throughout a region of space confined to the first octant. Treatment of the 3-D rupture source can therefore be restricted to a single octant or one-eighth of the full grid that would otherwise be required.

APPENDIX B

THE NONZERO MULTIPOLE COEFFICIENTS FOR THE BILATERAL RUPTURE

The equivalent elastic source representation for any arbitrary seismic source is defined by a series of multipole coefficients (Eq. (5.1)). Calculation of these multipole coefficients requires a numerical double integration over the surface of a sphere of radius R in the elastic region. The symmetry properties of the stick-slip earthquake for the configuration illustrated in Fig. 5.1 have been described above in Appendix A. In this appendix, these symmetry properties will be applied to derive the nonvanishing multipole coefficients for this bilateral rupture source model. As a practical result from the application of these symmetry properties, the required double integrations will be reduced to the spherical surface subtending only a single octant. While the nonzero multipole coefficients derived in this manner define the equivalent elastic source representation of the rupture model for a specific configuration in the source coordinate system, the coefficients for any other configuration can be derived from these by performing the appropriate series of transformations (rotations) to the source coordinate system.

The expression for the multipole coefficients in the time domain (Eq. (5.3)) provides a convenient starting point for the application of symmetry properties. The integration in θ can first be reduced to

$$A^{(\alpha)}_{\ell ms}(R,t) =$$

$$\frac{1}{N^2_{\ell m}} \left\{ \int_0^2 \int_0^{\pi/2} \left| \chi_\alpha(R,\theta,\phi,t) + (-)^{\ell+m} \chi_\alpha(R,\pi-\theta,\phi,t) \right| \right.$$

$$\left. \times P^m_\ell(\cos\theta) \sin\theta d\theta \right\} \begin{Bmatrix} \cos m\phi \\ \sin m\phi \end{Bmatrix} d\phi, \qquad \text{(B.1)}$$

since

$$\cos(\pi-\theta) = -\cos\theta, \quad \sin(\pi-\theta) = \sin\theta, \text{ and}$$

$$P^m_\ell(\cos(\pi-\theta)) = (-)^{\ell+m} P^m_\ell(\cos\theta) .$$

If the potential χ_α is symmetric or antisymmetric with respect to reflection through the fault (X-Y) plane, that is, if

$$\chi_\alpha(R,\pi-\theta,\phi,t) = \pm \chi_\alpha(R,\theta,\phi,t)$$

where

$$0 \leq \theta \leq \pi/2 \quad \text{and} \quad 0 \leq \phi \leq \pi/2 ,$$

then the θ integration in Eq. (B.1) reduces to

$$\int_0^{\pi/2} [1 \pm (-)^{\ell+m}] \chi_\alpha(R,\theta,\phi,t) P^m_\ell(\cos\theta) \sin\theta \, d\theta . \qquad \text{(B.2)}$$

For symmetric potential functions, the following multipole coefficients vanish

$$A^{(\alpha)}_{\ell ms}(R,t) = 0 \quad \text{when} \quad (\ell+m) \text{ is odd;} \qquad \text{(B.3)}$$

similarly, for antisymmetric potential functions,'

$$A^{(\alpha)}_{\ell ms}(R,t) = 0 \quad \text{when} \quad (\ell+m) \text{ is even.} \tag{B.4}$$

The integration over the aximuthal angle ϕ can also be reduced to integrals over the first octant,

$$\int_0^{2\pi} \chi_\alpha(R,\theta,\phi,t) \begin{Bmatrix} \cos m\phi \\ \sin m\phi \end{Bmatrix} d\phi ,$$

$$= \int_0^{\pi/2} \left\{ \chi_\alpha(\phi) \pm \cos m\pi \; \chi_\alpha(\pi-\phi) + \cos m\pi \; \chi_\alpha(\pi+\phi) \right.$$

$$\left. \pm \chi_\alpha(-\phi) \right\} \begin{Bmatrix} \cos m\phi \\ \sin m\phi \end{Bmatrix} d\phi , \tag{B.5}$$

where

$$0 \le \phi \le \pi/2, \quad \chi_\alpha(\phi) \equiv \chi_\alpha(R,\theta,\phi,t),$$

$$\cos m(\pi \pm \phi) = \cos m\pi \cos m\phi ,$$

$$\sin m(\pi \pm \phi) = \pm \cos m\pi \sin m\phi , \tag{B.6}$$

$$\cos m(-\phi) = \cos m\phi ,$$

$$\sin m(-\phi) = -\sin m\phi .$$

In the last and third from last relations, the positive signs correspond to integrals with the factor cos $m\phi$ and the negative signs to those with sin $m\phi$. When m is even, the ϕ integral above can be expressed as,

$$\int_0^{\pi/2} [\chi_\alpha(\phi) \pm \chi_\alpha(\pi-\phi) + \chi_\alpha(\pi+\phi) \pm \chi_\alpha(-\phi)$$

$$\times \begin{Bmatrix} \cos m\phi \\ \sin m\phi \end{Bmatrix} d\phi \; ; \qquad \text{(B.7)}$$

similarly, when m is odd,

$$\int_0^{\pi/2} [\chi_\alpha(\phi) \mp \chi_\alpha(\pi-\phi) - \chi_\alpha(\pi+\phi) \pm \chi_\alpha(-\phi)$$

$$\times \begin{Bmatrix} \cos m\phi \\ \sin m\phi \end{Bmatrix} d\phi . \qquad \text{(B.8)}$$

B.1 SCALAR DILATATION POTENTIAL (χ_4)

For the scalar potential χ_4 the symmetry properties are (Appendix A):

$$\begin{aligned} \chi_4(R,\pi-\theta,\phi,t) &= -\chi_4(R,\theta,\phi,t) , \\ \chi_4(R,\theta,\pi-\phi,t) &= +\chi_4(R,\theta,\phi,t) , \\ \chi_4(R,\theta,\pi+\phi,t) &= -\chi_4(R,\theta,\phi,t) , \\ \chi_4(R,\theta,-\phi,t) &= -\chi_4(R,\theta,\phi,t) . \end{aligned} \qquad \text{(B.9)}$$

Since χ_4 is antisymmetric in θ,

$$A^{(4)}_{\ell ms}(R,t) = 0 \quad \text{when} \quad (\ell+m) \text{ is even.} \qquad \text{(B.10)}$$

Application of the symmetry properties expressed by Eq. (B.9) in the ϕ integral, Eq. (B.7), shows that

$$A^{(4)}_{\ell ms}(R,t) = 0, \text{ when m is even,}$$

$$A^{(4)}_{\ell ms}(R,t) = 0, \text{ when m is odd and } s = 0. \tag{B.11}$$

Consequently, the only nonvanishing multipole coefficients for $\alpha = 4$ are expressed as

$$A^{(4)}_{\ell m_1}(R,t) = \frac{8}{N^2_{\ell m}} \int_0^{\pi/2} \int_0^{\pi/2} \chi_4(R,\theta,\phi,t) \times P^m_\ell(\cos\theta) \sin\theta \, d\theta \sin m\phi \, d\phi, \tag{B.12}$$

where $(\ell+m)$ is odd, m is odd and $s = 1$, in short,

$s = 1$

$\ell = 2, 4, 6, 8, \ldots$,

$m = 1, 3, .. (\ell - 1)$.

The nonvanishing multipole coefficients for $\alpha = 4$ are

$$A^{(4)}_{211}, A^{(4)}_{411}, A^{(4)}_{431}, A^{(4)}_{611}, A^{(4)}_{631}, A^{(4)}_{651}, \text{ etc.}$$

B.2 VECTOR ROTATION POTENTIAL ($\underset{\sim}{\chi}$)

For the first component of the vector potential, χ_1, the symmetry properties are:

$$\chi_1(R,\pi-\theta,\phi,\ t) = +\ \chi_1(R,\theta,\phi,t),$$

$$\chi_1(R,\theta,\pi-\phi,t) = +\ \chi_1(R,\theta,\phi,t)\ ,$$

$$\chi_1(R,\theta,\pi+\phi,t) = +\ \chi_1(R,\theta,\phi,t)\ , \qquad \text{(B.13)}$$

$$\chi_1(R,\theta,-\phi,t)\ \ = +\ \chi_1(R,\theta,\phi,t)\ .$$

Application of the symmetry properties in the θ and ϕ integrals shows that

$$A^{(1)}_{\ell ms}\ (R,t) = 0, \text{ when } (\ell+m) \text{ is odd},$$

$$A^{(1)}_{\ell ms}\ (R,t) = 0, \text{ when } m \text{ is even and } s = 1, \qquad \text{(B.14)}$$

$$A^{(1)}_{\ell ms}\ (R,t) = 0, \text{ when } m \text{ is odd}.$$

Consequently, the only nonvanishing multipole coefficients for $\alpha = 1$ can be expressed as

$$A^{(1)}_{\ell mo}\ (R,t) = \frac{8}{N^2_{\ell m}} \int_0^{\pi/2}\int_0^{\pi/2} \chi_1(R,\theta,\phi,t)\ P^m_\ell\ (\cos\theta)$$

$$\times \sin\theta\ d\theta\ \cos m\phi\ d\phi \qquad \text{(B.15)}$$

where $(\ell+m)$ is even, m is even, and $s = 0$; in short,

$$s = 0\ ,$$

$$\ell = 0,\ 2,\ 4,\ 6,\ \ldots\ ,$$

$$m = 0,\ 2,\ \ldots \ell\ .$$

The only nonvanishing terms for $\alpha = 1$ are:

$$A^{(1)}_{000},\ A^{(1)}_{200},\ A^{(1)}_{220},\ A^{(1)}_{400},\ A^{(1)}_{420},\ A^{(1)}_{440},\ \text{etc.}$$

For the second component of the vector potential, χ_2, the symmetry properties are:

$$\begin{aligned}
\chi_2(R,\pi-\theta,\phi,t) &= +\chi_2(R,\theta,\phi,t)\ , \\
\chi_2(R,\theta,\pi-\phi,t) &= -\chi_2(R,\theta,\phi,t)\ , \\
\chi_2(R,\theta,\pi+\phi,t) &= +\chi_2(R,\theta,\phi,t)\ , \\
\chi_2(R,\theta,-\phi,t) &= -\chi_2(R,\theta,\phi,t)\ .
\end{aligned} \tag{B.16}$$

From these relations, it follows that

$$\begin{aligned}
&A^{(2)}_{\ell ms}(R,t) = 0, \text{ when } (\ell+m) \text{ is odd}, \\
&A^{(2)}_{\ell ms}(R,t) = 0, \text{ when } m \text{ is even, } s = 0, \\
&A^{(2)}_{\ell ms}(R,t) = 0, \text{ when } m \text{ is odd}.
\end{aligned} \tag{B.17}$$

Consequently, the only nonvanishing multipole coefficients for $\alpha = 2$ can be expressed as

$$A^{(2)}_{\ell ms}(R,t) = \frac{8}{N^2_{\ell m}} \int_0^{\pi/2}\int_0^{\pi/2} \chi_2(R,\theta,\phi,t)\, P^m_\ell(\cos\theta) \times \sin\theta\, d\theta \sin m\phi\, d\theta, \tag{B.18}$$

where $(\ell+m)$ is even, m is even, $s = 1$; in short,

$$\begin{aligned}
&s = 1\ , \\
&\ell = 2, 4, 6, 8, \ldots\ , \\
&m = 2, 4, \ldots \ell\ .
\end{aligned}$$

The only nonvanishing terms for $\alpha = 2$ are:

$$A^{(2)}_{221},\ A^{(2)}_{421},\ A^{(2)}_{441},\ A^{(2)}_{621},\ A^{(2)}_{641},\ A^{(2)}_{661},\ \text{etc.}$$

For the third component of the vector potential, χ_3, the required symmetry properties are

$$\begin{aligned}
\chi_3(R,\pi-\theta,\phi,t) &= -\chi_3(R,\theta,\phi,t)\ , \\
\chi_3(R,\theta,\pi-\phi,t) &= -\chi_3(R,\theta,\phi,t)\ , \\
\chi_3(R,\theta,\pi+\phi,t) &= -\chi_3(R,\theta,\phi,t)\ , \\
\chi_3(R,\theta,-\phi,t) &= +\chi_3(R,\theta,\phi,t)\ .
\end{aligned} \tag{B.19}$$

Application of these symmetry properties in the θ and ϕ integrals shows that

$$\begin{aligned}
&A^{(3)}_{\ell ms}(R,t) = 0, \text{ when } (\ell+m) \text{ is even}, \\
&A^{(3)}_{\ell ms}(R,t) = 0, \text{ when } m \text{ is even}, \\
&A^{(3)}_{\ell ms}(R,t) = 0, \text{ when } m \text{ is odd and } s = 1.
\end{aligned} \tag{B.20}$$

Consequently, the only nonvanishing multipole coefficients for $\alpha = 3$ can be expressed

$$A^{(3)}_{\ell mo}(R,t) = \frac{8}{N^2_{\ell m}} \int_0^{\pi/2}\int_0^{\pi/2} \chi_3(R,\theta,\phi,t)\, P^m_\ell(\cos\theta) \times \sin\theta\, d\theta \cos m\phi\, d\phi, \tag{B.21}$$

where $(\ell+m)$ is odd, m is odd, and $s = 0$; in short,

$$\begin{aligned}
&s = 0\ , \\
&\ell = 2, 4, 6, \ldots\ , \\
&m = 1, 3, \ldots (\ell-1)\ .
\end{aligned}$$

The only nonvanishing terms for $\alpha = 3$ are

$$A^{(3)}_{210},\ A^{(3)}_{410},\ A^{(3)}_{430},\ A^{(3)}_{610},\ A^{(3)}_{630},\ A^{(3)}_{650},\ \ldots \text{ etc.}$$

A summary of the nonvanishing multipole coefficients for the rupture model with a prestress $S_{ZY} \neq 0$ is presented in Table B.1 for convenient reference. The familiar notation used in earlier reports (e.g., Bache, et al. [1974]) for these coefficients is related to that introduced above as,

$$\begin{aligned} A^{(\alpha)}_{\ell m} &\equiv A^{(\alpha)}_{\ell m_0} \\ B^{(\alpha)}_{\ell m} &\equiv A^{(\alpha)}_{\ell m_1} \ . \end{aligned} \tag{B.22}$$

The second column in this table labeled "ℓms" gives a unique index which has a one-to-one correspondence with the triple set of indices (ℓ,m,s). Summations over ℓ, m, and s are equivalent to a single summation over the "ℓms" index, which identifies all possible multipole terms; for example, all terms such as $A^{(\alpha)}_{\ell 0 1} \equiv B^{(\alpha)}_{\ell 0}$, which are identically zero, are excluded in a summation over "ℓms".

The existence of a nonvanishing S-wave monopole term, $A^{(1)}_{00}$, should be noted. This term is related to a rotation about the X-axis that is in the same direction for all points on the surface of any sphere in the elastic region. Since the rupture is not allowed to induce a net rigid body rotation of the medium, this term must vanish at late times.

There are five nonvanishing quadrupole terms

$$A^{(1)}_{20},\ A^{(1)}_{22},\ A^{(3)}_{21},\ B^{(2)}_{22},\ \text{and}\ B^{(4)}_{21}.$$

These terms specify the double-couple characterizing the source and are expected to be the dominant terms for long periods.

There are nine nonvanishing octupole terms:

$$A_{40}^{(1)},\ A_{42}^{(1)},\ A_{44}^{(1)},\ B_{42}^{(2)},\ B_{44}^{(2)},\ A_{41}^{(3)},\ A_{43}^{(3)},\ B_{41}^{(4)},\ \text{and}\ B_{43}^{(4)}.$$

There are 13 terms of sixth order:

$$A_{60}^{(1)},\ A_{62}^{(1)},\ A_{64}^{(1)},\ A_{66}^{(1)},\ B_{62}^{(2)},\ B_{64}^{(2)},\ B_{66}^{(2)},\ A_{61}^{(3)},\ A_{63}^{(3)},$$

$$A_{65}^{(3)},\ B_{61}^{(4)},\ B_{63}^{(4)},\ \text{and}\ B_{65}^{(4)}.$$

TABLE B.1. SUMMARY OF NONVANISHING MULTIPOLE COEFFICIENTS FOR RUPTURE MODEL WITH PRESTRESS $S_{ZY} \neq 0$

($A_{\ell m}^{(\alpha)} \equiv A_{\ell m 0}^{(\alpha)}$; $B_{\ell m}^{(\alpha)} \equiv A_{\ell m 1}^{(\alpha)}$)

#	ℓms	ℓ	m	s	α = 1	α = 2	α = 3	α = 4
1	1	0	0	0	$A_{00}^{(1)}$			
2	5	2	0	0	$A_{20}^{(1)}$			
3	6	2	1	0			$A_{21}^{(3)}$	
4	7	2	2	0	$A_{22}^{(1)}$			
5	8	2	1	1				$B_{21}^{(4)}$
6	9	2	2	1		$B_{22}^{(2)}$		
7	17	4	0	0	$A_{40}^{(1)}$			
8	18	4	1	0			$A_{41}^{(3)}$	
9	19	4	2	0	$A_{42}^{(1)}$			
10	20	4	3	0			$A_{43}^{(3)}$	
11	21	4	4	0	$A_{44}^{(1)}$			
12	22	4	1	1				$B_{41}^{(4)}$
13	23	4	2	1		$B_{42}^{(2)}$		
14	24	4	3	1				$B_{43}^{(4)}$
15	25	4	4	1		$B_{44}^{(2)}$		
16	27	6	0	0	$A_{60}^{(1)}$			
17	38	6	1	0			$A_{61}^{(3)}$	
18	39	6	2	0	$A_{62}^{(1)}$			
19	40	6	3	0			$A_{63}^{(3)}$	
20	41	6	4	0	$A_{64}^{(1)}$			
21	42	6	5	0			$A_{65}^{(3)}$	
22	43	6	6	0	$A_{66}^{(1)}$			
23	44	6	1	1				$B_{61}^{(4)}$
24	45	6	2	1		$B_{62}^{(2)}$		
25	46	6	3	1				$B_{63}^{(4)}$
26	47	6	4	1		$B_{64}^{(2)}$		
27	48	6	5	1				$B_{65}^{(4)}$
28	49	6	6	1		$B_{66}^{(2)}$		

APPENDIX C

ASYMPTOTIC BEHAVIOR OF THE EQUIVALENT ELASTIC SOURCE

The main interest in analytically evaluating asymptotic forms for the equivalent elastic source is twofold. First, these forms provide a check on the numerical calculations and the resulting spectral plots and radiation patterns. In addition, the character of the relative excitation of the various multipoles representing the source will illustrate how the 3-D finite difference earthquake simulation differs from other earthquake models. The asymptotic behavior of the potential spectra will be described first, followed by a discussion of displacement spectra.

C.1 ASYMPTOTIC BEHAVIOR OF THE POTENTIAL SPECTRA

C.1.1 Low-Frequency Behavior

The low-frequency limit corresponds to the condition $\omega << 1$. In the series representation of the potential spectra there are two types of frequency dependent factors, $\tilde{A}^{(\alpha)}_{\ell ms}(\omega)$ and $h^{(2)}_{\ell}(k_\alpha r)$, whose low-frequency behavior will first be examined separately. Numerical results from calculations of the multipole coefficients for the finite difference earthquake source show that the $\tilde{A}^{(\alpha)}_{\ell ms}$ display the following behavior at low frequencies (even up to 1.0 Hz):

$$|\tilde{A}^{(1)}_{00}(\omega)| \sim \omega^3 , \quad \omega << 1$$

$$|\tilde{A}^{(\alpha)}_{\ell ms}(\omega)| \sim \omega^{\ell} , \quad \ell \geq 2, \ \omega << 1 , \tag{C.1}$$

where again

$$\tilde{A}^{(\alpha)}_{\ell m0} \equiv \tilde{A}^{(\alpha)}_{\ell m} \text{ and } \tilde{A}^{(\alpha)}_{\ell m1} \equiv \tilde{B}^{(\alpha)}_{\ell m}.$$

The radial spreading of the potential spectra is controlled by the Hankel functions. Since the frequency enters these functions only in the argument

$$k_\alpha R = \omega R/v_\alpha \ ,$$

one must take into account the hypocentral distance R of the observer. For the far-field radiation the appropriate asymptotic form of the Hankel function is given as

$$h_\ell^{(2)}(k_\alpha R) \sim \frac{i^{\ell+1} e^{-ik_\alpha R}}{k_\alpha R} \ , \quad (k_\alpha R >> 1) \tag{C.2}$$

or

$$h_\ell^{(2)}(k_\alpha R) \sim \omega^{-1} , \quad (k_\alpha R >> 1) . \tag{C.3}$$

In the low-frequency limit the "far-field" monopole portion of the potential will behave as

$$|\tilde{A}_{00}^{(1)}(\omega)\ h_0^{(2)}(k_\alpha R)| \sim \omega^2 \ ;$$

all higher order terms ($\ell = 2, 4, 6, \ldots$) will behave as

$$|\tilde{A}_{\ell ms}^{(\alpha)}(\omega)\ h_0^{(2)}(k_\alpha R)| \sim \omega^{\ell-1} \ , \ \ell \geq 2 \ . \tag{C.4}$$

In the low-frequency limit when $\omega << 1$, the far-field radiation is expected to be dominated by the quadrupole field, which goes as the first power of ω. In summary, the asymptotic behavior of the "far-field" potential spectra in the low-frequency limit is

$$|\tilde{\chi}_\alpha(R,\theta,\phi,\omega)| \sim \omega \ ,$$

for

$$k_\alpha R >> 1 \quad \text{and} \quad \omega << 1 \ . \tag{C.5}$$

While our interest here is confined primarily to the far field, it can be shown that the low-frequency quadrupole field is also expected to be dominant in the "near-field" zone. This limit corresponds to the double condition

$$\omega << 1 \quad \text{and} \quad k_\alpha R << 1 ,$$

where the appropriate asymptotic form of the Hankel function as the argument approaches 0 is given by the leading term,

$$h_\ell^{(2)}(k_\alpha R) \sim \frac{i(2\ell)!}{2^\ell \ell! (k_\alpha R)^{\ell+1}} ,$$

or

$$h_\ell^{(2)}(k_\alpha R) \sim \omega^{-\ell-1} , \quad (k_\alpha R << 1) . \tag{C.6}$$

Combining the results given in Eq. (C.1) and Eq. (C.6) shows that in the low frequency "near-field" limit, the monopole field will behave asymptotically as ω^2, while the quadrupole and higher (even) order terms behave as ω^{-1}. As a result, the potential spectra in the low frequency "near-field" limit is expected to behave as

$$|\tilde{\chi}_\alpha(R,\theta,\phi,\omega)| \sim \frac{1}{\omega} ,$$

for

$$\omega << 1 \quad \text{and} \quad k_\alpha R << 1 . \tag{C.7}$$

C.1.2 High-Frequency Behavior

The high-frequency limit, which corresponds to the condition $\omega >> 1$, is not as easy to evaluate due to limitations on the high-frequency information generated by the numerical source calculation. The basis for the existence of a high-frequency cutoff is discussed in Appendix D. This cutoff in

the finite difference calculation, which is estimated to be about 3.0 - 5.0 Hz, prevents our deriving any definitive conclusions about the behavior of the multipole coefficients in the high-frequency limit.

The numerical results from calculating $\tilde{A}^{(\alpha)}_{\ell ms}(\omega)$ up to 5 Hz, however, does show that the quadrupole terms decay at a rate given approximately as ω^{-1}. Since the Hankel function in the far-field contributes a term of ω^{-1}, the field due to the quadrupole part of the source might be expected to behave as ω^{-2} in the high-frequency limit ($\omega >> 1$). On the other hand, the octupole terms were found to behave differently in the range of 1.0 to 5.0 Hz — not decaying as rapidly as the quadrupole terms; consequently, no estimate could be made of the high-frequency limit for terms of higher order than $\ell = 2$.

In summary, multipole fields of all orders contribute to the high-frequency radiation. Convergence of the multipole series may not be very rapid in the middle and high frequency range; a large number of higher-order terms would have to be calculated in order to derive the full radiation field for any given frequency beyond say 5 Hz. However, limitations at high frequencies will not introduce any practical difficulties for those lower frequencies, generally below 1 - 3 Hz, that are of chief interest in teleseismic studies.

C.2 ASYMPTOTIC BEHAVIOR OF THE FAR-FIELD DISPLACEMENT SPECTRA

The displacement spectrum is given in terms of the potential spectrum by

$$\tilde{u}\ (\underset{\sim}{r},\ \omega) = -\frac{1}{k_P^2}\nabla\ \tilde{\chi}_4\ (\underset{\sim}{r},\ \omega)$$

$$+\frac{2}{k_S^2}\nabla \times \tilde{\underset{\sim}{\chi}}\ (\underset{\sim}{r},\ \omega)\ , \qquad \text{(C.8)}$$

where χ_4 is the dilatational potential and $\underset{\sim}{\chi}$ is the rotational potential. The far-field spherical (polar) components of the displacement spectrum are according to Minster [1974]

$$[\tilde{u}_r\ (\underset{\sim}{r},\ \omega)]_F = -\frac{1}{k_P^2}\ \frac{\partial}{\partial r}\ \tilde{\chi}_4\ (\underset{\sim}{r},\ \omega)\ ,$$

$$[\tilde{u}_\theta\ (\underset{\sim}{r},\ \omega)]_F = \frac{2}{k_S^2}\ \left|\sin\phi\ \frac{\partial\tilde{\chi}_1}{\partial r} - \cos\phi\ \frac{\partial\tilde{\chi}_2}{\partial r}\right|\ ,$$

$$[\tilde{u}_\phi\ (\underset{\sim}{r},\ \omega)]_F = \frac{2}{k_S^2}\ \left|\cos\theta\ \cos\phi\ \frac{\partial\tilde{\chi}_1}{\partial r}\right.$$

$$\left. + \cos\theta\ \sin\phi\ \frac{\partial\tilde{\chi}_2}{\partial r} - \sin\phi\ \frac{\partial\tilde{\chi}_3}{\partial r}\right|\ . \qquad \text{(C.9)}$$

In the far-field the radial displacement results only from P-wave terms involving χ_4, and the transverse displacement (u_θ and u_ϕ) is only excited by S-wave terms involving $\underset{\sim}{\chi}$. Such a convenient separation of the P and S wave into purely radial and purely transverse terms is not possible in the near-field, since each displacement component will involve both χ_4 and $\underset{\sim}{\chi}$ as given in Eq. (C.8). Only displacement radiation patterns and spectral amplitudes in the far-field will be discussed below.

In the far-field approximation of the radial derivatives of the potentials appearing in Eq. (C.9), only a single term survives, irrespective of multipole order, namely

$$\left[\frac{\partial}{\partial r}\ h_\ell^{(2)}\ (k_\alpha R)\right]_F = \frac{i^\ell\ e^{-ik_\alpha R}}{R}\ . \qquad \text{(C.10)}$$

Consequently, in the far-field the radial dependence of both the longitudinal and transverse displacement spectra can be separated out of the expressions given above, leaving a series in which each term is the product only of a multipole coefficient and an associated Legendre function. For example, the radial component of the P-wave in the far-field is

$$\tilde{u}_r^{(P)}(R,\theta,\phi,\omega) = -\frac{1}{k_p^2}\frac{e^{-ik_pR}}{R}$$

$$\times \sum_{\ell=2,4,..}^{\infty} \sum_{\substack{m=1 \\ (odd)}}^{\ell-1} i^{\ell}\, \tilde{B}_{\ell m}^{(4)}(\omega)\, P_{\ell}^{m}(\cos\theta)\, \sin m\phi \quad . \qquad (C.11)$$

The θ component of the S-wave in the far-field is

$$\tilde{u}_\theta^{(S)}(R,\theta,\phi,\omega) = \frac{2\, e^{-ik_sR}}{k_s^2 R}$$

$$\left\{ \sum_{\ell=0,2,4}^{\infty} \sum_{\substack{m=0 \\ (even)}}^{\ell} i^{\ell}\, \tilde{A}_{\ell m}^{(1)}(\omega)\, P_{\ell}^{m}(\cos\theta)\, \cos m\phi\, \sin\phi \right.$$

$$\left. - \sum_{\ell=2,4,6}^{\infty} \sum_{\substack{m=2 \\ (even)}}^{\ell} i^{\ell}\, \tilde{B}_{\ell m}^{(2)}(\omega)\, P_{\ell}^{m}(\cos\theta)\, \sin m\phi\, \cos\phi \right\} . \qquad (C.12)$$

Expanding the far-field displacement spectrum yields,

$$\tilde{u}_r^{(P)}(R,\theta,\phi,\omega) = + \frac{1}{k_p^2} \frac{e^{-ik_pR}}{R}$$

$$\times \left\{ \tilde{B}_{21}^{(4)}(\omega)\ P_2^1(\cos\theta)\ \sin\phi - \tilde{B}_{41}^{(4)}(\omega)\ P_4^1(\cos\theta)\ \sin\phi \right.$$

$$\left. - \tilde{B}_{43}^{(4)}(\omega)\ P_4^3(\cos\theta)\ \sin 3\phi + \ldots \right\}, \qquad \text{(C.13)}$$

$$\tilde{u}_\theta^{(S)}(R,\theta,\phi,\omega) = \frac{2\ e^{-ik_sR}}{k_s^2 R}$$

$$\times \left\{ \tilde{A}_{00}^{(1)}(\omega)\ \sin\phi - \tilde{A}_{20}^{(1)}(\omega)\ P_2^0(\cos\theta)\ \sin\phi \right.$$

$$- \tilde{A}_{22}^{(1)}(\omega)\ P_2^2(\cos\theta)\ \cos 2\phi\ \sin\phi$$

$$+ \tilde{B}_{22}^{(2)}(\omega)\ P_2^2(\cos\theta)\ \sin 2\phi\ \cos\phi$$

$$+ \tilde{A}_{40}^{(1)}(\omega)\ P_4^0(\cos\theta)\ \sin\phi$$

$$+ \tilde{A}_{42}^{(1)}(\omega)\ P_4^2(\cos\theta)\ \cos 2\phi\ \sin\phi$$

$$+ \tilde{A}_{44}^{(1)}(\omega)\ P_4^4(\cos\theta)\ \cos 4\phi\ \sin\phi$$

$$- \tilde{B}_{42}^{(2)}(\omega)\ P_4^2(\cos\theta)\ \sin 2\phi\ \cos\phi$$

$$\left. - \tilde{B}_{44}^{(2)}(\omega)\ P_4^4(\cos\theta)\ \sin 4\phi\ \cos\phi + \ldots \right\}. \qquad \text{(C.14)}$$

Analyzing either the P- or S-wave displacement spectrum in the far field allows one to derive its asymptotic behavior. The low frequency asymptotic behavior of the multipole coefficients has been seen to be ω^ℓ for $\ell \geq 2$. The leading

term at low frequencies is the quadrupole, so that the multipole coefficient behaves as ω^2. The leading factor involving the wave number k behaves as ω^{-2}. The net result is that in the far-field the displacement spectrum should be "flat" in the low frequency limit. Only at high frequencies when the effects of multipoles beyond $\ell = 2$ become significant will this flat behavior be perturbed.

The high frequency asymptotic behavior of the displacement spectrum is more difficult to analyze. While information on the high frequency behavior of the multipole coefficients is limited in the finite difference calculation (see Appendix D), most quadrupole terms were estimated to behave approximately as ω^{-1}. Higher order terms are not expected to damp as rapidly as the quadrupole terms, so that the net result might be that the asymptotic behavior of the displacement spectrum is ω^{-2} for $\omega >> 1$. Consequently, the displacement spectrum is expected to behave as

$$|\tilde{u}_i(\underset{\sim}{r},\omega)| \sim \omega^{-q} \quad \text{for} \quad \omega >> 1 \ , \tag{C.15}$$

with $q \leq 3$.

The main interest in analytically evaluating asymptotic forms for the spectra is that they will provide a check on the numerical calculations to be presented below. The slope of the amplitude spectra is expected to be azimuthally dependent because of interferences between the multipole fields of different orders.

APPENDIX D

HIGH-FREQUENCY APPROXIMATIONS DUE TO THE DISCRETE GRID IN THE THREE-DIMENSIONAL FINITE DIFFERENCE CALCULATION

There are several effects associated with the use of a discrete grid which must be taken into account when analyzing the results of numerical finite difference calculations. A practical result of these effects is the introduction of a high-frequency cutoff. Useful information from the 3-D earthquake simulation will be limited to frequencies below this cutoff. Before proceeding to derive an estimate of the high-frequency cutoff, which is the objective of this discussion, two effects will be sketched to illustrate how approximations originate in the finite difference method. High-frequency attenuation due to the introduction of artificial damping will be discussed first. The second illustration will show how dispersion effects arise from the discretization of the applicable continuum mechanics equations in the 3-D finite difference calculation. Finally, the last subsection will provide some estimates for a high-frequency cutoff.

D.1 HIGH-FREQUENCY ATTENUATION DUE TO ARTIFICIAL DAMPING IN THE THREE-DIMENSIONAL EARTHQUAKE CALCULATION

In finite difference stress wave calculations it is often desirable to include viscosity in the material properties to maintain smooth profiles at wave fronts. This viscosity is often called artificial viscosity. However, it is useful to realize that finite difference codes generally do not propagate waves in purely elastic media, but only in materials that are to some extent viscoelastic.

In the three-dimensional finite difference earthquake calculation, the "artificial viscosity" terms cause the material to behave as a Voight solid model of viscoelasticity.

The effect of the viscoelasticity on a propagating wave is shown in Ewing, Jardetsky and Press [1957], Chapter 5. A propagating compressional wave is attenuated by exp [-τx] where

$$\tau^2 = \frac{\omega^2}{2\alpha^2 (1 + a^2\omega^2)} \left\{ \left| 1 + a^2\omega^2 \right|^{1/2} - 1 \right\} , \qquad (D.1)$$

where α is the compressional wave velocity while a is a selected constant characterizing the material viscoelasticity.

In the finite difference code a is selected to be $q\ \Delta t$ where Δt is the time step and q is a number which is empirically chosen to maintain stability. It is, of course, directly related to the amount of damping.

When $a^2\omega^2 << 1$, (D.1) can be expanded in power series to give

$$\tau = \frac{a}{2\alpha} \omega^2 + O\ (a^2\omega^4) . \qquad (D.2)$$

For a finite difference earthquake calculation $\alpha = 5.7 \times 10^5$ cm/sec and $a = 10^{-3}$ sec. In this case,

$$\tau \simeq 8.8 \times 10^{-10}\ \omega^2 \qquad (D.3)$$

The elastic radius in the earthquake calculation was at 1.5 km. Since the attenuation due to linear artificial viscosity is exp [- τx], its effect on the displacement spectrum can be estimated. Tabulating versus frequency we find

f(Hz)	exp[-τ·1.5 km]
1.0	0.995
2.0	0.98
3.0	0.95
4.0	0.92
5.0	0.88
10.0	0.59

Therefore, the attenuation due to artificial viscosity has minor effect (at this distance) for frequencies less than 5 Hz.

D.2 DISCRETIZATION ERRORS

The difference equations used in finite difference codes are discrete analogs of differential equations. However, the solutions of the difference equations are not identical to the solutions of the analogous differential equations. We must be certain that the errors introduced by the discretization are not influencing the solutions to a substantial degree.

The governing equations for one-dimensional, linear elastic wave propagation may be written:

$$\begin{aligned} \rho\dot{v} &= \sigma' , \\ \dot{\sigma} &= Kv' , \end{aligned} \tag{D.4}$$

where v is velocity, σ is stress, $K = \lambda + 2\mu$, the dot signifies time differentiation and the prime signifies spatial differentation. The finite difference equations in most Lagrangian finite difference codes are the (multi-dimensional) finite difference analogs of the differential equations (D.4).

We can write (D.4) in finite difference form and study the properties of a propagating wave compared to the same wave in a continuous medium. The wave in the discrete system turns out to be dispersed. We should be certain that the frequency components of interest are in the region where this dispersion effect is weak.

The finite difference analog of (D.4) may be written

$$\begin{aligned} \frac{\rho}{\Delta t}\left[v_j^{m+1} - v_j^m\right] &= \frac{1}{\Delta x}\left[\sigma_{j+1/2}^m - \sigma_{j-1/2}^m\right] , \\ \frac{1}{\Delta t}\left[\sigma_{j+1/2}^{m+1} - \sigma_{j+1/2}^m\right] &= \frac{K}{\Delta x}\left[v_{j+1}^{m+1} - v_j^{m+1}\right] . \end{aligned} \tag{D.5}$$

If solutions of the form $\exp[i(kx-\omega t)]$ are assumed, substitution into (D.5) gives two homogeneous simultaneous equations in the unknowns v and σ. Requiring the determinant to vanish gives the dispersion relation between ω and k.

This is

$$\frac{\rho}{\Delta t^2}\left[e^{-2i\omega\Delta t} - 2e^{-i\omega\Delta t} + 1\right] + \frac{Ke^{-i\omega\Delta t}}{\Delta x^2}\left[2-e^{ik\Delta x} - e^{-ik\Delta x}\right] = 0. \tag{D.6}$$

Note that Δt and Δx are related by the Courant stability condition

$$n\Delta x = \alpha\Delta t, \tag{D.7}$$

where $n < 1$.

If it is assumed that $\omega\Delta t$, $k\Delta x \ll 1$, the exponentials in (D.6) can be expanded in power series and the result reduced to

$$\omega^2 = k^2\alpha^2\left[1 + \frac{25}{12}\omega^2\Delta t^2 - \frac{k^2\Delta x^2}{12} + O(\omega^4\Delta t^4) + O(k^4\Delta x^4)\right], \tag{D.8}$$

where $\alpha^2 = K/\rho$ has been used.

Then using (B.7)

$$\omega^2 \approx k^2\alpha^2\left[1 + k^2\alpha^2\Delta t^2\left(\frac{25}{12} - \frac{1}{12n^2}\right)\right] \tag{D.9}$$

In terms of the phase velocity $c = \omega/k$,

$$c \approx \alpha\left[1 + \frac{b}{2}\omega^2\Delta t^2\right] \tag{D.10}$$

where $b = (25 - n^{-2})/12$ and for $0.2 < n < 1$, $0 < b < 2$.

For the three-dimensional finite difference earthquake calculation, the pertinent parameters were $\Delta t = 0.005$ sec and $n = 0.285$. Then

$$c \simeq \alpha \left[1 + 5.2 \times 10^{-4} f^2\right], \tag{D.11}$$

and we see that the effect is very small for low frequencies. For 5 Hz, $c \simeq 1.01\,\alpha$.

D.3 HIGH-FREQUENCY CUTOFF ESTIMATES

Effects due to the use of a discrete grid in the finite difference calculation will now be discussed from the point of view of deriving an estimate of the high-frequency cutoff that is associated with the 3-D earthquake source calculation. Consider first the effect often referred to as the aliasing of the continuous time series. Due to the digitization of the stress wave signal, information is not available at frequencies corresponding to wave numbers greater than the Nyquist wave number; this gives a cutoff frequency

$$f_N = \frac{v_\alpha k_N}{2\pi} = \frac{v_\alpha}{2\Delta x}, \text{ where } k_N = \frac{\pi}{\Delta x} \tag{D.12}$$

is the Nyquist wavenumber, Δx is a grid size (cell length), and v_α the body wave propagation velocity.

Another problem encountered by short duration pulses is that the velocity used to advance the motion at time t to $t + \Delta t$ is dependent on the wavenumber k for stress waves propagating on a discrete lattice. The origin of this dispersion effect was sketched above. The dispersion becomes important for 10 or fewer grid points per wavelength (Boore [1972]). This limitation yields a cutoff frequency

$$f_{max} = \frac{v_\alpha}{\lambda_{min}} = \frac{v_\alpha}{10\Delta x} \quad . \tag{D.13}$$

The same result is found, if one considers that at least 10 grid points are required to define a high frequency pulse. In a similar approach, if one uses the rule that in a single time cycle the wave can travel at most only one-half a cell dimension, then

$$\frac{\Delta x}{2} = v\Delta t, \text{ where } \Delta t = \text{cycle time}$$

and if say 10 grid points are required to define the shortest wavelength then

$$f_T = \frac{v}{\lambda_{min}} = \left(\frac{\Delta x}{2\Delta t}\right) \Big/ (10\Delta x) = \frac{1}{20\Delta t} \quad . \tag{D.14}$$

In the finite difference source calculations the following parameters were used:

$\Delta x = 0.1$ km

$\Delta t = 0.005$ sec

$v_P = 5.7$ km/sec

$v_S = 3.4$ km/sec .

Substituting in the above equations gives the following frequency limits (in Hz):

$f_N^P = 28.5$ $\qquad$ $f_N^S = 17.5$,

$f_{max}^P = 5.7$ $\qquad$ $f_{max}^S = 3.4$, and

$f_T = 10$.

As a conservative limit, for this specific finite difference source calculation the cutoff frequencies for P-wave and

S-wave spectra can be taken as 5.7 and 3.4 Hz, respectively. Consequently, information should be derived only for frequencies below, say

$$f_c^P \simeq 5 \text{ Hz} \quad \text{and} \quad f_c^S \simeq 3 \text{ Hz} \ . \tag{D.15}$$